



Forschungszentrum Karlsruhe
in der Helmholtz-Gemeinschaft

Wissenschaftliche Berichte
FZKA 7255

Electron-Phonon Coupling in Single-Walled Carbon Nanotubes

M. Oron-Carl
Institut für Nanotechnologie

September 2006

Forschungszentrum Karlsruhe

in der Helmholtz-Gemeinschaft

Wissenschaftliche Berichte

FZKA 7255

Electron-Phonon Coupling in Single-Walled Carbon Nanotubes

Matti Oron-Carl

Institut für Nanotechnologie

von der Fakultät für Chemie und Biowissenschaften der
Universität Karlsruhe (TH) genehmigte Dissertation

Forschungszentrum Karlsruhe GmbH, Karlsruhe

2006

Für diesen Bericht behalten wir uns alle Rechte vor

Forschungszentrum Karlsruhe GmbH
Postfach 3640, 76021 Karlsruhe

Mitglied der Hermann von Helmholtz-Gemeinschaft
Deutscher Forschungszentren (HGF)

ISSN 0947-8620

urn:nbn:de:0005-072552

Electron-Phonon Coupling in Single-Walled Carbon Nanotubes

Zur Erlangung des akademischen Grades eines
DOKTORS DER NATURWISSENSCHAFTEN

(Dr. rer. nat.)

von der Fakultät für Chemie und Biowissenschaften der
Universität Karlsruhe (TH)

genehmigte

DISSERTATION

von

Matti Oron-Carl

(M. Sc. in Chemistry)

aus Arad (Israel)

Dekan: Prof. Dr. Holger Puchta

Referent: Prof. Dr. Manfred M. Kappes

Korreferent: Prof. Dr. Matthias Olzmann

Tag der mündlichen Prüfung: 21. Juli 2006

Abstract

The present work investigates the strong electron-phonon coupling processes occurring on the level of individual metallic single-walled carbon nanotubes (SWNTs). In contrast to previous theory, we show that the phonon coupling to the electronic system in individual metallic SWNTs is not due to coupling to low-energy plasmons. This is based on evidence from the measured Raman-Stokes G-mode, which for metallic and semiconducting tubes could be fitted well by the superposition of only two Lorentzian lines associated with vibrational modes along the nanotube axis and the nanotube circumference. In the case of metallic tubes, the lower-energy G-mode is significantly broadened while maintaining the Lorentzian line shape, opposed to the theoretically expected asymmetric Breit-Wigner-Fano line shape from phonon-plasmon coupling. Based on the analysis of the Raman G modes' line shape, an alternative electron-phonon coupling mechanism was proposed. The proposed mechanism is based on results obtained by studying 25 individual metallic and semiconducting SWNTs with atomic force microscopy, electron transport measurements, and resonant Raman spectroscopy. To test the suggested electron-phonon coupling mechanism, a complementary study was performed in which the Raman spectra of metallic SWNTs were investigated under bias. Preliminary results show an increase in the high-energy phonons occupation, *i.e.*, an increase in the intensity of the anti-Stokes G peak.

Zusammenfassung

Elektron-Phonon Kopplung in einwandigen Kohlenstoff-Nanoröhren

Diese Arbeit untersucht starke Elektron-Phonon Kopplungsprozesse in einwandigen metallischen Kohlenstoff-Nanoröhren (SWNTs). Entgegen der bisherigen Theorie zeigen wir, dass in einzelnen metallischen SWNTs die Kopplung der Phononen an das elektronische System nicht auf der Kopplung an niederenergetische Plasmonen beruht. Die Grundlage hierzu bildet die Messung der Raman Stokes G-Mode, welche sowohl für metallische als auch für halbleitende Röhren gut durch die Superposition von nur zwei Lorentz-Kurven beschrieben werden konnte, die den Schwingungsmoden entlang der Achse und des Umfangs der Nanoröhre entsprechen. Im Fall metallischer Röhren ist die niederenergetische G-Mode bei Aufrechterhaltung der Lorentz-Linienform deutlich verbreitert, was im Gegensatz zu der theoretisch erwarteten asymmetrischen Breit-Wigner-Fano Linienform für die Phonon-Plasmon Kopplung steht. Ausgehend von der Analyse der Linienform der Raman G-Mode wird ein alternativer Mechanismus der Elektron-Phonon Kopplung vorgeschlagen. Dieser Mechanismus basiert auf Messungen an 25 einzelnen metallischen und halbleitenden SWNTs, die mittels Rasterkraftmikroskopie, elektronischen Transportmessungen und resonanter Ramanspektroskopie charakterisiert wurden. Um die vorgeschlagene Elektron-Phonon Kopplung zu verifizieren, wurde zusätzlich die Abhängigkeit der Ramanspektren metallischer SWNTs von der angelegten Spannung untersucht. Vorläufige Ergebnisse zeigen einen Anstieg der Besetzung der hochenergetischen Phononen, d.h., eine verstärkte Intensität des Peaks der Anti-Stokes G-Mode.

Contents

1. Introduction	1
2. Theoretical background	3
2.1. Carbon nanotube structure	3
2.2. Electronic properties	8
2.2.1. Zone-folding approximation	9
2.2.2. Energy gaps in quasi-metallic nanotubes	11
2.2.3. Density of states (DOS)	12
2.3. Electrical transport in SWNTs	13
2.3.1. Defect-induced elastic scattering in metallic SWNTs	15
2.3.2. High-bias electron-phonon scattering in metallic SWNTs	16
2.4. Raman Spectroscopy	19
2.4.1. First-order Raman scattering	20
2.4.2. The selection rules for Raman scattering in SWNTs	22
2.4.3. Double-resonant Raman scattering	23
2.4.4. The various Raman modes of SWNTs	25
2.4.5. Softening in metallic SWNTs	31
2.5. Dielectrophoresis	33
2.5.1. Basics of dielectrophoresis	34
2.5.2. The dielectrophoretic force on a small sphere	37
2.5.3. The formation of an inhomogeneous electric field	39
2.5.4. Dielectrophoresis in real dielectric materials	39
2.5.5. Dielectrophoretic force on SWNTs	40
3. Experimental	45
3.1. SWNTs synthesis via the pulsed laser vaporization (PLV) technique	45
3.2. Deposition of SWNTs via <i>low-frequency</i> dielectrophoresis	46
3.2.1. Two-point resistance measurements	50

3.3. Confocal Raman Microscope (CRM)	51
3.3.1. The CRM 200 Raman microscope	52
4. Results and discussion	57
4.1. Contact resistance measurements of individual SWNTs: tube-on-metal	58
4.2. AFM imaging of aligned SWNTs	59
4.3. Electrical transport and resonant Raman spectroscopy on the same individual SWNT	61
4.4. (n,m) assignment	64
4.5. G band broadening of metallic SWNTs	64
4.6. Simultaneous electrical and resonance Raman scattering measurements	76
4.6.1. The setup for simultaneous electrical and Raman measurements	77
4.6.2. Phonons' effective-temperature	78
4.6.3. Second lithography step: metal-on-tube	85
4.6.4. Optimizing the AS peak at zero bias	89
4.7. Towards electroluminescence	92
4.7.1. Ambipolar electrical behavior	95
5. Summary and outlook	99
A. Line-group notation	103
B. Surfactant-stabilized SWNTs suspension	105
C. Electrical and Raman correlation	107
C.1. Metallic SWNTs	108
C.2. Semiconducting SWNTs	111
D. Asymmetric BWF line-shape	115
E. Kohn anomaly in graphite	117
F. Hot phonons	119
G. IV_{SD} curves, Raman spectra and SEM images of biased SWNTs	121
G.1. $\ell = 0.5 \mu\text{m}$ $d_{\text{avg}} = 1.2 \text{ nm}$	122
G.2. $\ell = 1 \mu\text{m}$ $d_{\text{avg}} = 1.2 \text{ nm}$	125
G.3. $\ell = 1 \mu\text{m}$ $d_{\text{avg}} = 1.0 \text{ nm}$	126

H. Critical-point dryer (CPD)	127
I. Device fabrication for ambipolar SWNT s-FETs devices	129

Contents

1. Introduction

Research on carbon nanotubes has progressed rapidly since the first experimental observation of carbon nanotubes, using transmission electron microscopy, as reported by Iijima in 1991 [1]. Carbon nanotubes are graphene sheets rolled into hollow cylinders. Owing to their small size, a diameter on the order of nanometers and length on the order of microns, they can be regarded as large molecules or as quasi-one dimensional condensed matter with translational periodicity along their tube axis. The various structures of carbon nanotubes are due to the large variety of possible helical geometries. One of their most significant physical properties is the strong dependence of their electronic structure on their geometry. Although composed only from carbon atoms, their electronic band structure is either metallic or semiconducting in nature. This unique property, which depends solely on the combination of diameter and chirality, and does not require additional doping, is unique to solid state physics. Further, the energy gap of semiconducting carbon nanotubes can essentially vary continuously only by modifying the nanotube diameter. On this basis, various electronic applications are envisioned, such as: nanotube based-transistors, -sensors, -interconnectors, -field emission displays, -conductive coatings and more [2–8]. Metallic carbon nanotubes are particularly interesting due to their quasi-ballistic electron transport on the μm scale. However, recent experimental findings [9–11] show that the scattering length of electrons in the high-bias regime is more than a hundred times shorter than in the low-bias regime. In the high-bias regime, the accelerated electrons relax by the emission of high energy phonons.

The present work focuses on phonons in carbon nanotubes in general, and in particular on the electron-phonon interactions that play a central role in the relaxation processes occurring in single-walled carbon nanotubes (SWNT). If SWNTs are to be used in high-current applications as interconnectors or transistors operating in the saturation regime, a better understanding of the electron-phonon coupling is needed.

1. Introduction

This study comprises a systematic study of the electron-phonon coupling in SWNTs. To begin with, a detailed description of both structure and electronic properties of carbon nanotubes is given. Their induced curvature and the consequence of being quasi one-dimensional molecules are further discussed. Raman spectroscopy as the main characterization technique was applied mostly on individual carbon nanotubes, therefore the possible resonance processes occurring in these molecules and their resultant Raman modes are thoroughly covered. Next, the procedures for SWNT device fabrication are described with an emphasis on the deposition method. Electrical and Raman measurements on these devices were systematically performed and are displayed. In addition, research was performed to investigate the electron-phonon interactions occurring in metallic nanotubes at high biases. The possible back and forward electron scattering processes are illustrated with respect to the appropriate phonon modes. Line widths and effective temperature of high energy phonons are derived and discussed. An additional parallel study for the detection of infrared light from a single nanotube field effect transistor device was also initiated; some preliminary results are displayed.

2. Theoretical background

Carbon nanotubes are unique quasi-1D objects. In the following section, a condensed theoretical background is given about some of the carbon nanotubes properties. It starts with their physical structure, continues with their electronic band structure and concludes with their electrical transport and vibrational properties. In addition some basics in dielectrophoresis are given, as the method was used throughout the present work.

2.1. Carbon nanotube structure

A single-walled carbon nanotube (SWNT) is a rolled-up single graphite layer, called graphene. The resultant hollow cylinder comprises a monoatomic wall of sp^2 -bonded carbon atoms. If two or more concentrically arranged cylinders comprise the tube, it is called a double-walled (DWNT) or a multi-walled nanotube (MWNT), respectively. SWNTs were investigated in this work and thus the following discussion focuses on SWNTs.

Since carbon nanotubes are in effect rolled-up graphene sheets, their microscopic structure is strongly related to that of graphene. The graphene lattice vectors \vec{a}_1 and \vec{a}_2 are therefore used to label the carbon nanotubes as demonstrated in Fig. 2.1. The two lattice (or unit) vectors, indicated on the graphene honeycomb lattice, display the graphene unit cell by the enclosed rhombus. Only two carbon atoms at positions $\frac{1}{3}(\vec{a}_1 + \vec{a}_2)$ and $\frac{2}{3}(\vec{a}_1 + \vec{a}_2)$ are found in the unit cell. Both vectors are of length $|\vec{a}_1| = |\vec{a}_2| = a_0 = \sqrt{3}a_{c-c} = 2.46 \text{ \AA}$, where $a_{c-c} = 1.42 \text{ \AA}$ is the nearest neighbor distance [12]. The two unit vectors (\vec{a}_1 and \vec{a}_2) in real space and their correspondence reciprocal space unit vectors (\vec{k}_1 and \vec{k}_2) are expressed as:

$$\vec{a}_1 = \left(\frac{\sqrt{3}a_0}{2}, \frac{a_0}{2} \right) \quad \vec{k}_1 = \left(\frac{2\pi}{\sqrt{3}a_0}, \frac{2\pi}{a_0} \right) \quad (2.1)$$

2. Theoretical background

$$\vec{a}_2 = \left(\frac{\sqrt{3}a_0}{2}, -\frac{a_0}{2} \right) \quad \vec{k}_2 = \left(\frac{2\pi}{\sqrt{3}a_0}, -\frac{2\pi}{a_0} \right) \quad (2.2)$$

The chiral vector $\vec{c} = n_1\vec{a}_1 + n_2\vec{a}_2 \equiv (n_1, n_2)$ is the vector along which the graphene layer is rolled-up into a cylinder to form a particular nanotube. Its circumference is therefore equal to the chiral vector length, or alternatively the pair of integers

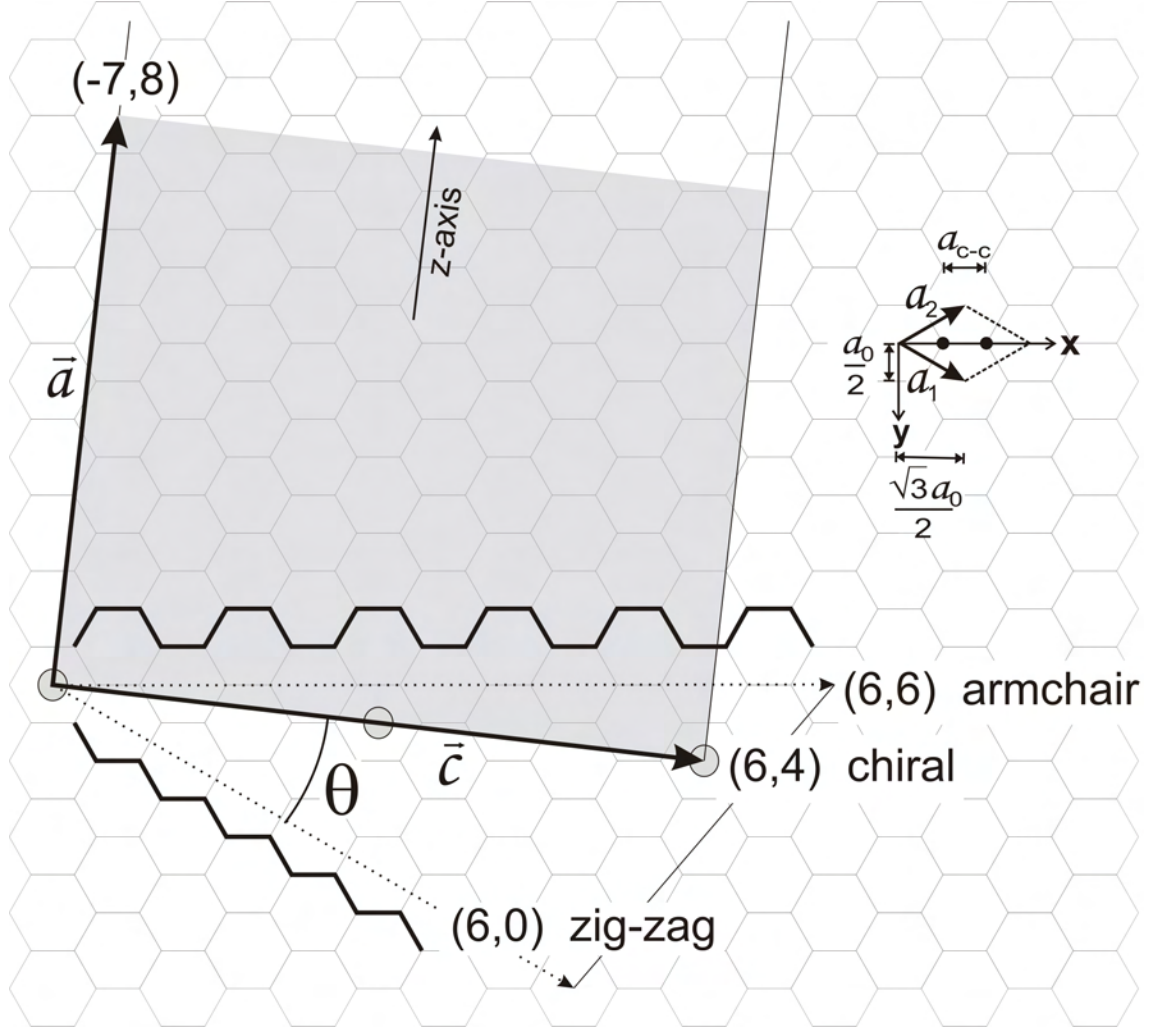


Figure 2.1.: Schematic illustration of a 2D graphene lattice. \vec{a}_1 and \vec{a}_2 are the graphene unit vectors at an angle of 60° with respect to each other. A black circle (carbon atom) exists at all lines-intersections. The scheme displays the chiral vector (\vec{c}) of a chiral (6,4) tube with its graphene-lattice points (open circles), of a (6,0) zig-zag and of a (6,6) armchair nanotube. The last two are shown with dotted arrows. The z -axis of a tube is always perpendicular to its \vec{c} vector. $\vec{a} = -7\vec{a}_1 + 8\vec{a}_2$ is the smallest lattice vector of the chiral (6,4) tube. The resultant grey rectangle is the unit cell of this nanotube. Zig-zag and armchair motifs are bold-highlighted. Adapted from Ref. [12].

(n_1, n_2) . Different chiral vectors can result in different properties for the nanotubes. For example, a small difference in chiral vector can alter the tube character from metallic to semiconducting and vice versa, as well as the number of atoms in the tube's unit cell. This applies even for tubes with a similar diameter, but with different (n_1, n_2) . Three representative examples of chiral vectors for the three types of nanotubes are shown in Fig. 2.1. The open-circles drawn on the chiral tube (6,4) with its corresponding chiral vector $\vec{c} = 6\vec{a}_1 + 4\vec{a}_2$ denote the graphene lattice-points. Their number is given by the greatest common divisor n of (n_1, n_2) , here $n = 2$, where the first and the last coincide when the sheet is rolled up. The chiral direction is defined by the chiral angle θ that is given by:

$$\cos \theta = \frac{n_1 + n_2/2}{\sqrt{N}} \quad \text{with} \quad N = n_1^2 + n_1 n_2 + n_2^2 \quad (2.3)$$

In principle the chiral angle θ of a particular tube is defined between 0° and 30° where tubes with $30^\circ \leq \theta \leq 60^\circ$ have an opposite helix, but otherwise equivalent to those with $0^\circ \leq \theta \leq 30^\circ$. Zig-zag tubes are denoted by $(n, 0)$ with $n_2 = 0$ and $\theta = 0^\circ$. Armchair tubes are denoted by (n, n) with $n_1 = n_2$ and have a chiral angle of 30° . The zig-zag and armchair tubes are both defined as *achiral* tubes in contrast to the *chiral* tubes.

The diameter of a generic carbon nanotube is directly proportional to the length of its chiral vector:

$$d = \frac{|\vec{c}|}{\pi} = \frac{a_0}{\pi} \sqrt{N} \quad (2.4)$$

Perpendicular to a particular chiral vector \vec{c} , the smallest corresponding graphene lattice vector \vec{a} defines the repeated translational period a ($= |\vec{a}|$) along the tube axis. Both are determined from the chiral indices (n_1, n_2) as follows:

$$\vec{a} = -\frac{2n_2 + n_1}{n\mathfrak{R}} \vec{a}_1 + \frac{2n_1 + n_2}{n\mathfrak{R}} \vec{a}_2 \quad (2.5)$$

and

$$a = |\vec{a}| = \frac{\sqrt{3(n_1^2 + n_1 n_2 + n_2^2)}}{n\mathfrak{R}} a_0 \quad (2.6)$$

where if the term $(n_1 - n_2)/3n$ gives an integer $\mathfrak{R} = 3$, otherwise $\mathfrak{R} = 1$. Following Eq. 2.5, the \vec{a} lattice vector of the (6,4) tube in Fig. 2.1 is $\vec{a} = -7\vec{a}_1 + 8\vec{a}_2$. Both \vec{c} and \vec{a} vectors form the unit cell of the nanotube (shown as grey rectangle).

2. Theoretical background

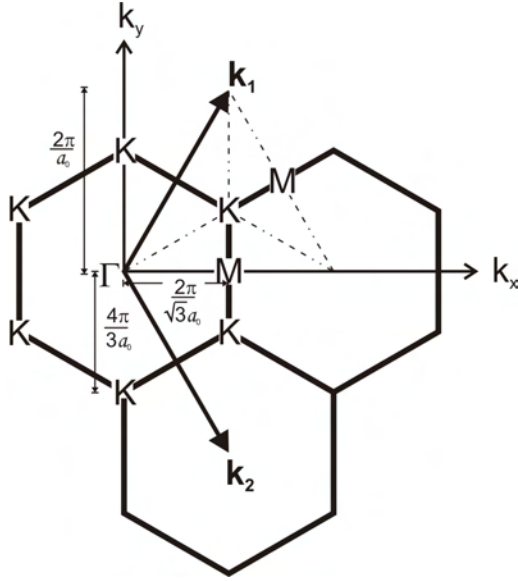


Figure 2.2.: The hexagonal Brillouin zone (BZ) of graphene displaying the reciprocal unit vectors $\vec{k}_1 = \left(\frac{2\pi}{\sqrt{3}a_0}, \frac{2\pi}{a_0}\right)$ and $\vec{k}_2 = \left(\frac{2\pi}{\sqrt{3}a_0}, -\frac{2\pi}{a_0}\right)$ at an angle of 120° with respect to one another. The high symmetry points Γ , K and M are indicated as well as some relevant dimensions. Adapted from Ref. [13].

The nanotube unit cell contains q hexagons and n_c carbon atoms, recalling two carbon atoms for the graphene unit cell:

$$q = \frac{2N}{n\mathfrak{R}} \quad (2.7)$$

$$n_c = 2q = \frac{4N}{n\mathfrak{R}} \quad (2.8)$$

Note that in achiral tubes, $q = 2n$ with n being the greatest common divisor of (n_1, n_2) .

The hexagonal Brillouin zone (BZ) of graphene is shown in Fig. 2.2 with its reciprocal unit vectors \vec{k}_1 and \vec{k}_2 , as defined in Eqs. 2.1 and 2.2. The high symmetry points Γ , K and M are also indicated. To a first approximation, the nanotube BZ is derived from that of graphene by the so called zone-folding approach, see section 2.2.1. In Fig. 2.1 it was defined that the z -axis is the tube axis. The continuous reciprocal lattice vector k_z is correlated to the translational period a along the z -axis of the infinitely long tube, where its length is given by:

$$k_z = 2\pi/a \quad (2.9)$$

In contrast, any wave vector along the circumference of the nanotube is quantized by the following boundary condition:

$$m \cdot \lambda = |\vec{c}| = \pi \cdot d \quad (2.10)$$

which defines the quantized k_{\perp} wave vector:

$$k_{\perp,m} = \frac{2\pi}{\lambda} = \frac{2\pi}{|\vec{c}|} \cdot m = \frac{2}{d} \cdot m \quad (2.11)$$

with m an integer ranging between $-n+1, \dots, 0, 1, \dots, n$ in achiral tubes (recall $q = 2n =$ number of hexagons in the nanotube unit cell). The first BZ of the nanotube consists therefore of q parallel lines along the tube axis. The lines are separated from each other by the magnitude of the quantized wave vector $k_{\perp} = 2/d$ with $m = 1$.

Both \vec{k}_{\perp} and \vec{k}_z are derived from the four relations:

$$\vec{k}_{\perp} \cdot \vec{c} = 2\pi \quad , \quad \vec{k}_z \cdot \vec{c} = 0 \quad , \quad \vec{k}_{\perp} \cdot \vec{a} = 0 \quad , \quad \vec{k}_z \cdot \vec{a} = 2\pi \quad (2.12)$$

which after substitution yields their dependence on the reciprocal unit vectors:

$$\vec{k}_{\perp} = \left(\frac{2n_1 + n_2}{qn\mathfrak{R}} \right) \vec{k}_1 + \left(\frac{2n_2 + n_1}{qn\mathfrak{R}} \right) \vec{k}_2 \quad (2.13)$$

$$\vec{k}_z = \left(-\frac{n_2}{q} \right) \vec{k}_1 + \left(\frac{n_1}{q} \right) \vec{k}_2 \quad (2.14)$$

The 6 parallel lines ($q = 2n$, $n = 3$) of the BZ of an armchair (3,3) tube and the 12 parallel lines ($q = 2n$, $n = 6$) of the BZ of a zig-zag (6,0) tube are illustrated in Fig. 2.3. The *extra line indexed with $m = 0$* is the one that passes through the graphene Γ -point and corresponds to $\vec{k} = 0$, see Eq. 2.11. Independent of diameter, the line indexed by $m = n$ lies on top of a high-symmetry M-point of the graphene BZ in both armchair and zig-zag tubes. Further, in the case of zig-zag tubes, the $m = 2n/3$ line hits the K-point if $n/3$ is an integer, here the line $m = 4$. The boundary π/a of the nanotube BZ is given by π/a_0 and by $\pi/\sqrt{3}a_0$ in armchair and zig-zag tubes, respectively, which provides $q = 2n$ allowed k -lines of length $2\pi/a$. In general, the number of allowed k -lines increases/decreases with increasing/decreasing diameter, while their distance ($2/d$) from each other decreases/increases, respectively. Nevertheless, within the tube type (armchair or zig-zag) the BZ boundary remains the same.

2. Theoretical background

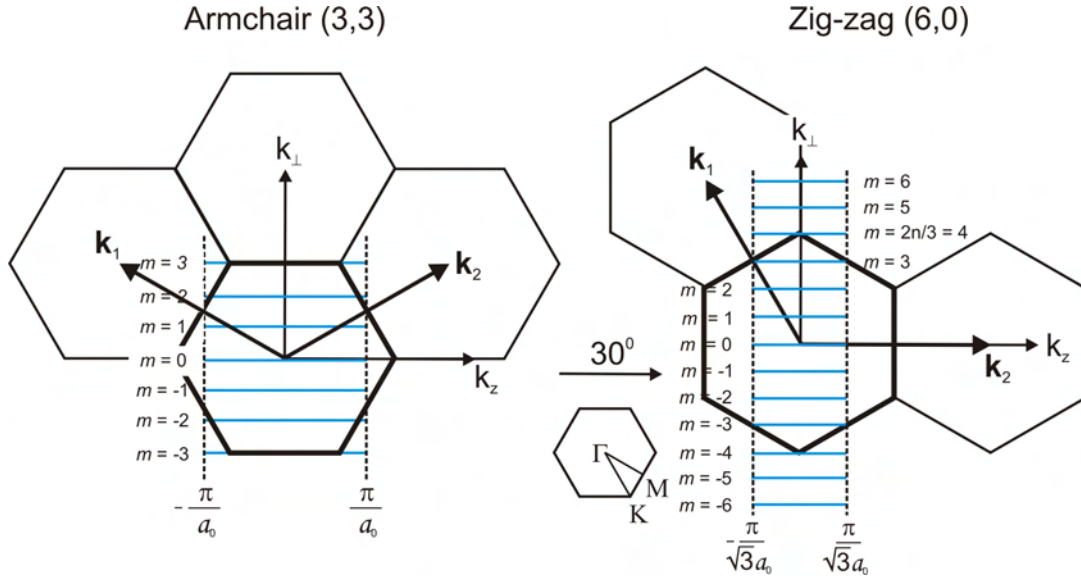


Figure 2.3.: An illustration of the BZ of an armchair (3,3) tube and a zig-zag (6,0) tube. The $2n$ parallel allowed k -lines comprise the nanotube BZ where they are indicated on top of the graphene BZ in order to emphasize their correlation. The reciprocal unit vectors \vec{k}_1 and \vec{k}_2 point along the ΓM direction and are at 120° angle with respect to one another. Lines with index m and $-m$ are defined equal due to symmetry reasons. Adapted from Ref. [12].

2.2. Electronic properties

The sp^2 -bonded carbon atoms in a carbon nanotube or a graphene network possess σ bonds in the plane of the monoatomic wall and π bonds that are above and below the plane of the monoatomic wall. Besides being responsible for the weak van-der-Waals interactions between tubes, the π bonds have a major effect on the electronic properties of carbon nanotubes. The σ bonds do not contribute to any physical effect like electronic transport or optical absorption occurring at the Fermi level, or at about 1-3 eV away from it, respectively. From the electronic band structure of graphene shown in Fig. 2.4 one observes that the smallest gap between the σ bonding and σ^* antibonding bands is ≈ 8 eV. For the commonly used visible range energies, no contribution to physical effects can occur as these bands are energetically too far from the Fermi level. In contrast, the bonding π and antibonding π^* bands cross the Fermi level at the K-point of the BZ, and thus strongly affect the electronic properties of both graphene and carbon nanotubes. Graphene is called a semimetal since the Fermi surface consists of only six distinct points (Fig. 2.4). This peculiar Fermi surface is responsible for the two possible modifications, metallic and semiconducting, of carbon nanotubes (section 2.2.1).

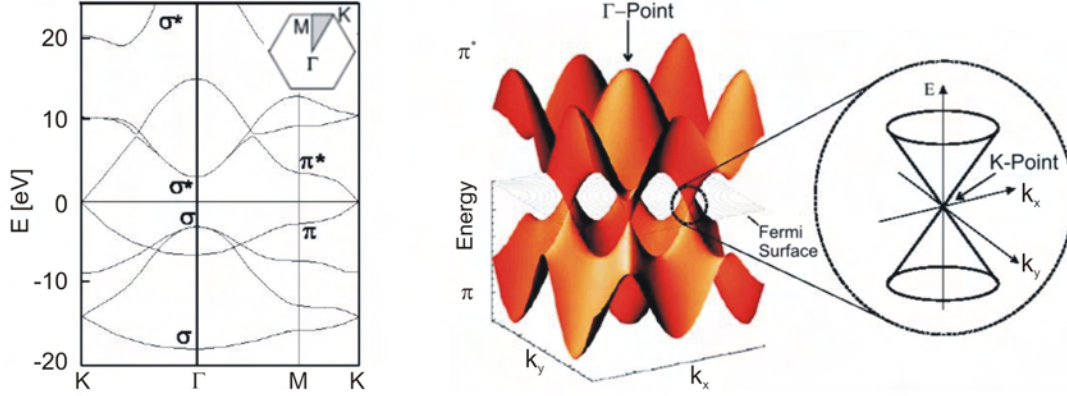


Figure 2.4.: On the left, the TB-calculated electronic band structure of graphene along the high symmetry Γ -M-K and Γ -K directions is shown. The Fermi level is defined at zero energy where the π/π^* and σ/σ^* bands are indicated. The inset shows the 1st BZ of graphene with the high symmetry directions (modified from Ref. [14]). On the right, a three-dimensional view of the graphene π/π^* bands is presented. The π bonding and π^* antibonding bands touch at the six K points. These 6 points are the Fermi surface. Modified from Ref. [15].

The electronic bands of a material can in principle be calculated by several approaches, for example *ab-initio* and tight-binding (TB). To date, many derivatives of these two basic approaches are further available for the calculation of the electronic band structure of graphene and carbon nanotubes. Neither theoretical calculations were performed in the work presented here. Information about the various methods can be found for example in Refs. [12,14]. Briefly, in order to calculate the full band structure of carbon nanotubes one has to know the graphene TB dispersion and the concept of zone-folding. Alternatively, one can solve the Schrödinger's equation self consistently to calculate the electronic energies of a particular tube. The zone-folding approach helps in understanding many of the carbon nanotube properties like the most unique property of being either metallic or semiconducting in character, depending on diameter and chirality.

2.2.1. Zone-folding approximation

The continuous wave vectors \vec{k}_z along the nanotube z -axis and the allowed quantized wave vectors \vec{k}_\perp around the nanotube circumference were defined in Eqs. 2.14 and 2.13, respectively. In Fig. 2.3, the allowed k -lines or wave vectors were plotted on top of the graphene BZ. This is in essence the zone-folding approach, also called the

2. Theoretical background

confinement approximation. It specifies the electronic band structure of the carbon nanotube by adapting the existing electronic energies of graphene along the allowed k -lines of the tube. The chiral indices (n_1, n_2) of a particular tube are the ones to determine the dimensions and orientation of the allowed k -lines, namely their length $(2\pi/a)$, their distance between each other $(2/d)$ and their number (q) . The latter is given by the greatest common divisor n .

The metallic or semiconducting character of SWNTs is determined by the Fermi surface of graphene. Following Fig. 2.4 we know that the valence and conduction bands cross at the graphene K-point of the BZ. Therefore, according to the concept of zone-folding, if the graphene K-point located at the Fermi surface matches an allowed k state of the carbon nanotube, the tube should be *metallic*. If no match occurs, the tube will possess an energy gap and be *semiconducting* in character.

As specified in Eq. 2.11, the electronic states (allowed k lines) of a general carbon nanotubes are confined to the vectors which satisfy the condition $\vec{k}_\perp \cdot \vec{c} = 2\pi m$. The K-point of the graphene BZ is defined via the reciprocal unit vectors (defined in Eqs. 2.1 and 2.2) to be located at $\frac{1}{3}(\vec{k}_1 - \vec{k}_2) = 4\pi/3a_0$, see also Fig. 2.2. It follows that a nanotube is metallic if the following expression is satisfied:

$$\vec{K} \cdot \vec{c} = 2\pi m = \frac{1}{3}(\vec{k}_1 - \vec{k}_2) (n_1 \vec{a}_1 + n_2 \vec{a}_2) \stackrel{\text{Eqs. 2.1+2.2}}{=} \frac{2\pi}{3} (n_1 - n_2) \quad (2.15)$$

or in other words if $3m = n_1 - n_2$, *i.e.*, if $n_1 - n_2$ is a multiple of three, the tube is *metallic* in character .

Alternatively, the K-point can be projected along the nanotube axis. Such procedure provides the k_z vector $[0, \frac{\pi}{a}]$ for metallic nanotubes at which the valence and conduction bands cross in the nanotube BZ:

$$\vec{K} \cdot \vec{a} = \frac{1}{3}(\vec{k}_1 - \vec{k}_2) \left(-\frac{2n_2 + n_1}{n\mathfrak{R}} \vec{a}_1 + \frac{2n_1 + n_2}{n\mathfrak{R}} \vec{a}_2 \right) = 2\pi k_z \quad (2.16)$$

which yields the k_z after substituting for the unit vectors:

$$k_z = \begin{cases} 0 & \text{if } \mathfrak{R} = 1, \text{ i.e., } (n_1 - n_2)/3n \text{ is not integer} \\ 1/3 & \text{if } \mathfrak{R} = 3, \text{ i.e., } (n_1 - n_2)/3n \text{ is integer} \end{cases}$$

For zig-zag and chiral metallic tubes with $\mathfrak{R} = 1$, the valence and conduction bands

cross at the Γ -point ($k_z = 0$)¹, while for armchair metallic tubes with $\mathfrak{R} = 3$ the bands cross at $k_z = \frac{2\pi}{3a}$.

The zone-folding approach has a big advantage of providing physical insights in a simple way as was shown in the case of metallic *versus* semiconducting character. It directly provides the m quantum number of the confined electronic states and thus an optical transition energy can be determined directly from the band structure of the tube, keeping in mind that for light polarized along the tube z -axis, the selection rule reads $\Delta m = 0$ (section 2.4.2)². The zone-folding is further capable of explaining the trigonal warping effect [19], the electronic band structure changes with curvature (section 2.2.2) and even provides the nanotube's vibrational modes from the phonon dispersion of graphene (section 2.4.4).

2.2.2. Energy gaps in quasi-metallic nanotubes

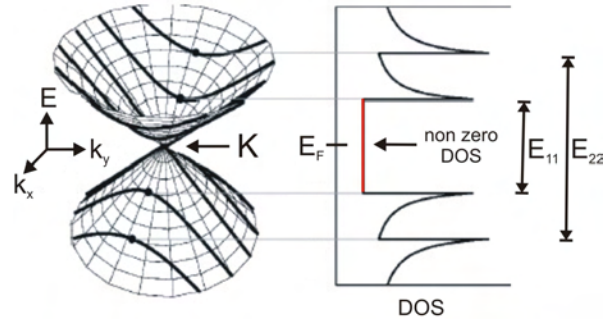
Nanotubes with an integer $(n_1 - n_2)/3n$ are defined metallic within the zone-folding approximation. Yet, experimental findings [20, 21] show that a small energy gap opens at the Fermi level of metallic zig-zag $(n, 0)$ and chiral (n_1, n_2) SWNTs. The gap opening in these SWNTs occurs as their finite curvature reduces the overlap between the π orbitals. For this reason metallic zig-zag and chiral tubes were named quasi-metallic. The statement was proven by means of low-temperature scanning tunnelling spectroscopy (STS) measurements, where Ouyang *et al.* [20, 21] demonstrated gap-like structures at the Fermi level of metallic zig-zag SWNTs. It was established that these quasi-metallic zig-zag tubes are in fact small-gap (few meV) semiconductors, where their gap is inversely proportional to their radius. A model was further developed. It explains that since a reduction in the overlap of nearest neighbor π orbitals occurs due to curvature, a shift of the Fermi vector \vec{k}_F from the K-point of the graphene BZ takes place. In quasi-metallic zig-zag tubes, the vector shifts away from the K-point, perpendicular to the allowed k -line direction. Consequently, the allowed k -line does not pass through \vec{k}_F , leading to an opening of a small-energy gap at the Fermi level. This model is valid also for chiral quasi-metallic SWNTs. Later, Kleiner *et al.* [22] showed the dependence of the band-gap on chiral

¹The valence and conduction bands of semiconducting tubes, chiral and zig-zag metallic tubes cross at the Γ -point ($\mathfrak{R} = 1$).

²Strong excitonic effects renormalize the transition energies so the observed optical transition energies are in fact exciton energies and not the actual interband transition energies [16]. Recent study by Martty *et al.* [17] have reported excitons' binding energy of about 270 meV for 1.4 nm diameter SWNTs. Similar results were previously obtained by Dukovic *et al.* [18].

2. Theoretical background

Figure 2.5.: The derivation of the DOS of a metallic tube (right) via its electronic band structure (left), given by the bold cutting lines on the cones. The formation of the vHSs in the DOS of the 1D system is shown, where in the vicinity of the Fermi level (marked in red), $\text{DOS} \propto 1/d$. E_{11} and E_{22} are the 1st and 2nd optical transition energies. Modified from Ref. [13].



angle, *i.e.*, the smaller the chiral angle the larger the band-gap. In contrast to the gap opening in zig-zag tubes, in metallic armchair tubes the Fermi wave vector \vec{k}_F moves parallel to the allowed k -line and thus armchair nanotubes always remain metallic [21].

2.2.3. Density of states (DOS)

Most of the differences between the electronic properties of graphene and carbon nanotubes result primarily from the reduced dimensionality. The density of states (DOS) is an essential quantity in experimental study of electronic properties, and it defines the number of electrons which are available at a given energy range for a specific system. In bulk semiconductors, the DOS increases approximately as the square root of the energy above the band gap. Also in 2D solids, the DOS shows a general increase in energy. Yet, in 1D systems the DOS is proportional to the inverse of the square root of energy and exhibits a decaying tail between maxima, also called van Hove singularities (vHSs). Carbon nanotubes show a 1D DOS as demonstrated in Fig. 2.5. Finally, 0D systems display δ -function DOS.

Figure 2.5 schematically demonstrates how the DOS of a metallic carbon nanotube is obtained via its electrical band structure. Here, the band structure of the tube is given by the cutting lines marked on the 2D cone-shaped energy dispersion around the K-point of the graphene BZ. Each line forms a van Hove singularity (vHS) in the DOS, shown as a local maximum except for the two lines crossing at the K-point. The non-zero DOS at the Fermi level (marked in red) is the result of such line-crossings that represent a metallic character for the nanotube. Its magnitude is inversely proportional to the tube diameter, $\text{DOS} \propto 1/d$. In contrast, the DOS is zero at the Fermi level for the case of a semiconducting tube, where no such crossing at the K-point exists. Figure 2.5 also shows the optical transition energies

between the first and second pairs of vHSs, or alternatively between the valence and conduction bands, E_{11} and E_{22} , respectively.

2.3. Electrical transport in SWNTs

For the truly metallic armchair tube, the valence and conduction bands cross at the Fermi level just as in the case of graphene. The two crossing bands provide the tube with two conducting channels at and close to the Fermi level, where in each of these bands, two electrons of opposite spins can co-exists. Consequently, an armchair tube with transparent contacts to metal electrodes should have the theoretical quantum conductance and resistance limits of:

$$G_{\text{nt}} = 2G_0 = \frac{4e^2}{h} \approx 150 \mu\text{S} \quad R_{\text{nt}} = \frac{h}{4e^2} \approx 6.5 \text{ k}\Omega \quad (2.17)$$

where $G_0 = 2e^2/h \approx 75 \mu\text{S}$ [12].

Different band structures are obtained for a truly metallic, a quasi-metallic and a semiconducting nanotube. The various band structures are illustrated in Fig. 2.6 which displays a quasi-metallic (12,0) zig-zag, a semiconducting (11,0) zig-zag, and an armchair (6,6) nanotube band structure. In the case of the armchair tube, the two bands $m = n = 6$ conduct the current while in the case of quasi-metallic zig-zag or chiral nanotubes, a small energy gap of few meV ($< k_B T$) exists due to the nanotube curvature (section 2.2.2). This gap is important at low-temperatures and can suppress electron transport. However, at room-temperature, the thermal energy is larger than the gap and the tubes show metallic behavior. Semiconducting tubes

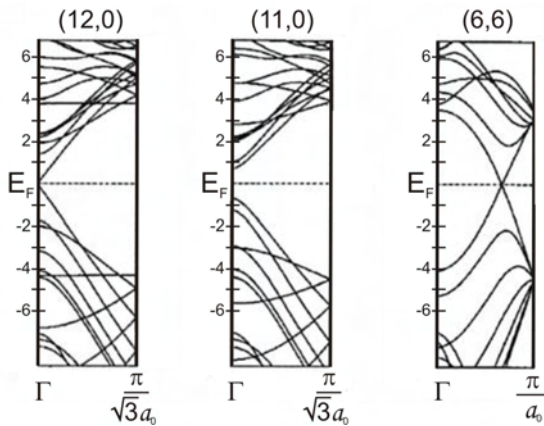


Figure 2.6.: The electronic band structures of a quasi-metallic zig-zag tube (12,0), a semiconducting zig-zag tube (11,0) and an armchair tube (6,6). E_F is set at zero energy. Modified from Ref. [23].

2. Theoretical background

possess an energy-gap of $\approx 0.5\text{-}1$ eV, where both zig-zag and semiconducting tubes have their DOS singularities at the Γ -point.

Room-temperature measurements of conductance *versus* gate-voltage (V_G) can distinguish between the two character types (see also section 4.3). In the case of metallic tubes, the conductance is V_G independent, with the crossing bands providing conducting electrons independently on the V_G , *i.e.*, the gate potential does not change the number of conduction channels. On the other hand, the conductance in semiconducting tubes is strongly affected by the V_G and can change by orders of magnitude. It is further accompanied by hysteresis [24,25] and it is asymmetric above and below the Fermi level, E_F . The tubes conduct at a negative V_G , which is smaller in absolute value than the positive V_G for the non-conducting state. This trend was initially interpreted to occur due to a p-type doping of the tube [26,27]. However, a few years later it was shown by Heinze *et al.* [28] that the asymmetry in the conducting channels is due to a Schottky barrier (SB) at the tube-metal interface³ rather than to a doping of the tube by oxygen [26,27]. It is known that the Schottky barrier at the nanotube/electrode interface is sensitive to the metal electrode work function and that the work functions are in turn sensitive to gas adsorbents [29]. In the work of Heinze *et al.* [28] one field-effect transistor device (FET) was exposed to different oxygen concentrations while another was doped by increasing potassium concentration. The current *versus* gate-voltage characteristics (Fig. 4 in Ref. [28]) were then investigated, showing qualitatively the current- V_G changes for the case of doping *versus* the case of changing the work function. If the work function is changed it leads to a lowering of the conductance for one sign of the V_G and to an increase for the opposite sign. However, the range of V_G in which the device is "OFF" stays the same. If the oxygen was to dope the tube, the minimum of the curve would have been shifted. On the other hand, for the potassium-doped device, the minimum of the curves (the V_G range at which the device is "OFF") shifts to negative/positive V_G for n-type/p-type doping, respectively. Therefore, it was concluded that the effect of oxygen exposure was not to dope the tube, but rather to change the work function of the exposed electrode [28]. Furthermore, due to the presence of a SB in FETs, contact geometry is essential, as one must consider the effect of the electric-field at the nanotube/electrode interface for better operating FETs.

³A Schottky barrier for holes or electrons can result at the interface of a semiconductor and a metal.

2.3.1. Defect-induced elastic scattering in metallic SWNTs

Single-wall metallic nanotubes should theoretically exhibit the conductance limit of $2G_0$, or a resistance of $\approx 6.5 \text{ k}\Omega$. However, most measured conductances display a much lower value than the theoretically expected one. In a two-terminal resistance measurement, which typically displays a value on the order of $\text{M}\Omega$ s, most of the applied voltage drops at the metal-tube contacts, and a tunnelling process dominates the transport. This is unfortunately the general case with varying contact resistances depending on device processing. Nevertheless, the origin for this high contact resistance is not yet completely understood and remains even now an open question. Although a few experiments with highly transparent contacts and nearly theoretical resistance values have been reported [30, 31], most cases exhibit resistances on the order of tens to hundreds of $\text{k}\Omega$. Apart from contacts, this is due to the fact that real nanotubes are not perfect as assumed in theoretical calculations. SWNTs have structural defects which elastically scatter electrons, where additionally the electrons can be inelastically scattered by phonons (section 2.3.2).

In metallic tubes, the elastic scattering of electrons near the Fermi level is suppressed. One explanation for this suppression comes from the fact that the wave functions near the E_F are smeared along the circumference. When a disorder like an impurity, a pentagon-heptagon defect or other kind of defect, exists in an arm-chair nanotube wall, the electron senses only a reduced potential as it is averaged over the whole circumference. In larger diameter tubes, the impurity influence will be smaller or even negligible [32]. This argument holds up to the case where the diameter is as big as to cause higher-lying bands to be too close in energy to the crossing $m = n$ bands. For such a scenario, electron backscattering occurs between different m -bands and ballistic transport fails. Symmetry arguments are another way to explain the elastic scattering suppression in metallic tubes and can be found in Ref. [12]. The conclusion of both is however the same, some of the metallic tubes can reach the ballistic transport limit, while others can not.

Finally, ON state semiconducting tubes experience no elastic scattering suppression. The argument here is that the conducting electrons have the same irreducible representation and thus backscattering is allowed. This is in contrast to the case of metallic tubes which their crossing bands belong to different irreducible representations.

2.3.2. High-bias electron-phonon scattering in metallic SWNTs

Metallic SWNTs can be envisioned as tiny interconnectors in electrical circuits, as it is known that some of them can reach the ballistic transport limit. However, in the high-bias regime, electron-phonon scattering processes take place. These interactions result in a very small mean-free-path for the electrons, *i.e.*, very small scattering lengths which bring the electrical transport to current saturation. Various phonons like the acoustic, optical high-energy or zone-boundary phonons can interact with the electrons, which in many cases are the dominant paths for relaxation processes in SWNTs. In Fig. 2.7, a schematic illustration of the electronic band structure is shown for a metallic SWNT. Like in graphene, the electronic gap is zero at the crossing π bands for both equivalent K and K'=2K BZ points⁴. The scattering processes at both Γ and K points are assigned for $q \approx 0$ and $q \approx 4\pi/3a$ phonon wave vectors, respectively. At low-electric-field (small source-drain voltage, V_{SD}) or in the low-energy regime, electron-phonon coupling processes occur with either $q \approx 0$ or $q \approx 4\pi/3a$ acoustic phonons, as indicated by the red arrows in Fig. 2.7. The electron reverses its propagation-direction as it scatters from subband 1 into subband 2 thus, changing its momentum but maintaining its energy. A further increase in electric-field (higher V_{SD}) accelerates the electrons to such energies that they can emit high-energy phonons with wave vectors $q \approx 0$ and $q \approx 4\pi/3a$ (zone-boundary phonons), as illustrated by the black arrows. These phonons are of $\hbar\omega_{\Gamma}$ and $\hbar\omega_K$ energy, respectively. In the upper-left process, an electron is back scattered between subbands (1 and 2) under the emission of a high-energy phonon. The electron preserves its momentum while its energy is lowered by a phonon energy of $\hbar\omega_{\Gamma}$. Alternatively, the electron can relax by emitting a zone-boundary phonon as in the upper-right process. Here, the electron is back scattered between the two subbands (1 and 2) of the two equivalent K points, where both its momentum and energy are changed. It loses $\hbar\omega_K$ energy and its momentum is changed by $\approx 4\pi/3a$. An electron can also be forward scattered into the same subband as illustrated in the lower-panel of Fig. 2.7.

⁴As long as the bias is smaller than 1V, the initial (k) and final ($k+q$) electron states stay close to the K or 2K graphene points, as the electron is scattered by a q or $-q$ phonon. The conservation of energy reads $E_{(k+q)j} = E_{ki} \pm \hbar\omega_{q\eta}$ where \pm refers to the absorption/emission of a q phonon in branch η , and i and j are the electron bands [33].

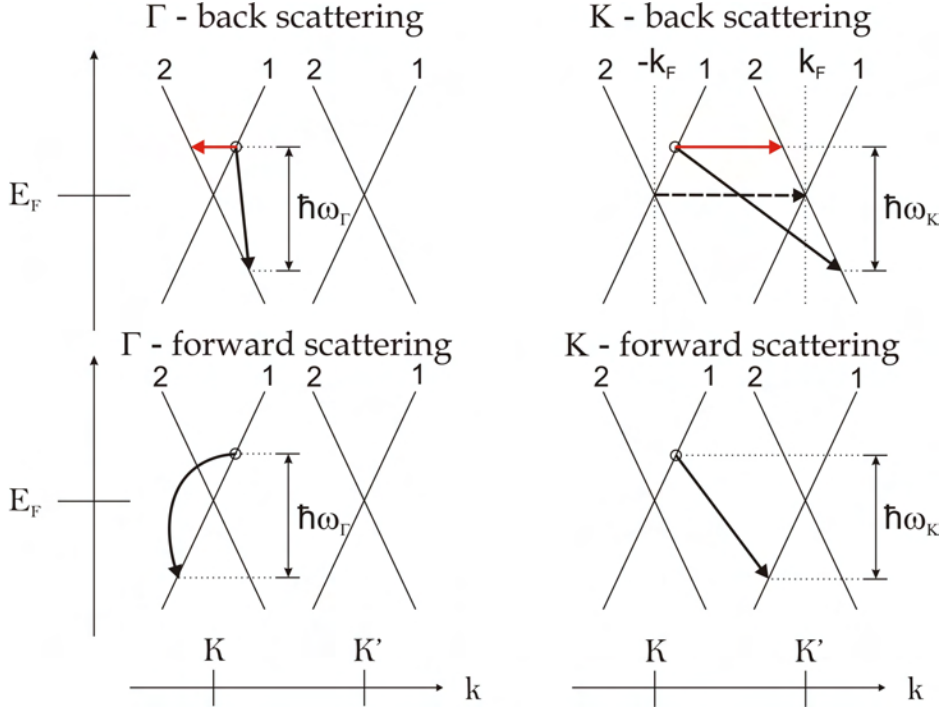


Figure 2.7.: Schematic drawing of the various phonon scattering processes in a metallic SWNT, illustrated at the K and K' graphene BZ points. Γ and K refer to $q \approx 0$ and $q \approx 4\pi/3a$ phonons, respectively (the latter refers to scattering between k_F and $-k_F$). Red/black arrows indicate the two possible electron back scattering by low-energy acoustic phonons, and the four possible electron scattering processes by high-energy and zone-boundary phonons, respectively. Broken arrow denotes the K vector connecting the two equivalent K and K' points. Modified from Ref. [33].

The optical phonons required to scatter an electron between two subbands are of energies in the range 100 - 200 meV (small- q phonons), while those with the energy range 100 - 160 meV are the (large- q) zone-boundary phonons⁵. At low V_{SD} , the moderately accelerated electrons lack the energy required to emit high-energy phonons, and therefore only very low-energy acoustic phonons are emitted. Nevertheless, at high V_{SD} , the electrons can be accelerated to have enough energy for the emission of optical high-energy and zone-boundary phonons. The relaxation can occur as long as an electronic state is available for the specific scattering process. Likewise, if the energy difference between the occupied and unoccupied states is less than 100 - 200 meV, negligible electron-phonon coupling processes take place, *i.e.*, merely with acoustic phonons. Following this theory, the current saturation I_0 for a

⁵In armchair tubes, such scattering requires a change in the vertical mirror plane parity, see appendix A.

2. Theoretical background

SWNT given in Eq. 2.18 was calculated by Yao *et al.* [9] to vary between 15 - 30 μA for $E_{\text{ph}} = 100 - 200$ meV phonon energies:

$$I_0 = \left(\frac{4e}{h} \right) E_{\text{ph}} \quad (2.18)$$

Various experimental results [9–11], as well as in the present work (section 4.6.3), have shown that individual SWNTs can conduct currents in this range and that at high-bias the current saturates. Note that the I_0 defined in Eq. 2.18 does not depend on tube length, L . The I - V_{SD} curves in these experiments show a linear dependence in the low-bias regime. In the high-bias regime though the curves saturate, in agreement with the electron-phonon coupling processes described above. At higher applied voltage, the electrons can reach the required energy faster with a consequent relaxation via phonon emission.

Since optical high-energy and zone-boundary phonons do not exist at room temperature, one must assume that they relax instantaneously after their emission by the electrons. Figure 2.8 illustrates the occurrences to an electron in the high-bias regime. The electron accelerates within a length l_{T} under the applied electric field \vec{E} . At the same time, it gains the required energy for the emission of an optical phonon. Once obtained, the electron scatters on a length scale of the mean-free-path (l_{ph}) of a high-energy phonon ($E_{\text{ph}} \approx 0.2$ eV) or a zone-boundary phonon ($E_{\text{ph}} \approx 0.16$ eV).

In order to evaluate both l_{T} and l_{ph} , one needs to consider the change in the electron momentum k under an applied electric field, \vec{E} :

$$\hbar \frac{dk}{dt} = e|\vec{E}| \quad (2.19)$$

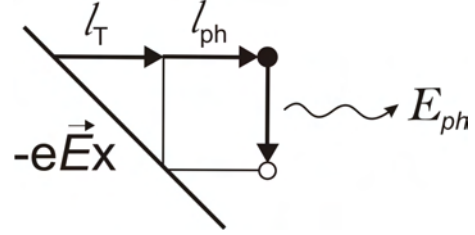
If the linear dispersion $dE/dk = \hbar v_{\text{F}}$ at the Fermi level is then inserted into Eq. 2.19, the mean-free path l_{T} of an electron before it scatters is found⁶

$$l_{\text{T}} = \frac{E_{\text{ph}}}{e|\vec{E}|} = \left(\frac{E_{\text{ph}}}{\text{eV}} \right) \cdot L \quad (2.20)$$

Once the electron has reached the threshold energy, it will scatter on a length scale l_{ph} , the high-energy phonon scattering mean-free path. The total length that the

⁶ $dE = e\vec{E}dx = \hbar v_{\text{F}} \cdot dk \Rightarrow dx \equiv l_{\text{T}} = \frac{dE}{e\vec{E}}$

Figure 2.8.: Schematic illustration of the scattering lengths involved in the high-bias regime. l_T and l_{ph} are the electron and phonon mean-free paths, respectively. Taken from Ref. [10].



electron propagates before scattering is the sum $l_T + l_{ph}$, as shown in Fig. 2.8. For large enough tube lengths (L), the total scattering length is determined by l_T , because $l_T \gg l_{ph}$.

The total resistance (high-bias and low-bias resistances) is therefore,

$$R = R_{\text{high}} + R_{\text{low}} = \left(\frac{\hbar}{4e^2} \right) \left(\frac{L}{l_T} \right) + R_{\text{low}} \stackrel{\text{Eq. 2.20}}{=} \frac{V}{I_0} + R_{\text{low}} \quad (2.21)$$

with I_0 as defined in Eq. 2.18. R_{low} is the sum of a voltage-independent resistance (contact resistance) plus the constant intrinsic quantum resistance, $R_{\text{nt}} = 6.5 \text{ k}\Omega$, *i.e.*, $R_{\text{low}} = R_{\text{contact}} + R_{\text{nt}}$. However, if L is adequately small, the scattering length is determined by l_{ph} , because $l_T \ll l_{ph}$. For very short tube segments, a lower applied voltage is required to obtain a sufficient \vec{E} that can accelerate the electron to the point it relaxes via phonon emission, compared to a longer segment with the same diameter. For this short channel, the experimental scattering length is l_{ph} and the total resistance is:

$$R = R_{\text{high}} + R_{\text{low}} = \left(\frac{\hbar}{4e^2} \right) \left(\frac{L}{l_{ph}} \right) + R_{\text{low}} \quad (2.22)$$

Recent experimental results [9–11] for the mean-free path of electrons in the high-bias regime have shown a general agreement. The reported values for room temperature measurements were on the order of 10 - 15 nm and $> 1.6 \text{ }\mu\text{m}$ for the electron high-energy phonon scattering and for the electron acoustic phonon scattering, respectively.

2.4. Raman Spectroscopy

Raman spectroscopy is a well-established experimental technique for the characterization of carbon materials. The recorded spectra can provide information about their physical properties and quality, even in cases where only a small amount of

2. Theoretical background

the material is available. In the case of carbon nanotubes, the Raman scattering signal is resonantly enhanced due to the van Hove singularities (vHSs) in the electronic band structure, and thus, even individual tubes can be investigated. In the present work, the Raman technique was used on SWNTs to obtain information about their vibrational properties, their metallic or semiconducting character and to get insight on the various electron-phonon coupling processes occurring on the level of an individual metallic SWNT.

2.4.1. First-order Raman scattering

A typical *First-order* Raman scattering process involves (in the framework of quantum mechanics) the following steps:

1. Absorption of an incoming photon with energy $\hbar\omega_1$ while creating an electron-hole pair.
2. The electron scatters inelastically by emitting/absorbing a phonon of energy $\hbar\omega_{\text{ph}}$.
3. Recombination of the electron and hole under the emission of the scattered photon of energy $\hbar\omega_2$.

Equations 2.23 and 2.24 express the energy and momentum conservation in the Raman process, respectively:

$$\hbar\omega_1 = \hbar\omega_2 \pm \hbar\omega_{\text{ph}} \quad (2.23)$$

$$\vec{k}_1 = \vec{k}_2 \pm \vec{q} \quad (2.24)$$

where \vec{k}_1 and \vec{k}_2 denote the electron wave vector before and after scattering with a phonon of wave vector \vec{q} , while the \pm sign stands for the Stokes (S) and anti-Stokes (AS) scattering processes⁷.

Three *first-order* Raman scattering processes are possible: the non-resonant, the single-resonant and the double-resonant Raman scattering. Figure 2.9, schematically illustrates the various processes. The solid lines denote real electronic states, which for a SWNT indicate a vHS pair, *i.e.*, an optical transition energy, E_{ii} . The

⁷The emitted photon has a lower energy for S-process and higher energy for AS-process.

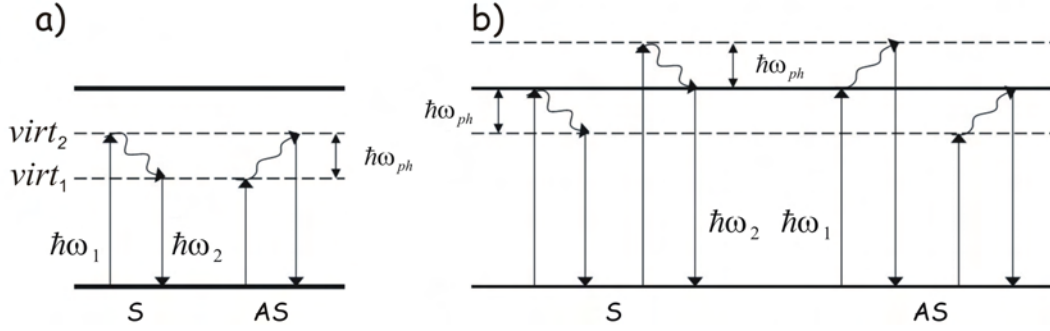


Figure 2.9.: Schematic illustration of the Stokes and anti-Stokes electron-phonon scattering processes. (a) Two possible non-resonant and (b) four possible single-resonant Raman scattering processes. Solid/broken lines denote real/virtual electronic states, respectively. The energy difference between solid lines indicate an optical transition E_{ii} in a SWNT. Note that while the broken lines indicate virtual states for the single-resonant case, they indicate *real* states for the double-resonant scattering processes. $\hbar\omega_1$, $\hbar\omega_{ph}$ and $\hbar\omega_2$ stand for incoming photon energy, phonon energy and outgoing photon energy, respectively, in both *a* and *b*. S and AS are abbreviations of Stokes and anti-Stokes. Modified from Ref. [12].

broken lines indicate virtual electronic states. Following the sequence of events listed above for the first-order Raman scattering, the Stokes process in part (a) of Fig. 2.9 illustrates how a photon of energy $\hbar\omega_1$ excites an electron into the virtual state, $virt_2$. The excited electron is then scattered under the emission of $\hbar\omega_{ph}$ phonon into the virtual state $virt_1$, and finally recombines with the hole under the emission of a photon of energy $\hbar\omega_2$. A similar sequence takes place for the anti-Stokes process, however, here the electron is scattered between the virtual electronic states by absorbing a phonon of $\hbar\omega_{ph}$ energy, and the order of virtual states is reversed. Since in both Stokes and anti-Stokes processes the intermediate electronic states are all virtual, *non-resonant* Raman scattering processes occur. Part (b) of Fig. 2.9 illustrates the two Stokes and two anti-Stokes possible scattering routes for *single-resonant* Raman scattering processes. Here, the photon energy matches an incoming or an outgoing transition between two *real* electronic states. For a *double-resonant* Raman scattering process, the virtual electronic states drawn in Fig. 2.9 (b) have to be also real. For the picture given here though, the double-resonant scattering is obtained only for one particular laser wavelength.

All first-order processes described in Fig. 2.9 are limited to scattering of visible light by Γ -point phonons ($q \approx 0$). According to the single-resonance model, a resonance

2. Theoretical background

condition must further occur or no contribution to the Raman signal occurs, *i.e.*, the laser energy must match a given optical transition of the tube.

Nevertheless, higher-order processes, which follow the scheme of the double-resonant scattering, are also possible. These processes involve scattering by two phonons with wave vectors of opposite sign $\pm q$ (***second-order*** Raman scattering) or involve ***elastic-scattering*** by defects. In both cases the phonon wave vectors are bigger than zero, $q > 0$. For details see section 2.4.3.

2.4.2. The selection rules for Raman scattering in SWNTs

The Raman scattering selection rules in carbon nanotubes are easily found by considering the conservation of the quasi-angular momentum m and the parity along the horizontal mirror plane, σ_h (the parity applies only in achiral tubes, see appendix A). When taking into account only first-order scattering, *i.e.*, Γ -point phonons ($q \approx 0$) for vertical transitions in the visible ($\Delta k \approx 0$), the selection rules depend on the polarization of the electric field vector \vec{E} with respect to the nanotube z -axis⁸. Achiral nanotubes have a horizontal (σ_h) and a vertical (σ_v) mirror planes, where a z -polarized optical transition changes the horizontal mirror parity *i.e.*, $\sigma_h = -1$. For transitions polarized perpendicular to the tube axis, however, the horizontal mirror parity does not change, $\sigma_h = +1$. When a photon with an angular momentum ± 1 is absorbed, the transition from the valence to conduction band must fulfill the following conditions in order to conserve the total angular momentum. The first condition specifies that the m is kept constant if z -polarized light is applied, *i.e.*,

$$\Delta m = 0 \quad \text{for} \quad \vec{E} \parallel z - \text{axis} \quad (2.25)$$

while the second rule states that m should change by ± 1 if (x, y) -polarized light is applied on the tube:

$$\Delta m = \pm 1 \quad \text{for} \quad \vec{E} \perp z - \text{axis} \quad (2.26)$$

⁸If an external field \vec{E}_{ext} is applied along a sufficiently long tube, the formed charges are too far apart to form a polarization. If the \vec{E}_{ext} is applied perpendicular to the tube, the charges induced on its surface result in a polarization (\vec{P}) that opposes the external field and reduces the magnitude of the electric field in the tube (\vec{E}_{\perp}). This depolarization or antenna effect suppresses allowed optical transitions in tubes with \vec{E}_{\perp} [34].

When other scattering processes are also allowed, *e.g.*, defect-induced double resonance scattering processes (section 2.4.3), which involve large- q phonons, one has to additionally apply the *Umklapp*⁹ rules.

2.4.3. Double-resonant Raman scattering

Most Raman experiments on solids are performed in the backscattering configuration and utilize a light source in the visible spectral range. In such a setup, the extremely small wave vector of the incident light limits the scattering processes to first-order scattering of Γ -point phonons ($q \approx 0$) as the electron momentum must be conserved. In most Raman scattering experiments on solids, therefore, only Γ -point phonons can participate in the scattering process. However, an exception occurs in carbon nanotubes. Owing to their unique electronic band structure, double-resonant scattering processes contribute to the Raman spectrum. Such defect-induced processes employ typically large- q phonons and are *not* " Γ -point-phonons-restricted" as discussed below.

Only a few years back, the double-resonant Raman scattering process was realized to contribute significantly to the Raman spectrum of carbon materials. The shift with excitation energy of the disorder induced D-mode in graphite [35, 36] has evoked the recognition that double-resonant processes are involved, since it could not be explained by the well known first-order Raman processes, dominated by the $q \approx 0$ phonons, where the peak frequencies are independent of the laser energy.

Thomsen and Reich [37] were the first to explain the observed laser-energy dependence in graphite. They have demonstrated that the responsible mechanism for the frequency shift of the D-mode is defect-induced, double-resonant Raman scattering. The role of the defect is to elastically scatter back the electron to its original momentum (\vec{k}_i) after it was resonantly or non-resonantly scattered by a large- q phonon, so as to not violate the momentum conservation. It is for that reason that large- q phonon wave vectors can additionally contribute to the spectra of carbon nanotubes or of graphite.

In Fig. 2.10, a schematic illustration of the two linear electronic bands are shown, resembling the energy dispersion at the K-point of the graphene BZ. On the left, an

⁹As long as the scattering process remains within the 1st-BZ boundaries $[-\pi/a, \pi/a]$ m can be regarded as a conserved quantum number. However, once the BZ boundary is crossed, m is no longer conserved, and the scattering process is called *Umklapp* process. In such a case, the phonon wave vector q is corrected according to the Umklapp rules [12].

2. Theoretical background

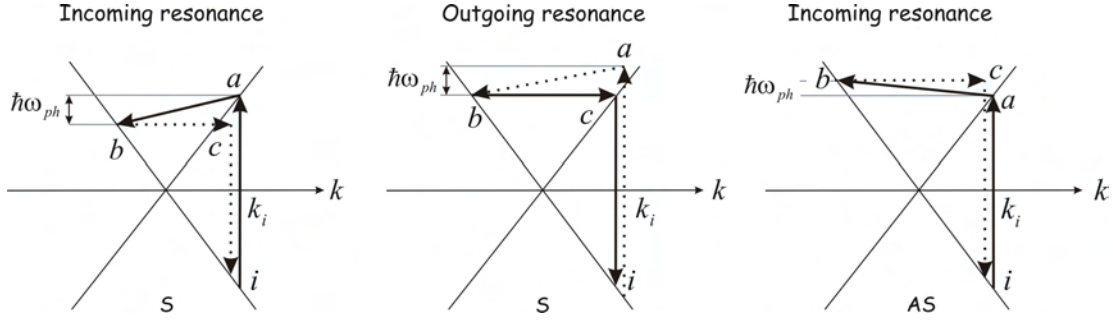


Figure 2.10.: Schematic illustration of both incoming and outgoing double-resonant Raman processes. Solid/dotted black arrows stand for resonant/non-resonant scattering processes. Left/middle schemes demonstrate an incoming/outgoing double-resonance Stokes (S) processes with the first two transitions in resonance/non-resonance. Right scheme illustrates an anti-Stokes (AS) process. \vec{k}_i indicates the initial electronic state, while \vec{k}_a, \vec{k}_b and \vec{k}_c indicate intermediate electronic states, with momentum conservation $\vec{k}_i = \vec{k}_c$. Note the larger wave vector in the AS process *versus* its equivalent S process in the left scheme. This results in a different S and AS peak frequencies for the same incoming photon energy, as seen by the energy magnitudes of the scattering phonons, $\hbar\omega_{\text{ph}}$. Adapted from Ref. [12].

incoming real transition occurs, initiated by the excitation of an electron from its ground- i to its intermediate a -electronic state. It can be rationalized from such picture that if we would increase/decrease the laser energy, the electron wave vector \vec{k}_i will simply increase/decrease to match the resonant transition. A double-resonance process implies that the excited electron at state a is for example resonantly scattered to state b under the emission of a phonon of energy $\hbar\omega_{\text{ph}}$ as shown in the left Stokes process of Fig. 2.10. The energy of the phonon is given by the energy difference between states a and b while the magnitude of q is determined by the length of its arrow. As mentioned above, a second scattering must bring back the electron to its original wave vector, here shown as intermediate electronic state c . The second scattering can be done elastically by a defect (displayed here) or inelastically by a second phonon, which results in a process called **second-order** Raman scattering. Finally, after returning to the wave vector k_i , the electron recombines with the hole. The middle scheme demonstrates an example of scattered light in resonance *i.e.*, an outgoing resonance process. In this picture, the excited electron reaches a virtual electronic state¹⁰ a , which scatters into state b by emitting a phonon. The electron is then scattered back by a defect and recombines with the hole. In contrast to the

¹⁰A virtual state has a lifetime on the order of 10^{-15} seconds.

example shown for an incoming Stokes resonance process, the last two transitions of the outgoing Stokes process are in *resonance*. On the right, an anti-Stokes process in an incoming resonance procedure is exemplified. In general, all the transitions in anti-Stokes processes are similar to those in Stokes processes, except for the absorption of phonons. Here, the electron absorbs a phonon of energy $\hbar\omega_{\text{ph}}$, while being scattered resonantly from state a to state b . In all of the above examples, the phonon that scatters the electron from state a into state b must have a larger wave vector than that of the electron *i.e.*, $q > k_i$. In total, there are four possible Stokes and four possible anti-Stokes processes.

2.4.4. The various Raman modes of SWNTs

In order to determine the full phonon dispersion of carbon nanotubes, the tubes must be in the form of single crystals. Since no such object exists, one compromise is to theoretically calculate the phonon dispersion by zone-folding the graphene BZ. It turns out that the more tractable zone-folding approximation predicts the phonon dispersion quite well as compared to the much more elaborate/slower but accurate *ab-initio* calculations, given in Fig. 2.11. On the left, the phonon dispersion of graphene with its optical and acoustic modes, *i.e.*, longitudinal (LO/LA), transverse (TO/TA) and out-of-plane (ZO/ZA) modes are shown. To achieve the phonon band structure of the (4,4) tube by the zone-folding procedure, slicing the graphene BZ in the direction of k_{\perp} is needed. The slicing occurs four times along the Γ -M direction for the armchair tube exemplified here, while for a general armchair tube it will be n times. Like in Fig. 2.3, the lines with $m = 0$ and $m = n$ lie on the graphene Γ -point and M-point, respectively. Each point where the vertical lines intersect with the phonon branches of the graphene sheet becomes a Γ -point phonon in the nanotube.

A comparison between the zone-folded and *ab-initio* calculated phonon dispersions reveals two obvious limitations; the zone-folding approach lacks both an acoustic mode and a non-zero frequency radial breathing mode at the Γ -point. Both are missing in graphite, and are indicated with thick red lines in the *ab-initio* calculated phonon dispersion of the (4,4) tube (lower part). Note that the slicing procedure for a zig-zag tube occurs along the Γ -K direction, here demonstrated in red for the (6,0) tube, with $m = 2n/3 = 4$ hitting the K-point (compare with Fig. 2.3).

2. Theoretical background

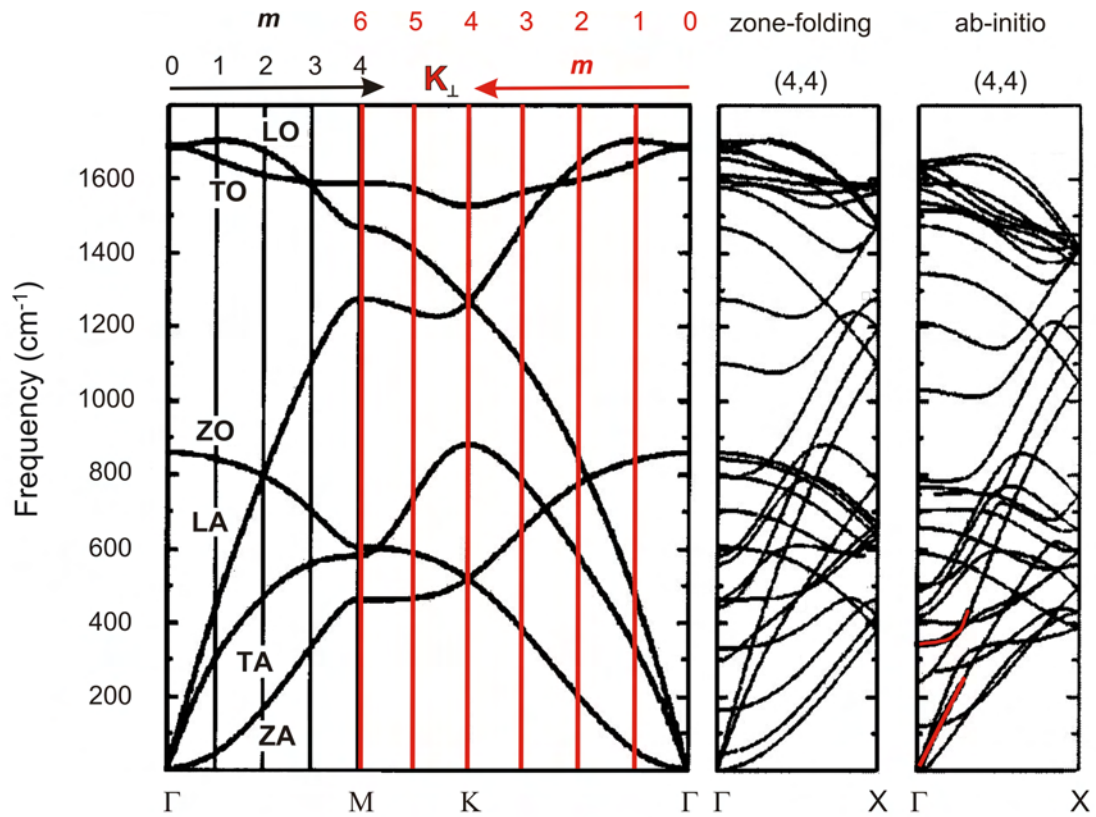


Figure 2.11.: The procedure of zone-folding the phonon dispersion of the graphene BZ (left) to construct the band structure of a specific nanotube, demonstrated here (black) for the armchair (4,4) tube. Thick red lines in the *ab-initio* calculations (using pseudopotential-density-functional theory) demonstrate the acoustic (twist) mode and the radial breathing mode branches that are missing in graphite. Also shown is the slicing procedure for a (6,0) zig-zag tube (red) however without a corresponding nanotube band structure. Modified from Refs. [12, 38].

The first-order Raman scattering spectrum is normally divided into three major regimes: (1) the low-frequency range of the radial breathing mode where the tube mimics a breathing-like vibration, (2) the intermediate range with the defect-induced vibrations and (3) the high-energy range where adjacent carbon atoms vibrate out-of-phase.

Radial breathing mode

The radial breathing mode (RBM) appears in the low-frequency range of the Raman spectrum ($100 - 400 \text{ cm}^{-1}$). This vibration causes all positions to expand and

contract in a coherent way along the radial direction, mimicking a breathing like movement. The diameter d of a SWNT is inversely proportional to the frequency of its RBM mode, as given by the following relation:

$$\omega_{\text{RBM}} = \frac{C_1}{d} + C_2 \quad (2.27)$$

where C_1 and C_2 are constants. In the beginning, C_2 was used to account for external forces *e.g.*, interaction with the substrate or van-der-Waals interactions between neighboring tubes in a bundle [39]. However, rather small changes in the RBM frequencies were found due to changes in the environment [40, 41], and thus C_2 is regarded today mainly as a fitting parameter. The value for C_1 is either calculated or found by best fit to many measurement data points and thus ranges from 218 to 248 cm^{-1}nm , for isolated nanotubes, as found by various groups. It is for that reason that a few percent error in the C_1 value is always present ($\sim 5\%$), which transforms into the same error for the diameter d . Based on the theory of the single-resonance model (section 2.4.1) only particular tubes are selected from a tube ensemble of different diameters at a specific laser energy. This dependence of the Raman frequency on excitation energy is called ***diameter-selective resonance***. Following this model, any variation of the Raman spectrum with laser energy implies that different tubes are resonantly excited [41].

Defect-induced D-mode

The D-mode belongs to the intermediate range of the Raman spectrum, extending between 1200 to 1400 cm^{-1} . The D-mode in graphite was observed for the first time in 1970 [42] and was proven to be disorder-induced, via experiments in which the crystallite size of graphite was progressively decreased and the intensity for this mode linearly increased. Ten years later, it was discovered by Vidano *et al.* [35] that the frequency of this mode changes, *i.e.*, increases by about 50 cm^{-1}/eV with laser energy. From section 2.4.3, it is clear that this dependence results from a double-resonance process, enhancing a different phonon wave vector for each excitation energy wavelength. The shift in phonon frequency is a consequence of a dispersive phonon band for which a different wave vector fulfills the double resonance condition. The defect-induced D-mode involves K-point rather than Γ -point phonons. In carbon nanotubes, the D-mode corresponds to the one in graphite except that it is found to have a slightly smaller frequency [43, 44]. Possible defects in a nanotube

2. Theoretical background

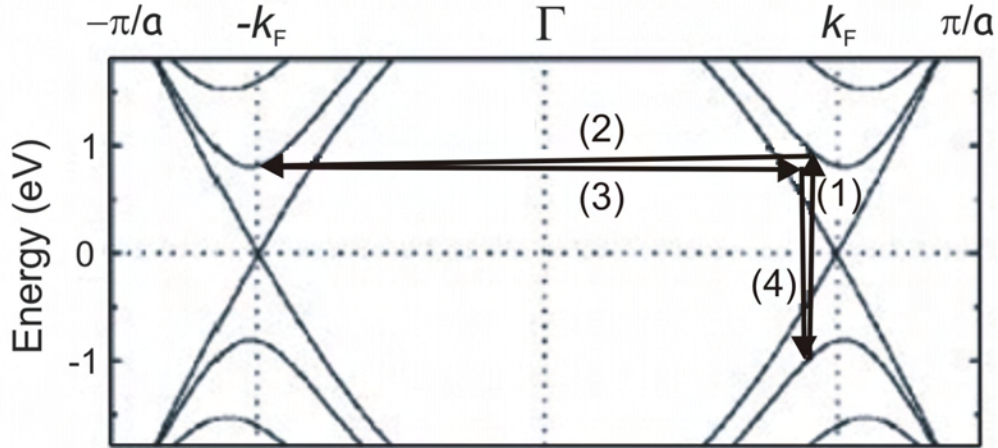


Figure 2.12.: Schematic illustration of a double-resonance process which results in a D-mode signal. The sequence of events (1 to 4) are indicated by the arrows on top of an armchair tube band structure. The optical transitions occur near the k_F wave vector at which the valence and conduction bands cross. Taken from Ref. [46].

can be either structural, impurities or its finite length (*i.e.*, the ends). In addition, the intensity of the D-mode in carbon nanotubes has a similar dependence on the defect concentration as in graphite [45]. Nevertheless, some features of the D-mode in nanotubes results from both their 1D band structure and symmetry. A schematic illustration of the electronic band structure of an armchair tube is given in Fig. 2.12.

For the $\mathfrak{N} = 3$ tubes, the K-point corresponds to $k_F = 2\pi/3a$. However, for $\mathfrak{N} = 1$ tubes, the bands crossing point refers to the Γ -point [47]. Since an armchair tube is an $\mathfrak{N} = 3$ tube, its optical transitions occur near the k_F vector, where the conduction and valence band minima and maxima are located. For z -polarized light ($\Delta m = 0$), the double-resonance condition is fulfilled if the electron is scattered across the Γ -point to a band with the same quantum number m . The defect, which scatters back the electron, can change only the electron quasi-linear momentum (k), but not m . The phonon thus has a quasi-angular momentum $m = 0$, while its wave vector is $q \approx 4\pi/3a \approx 2k_F$, which is about twice the vector Γ -K, as can be realized from the length of the long arrow in the scheme. After applying the *Umklapp* rules (since $q > 1^{\text{st}}$ -BZ boundary) one finds that the phonon wave vector changes to $2\pi/3a$ and its m to n , with a dispersion that has a Γ -point frequency that is similar to the D-mode in graphite (for details see Refs. [12, 46]). By increasing the laser

energy, the phonon wave vector moves away from the k_F wave vector, and its wave vector increases (decreases) if the optical transition is on the right (left) side of the conduction-band minimum. Both conduction bands and phonon dispersion possess a minimum at the K-point. Any increase of laser energy will result in higher phonon frequency, but lower intensity as the DOS is smaller further from the k_F .

Recently, the D-mode frequencies were measured for an isolated tube and a small bundle [48]. The observed shift with excitation energy was proof that this property is indeed not just an ensemble effect, as claimed by the selective resonance model [49].

High-energy modes (HEMs)

The frequency range of the HEMs extends between 1500 - 1600 cm^{-1} . The high-energy vibrations are the result of adjacent carbon atoms vibrating in opposite direction with respect to one another, parallel and perpendicular to the tube axis, as illustrated in Fig. 2.13. The longitudinal mode (LO) and the transverse mode (TO) are respectively called the G^+ and the G^- modes¹¹ and are almost at the same energy as in graphite for the case of semiconducting tubes. In metallic nanotubes, however, the LO mode is extremely softened (lowered in frequency) by means of a strong electron-phonon coupling mechanism [50], see section 2.4.5.

The zone-folding approach translates a single Γ -point mode of graphene into a few modes in the carbon nanotube (Fig. 2.11). This results from the confinement of the wave vector in the circumferential direction, which produces Γ -point modes for the nanotube out of non- Γ -point modes of graphene. Even though the mode frequencies are not precisely predicted by this approach, the high-energy modes of carbon nanotubes can be still related to those of graphene. They correspond directly to the E_{2g} Γ -point mode of graphene, and possess momentums that are equal to zero ($m = k = 0$).

Similar to the case of the RBM signal, the high-energy modes are a specific property of SWNTs (graphite displays only one high-energy mode). The Raman G signal of a SWNT bundle consists of a few close peaks with predominant broad peaks at ~ 1593 and ~ 1570 cm^{-1} , which are non-Lorentzian peaks and have a full width at half maximum (FWHM) of 16 and 30 cm^{-1} , respectively. However, this is not the

¹¹The high-energy modes of carbon nanotubes are also called the G band to highlight their connection to the single graphite Γ - E_{2g} G mode, located at the high symmetry Γ -point with 1582 cm^{-1} frequency.

2. Theoretical background

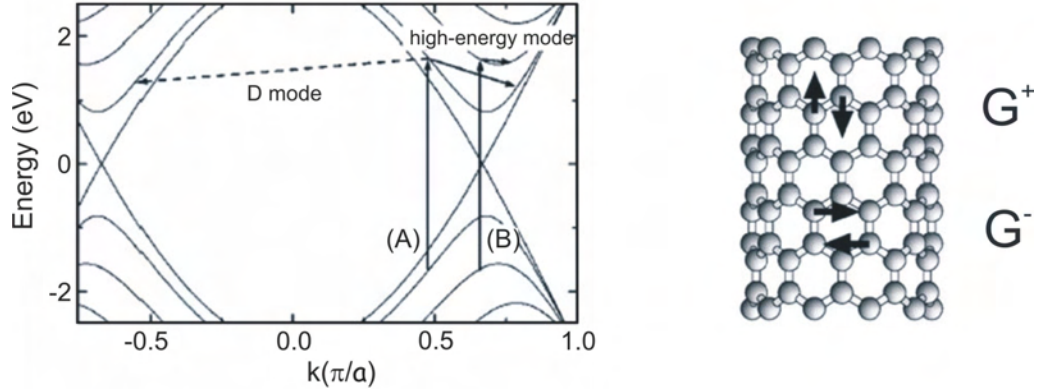


Figure 2.13.: Schematic illustration of two double-resonance processes which lead to two HEM modes. The double-resonant processes (A and B) are initiated by the same laser energy for different electron wave vectors (k). The D-mode process is also depicted for comparison. Taken from Ref. [51]. The tangential carbon vibrations along (LO, G^+) and perpendicular (TO, G^-) to the tube axis are illustrated on the right for a semiconducting tube. The reverse assignment occurs in metallic nanotubes, *i.e.*, LO, G^- and TO, G^+ .

case on the level of an individual tube. For an isolated SWNT, only two Lorentzian peaks, associated with the LO and TO vibrational modes are obtained [52]. Further, the characteristic peak structure allows the distinction between a metallic and a semiconducting tube, as long as a RBM signal is present (to assure resonance conditions, see section 4.3).

Various Raman energy-dependent studies have revealed slight frequency shifts for the HEM modes [49, 53, 54]. It was first suggested that the diameter-selective resonance concept is the cause for the observed shift, as these experiments involved different tubes of different diameters, presumably dominated by bundles. A few years later, Maultzsch *et al.* [51] have suggested an alternative explanation based on a defect-induced double-resonance scattering. By this model, the frequency of the mode changes because a different phonon of the same tube is enhanced by the double-resonant scattering process, comparable to the process resulting in a defect-induced D-mode. The only difference is that the double-resonance processes leading to the HEMs involve small- q phonons, which scatter the excited electrons across the conduction band minimum, and not across the Γ -point, as illustrated in Fig. 2.13. Processes A and B lead to the less/more intense G^- and G^+ peaks, respectively, as a larger DOS is involved in process B compared to process A (see Fig. 2.5 for the

DOS magnitude). Maultzsch *et al.* have further shown how the G^+ and G^- frequencies increase and decrease with laser energy, respectively [51]. It was explained that the G^+ peak follows the overbending of the LO branch¹² thus, its energy increases for larger- q phonons, whereas the G^- peak follows the negative slope of the TO dispersion thus, its frequency decreases for higher excitation energies.

Based on the double-resonance model, the Stokes and anti-Stokes spectra of the HEMs are expected to show different frequencies for the same laser energy, since the double-resonance conditions are slightly different. Following the single-resonance model, the difference in frequencies results because semiconducting/metallic tubes are selectively excited by the Stokes/anti-Stokes processes [55].

As a rule, only when the Raman signal reflects the properties of an individual isolated SWNT, can one draw conclusions on the tube properties. When the Raman experiment is done on bundles of SWNTs with different diameters, chiralities and orientations, the interpretation is misleading, since the Raman signal is averaged over different tubes with different properties.

2.4.5. Softening in metallic SWNTs

Dubay *et al.* [50] were the first to show theoretically that the LO mode in metallic SWNTs is significantly softer than the corresponding mode in semiconducting tubes or the peak of graphite. The theoretical calculations demonstrate a general tendency of a decreased phonon frequency for smaller diameter tubes. However, for different metallic tubes, the LO mode (the G^- peak) also drops below the TO (responsible for the G^+ peak) phonon frequency with a much stronger diameter dependence.

The softening in metallic SWNTs originates from a developed band-gap at the π bands crossing point, caused by the LO axial vibration. To realize this gap opening, Dubay *et al.* [50] have illustrated the band structure of graphene at the K-point in a 3D representation. As shown in Fig. 2.14, the two intersecting bands form two cones around the K-point. The band structure of an armchair tube at E_F is indicated by the thick lines. The LO mode opens a gap in the armchair tube, since the tip of the cones has moved perpendicular to the allowed line (here shown as ΓK line). However, the TO mode leads only to a shift of the k_F to a different k

¹²Overbending occurs when the maximum phonon frequency is higher than the frequency at the Γ -point.

2. Theoretical background

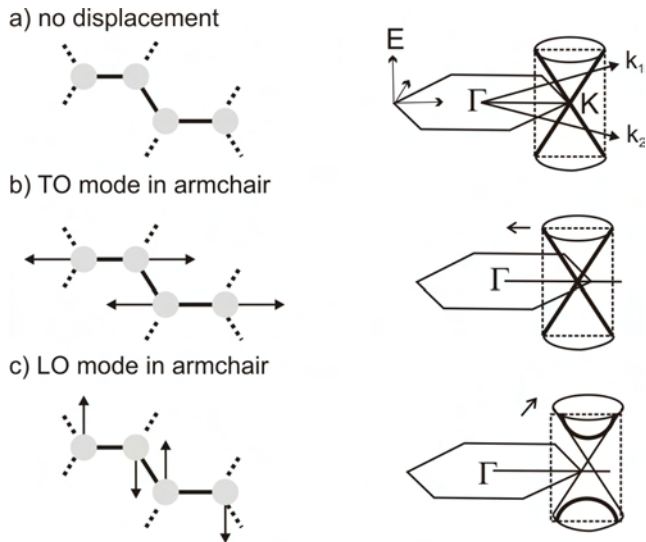


Figure 2.14.: Schematic drawing of the electronic band structure at the graphene K-point, illustrating the band structure of an armchair tube (crossing thick lines). In (a), no displacement is present. The changes in the band structure of the tube is demonstrated in (b) and (c) for the TO and LO displacements. Modified from Ref. [50].

point. The mechanism is similar for a zig-zag tube, except that the allowed lines are perpendicular to those for armchair, and thus, the LO mode is again the one to cause the gap-opening.

The formation of such a gap in metallic tubes lowers the band-structure energy of the system, as filled states are moved to lower energy. Further, as the relation $\text{DOS} \propto 1/d$ holds in the vicinity of the Fermi level (Fig. 2.5), a softer axial mode results for smaller diameter tubes. The softening can amount up to 100 cm^{-1} , compared to the TO mode of semiconducting tubes at $\approx 1590 \text{ cm}^{-1}$, and decreases with increasing tube diameter.

In summary, the totally symmetric axial LO mode of symmetry A_1 is the displacement which moves the cones perpendicular to the lines allowed by the periodicity imposed by the zone-folding procedure. This mode creates the largest gap, irrespective of chirality, where the electron-phonon coupling mechanism demonstrated above opens a gap when a nanotube swings back and forth in a manner compatible to the A_1 mode. The oscillating band gap lowers the frequency of the LO mode in a manner which resembles a "dynamic" Peierls distortion [50]. From this model it is clear that armchair tubes have a small non-vanishing gap at zero-temperature, as the LO mode freezes. This strong electron-phonon coupling in metallic SWNTs was recently found by various experimental studies to be of importance not only in low-temperature experiments but also in high-electric-field applications at room-temperature [9–11].

Kempa [56] and Jiang *et al.* [57] have suggested a phonon-plasmon interaction mechanism that causes the downshift and line-shape of metallic bulk samples spectra. They claimed that a non-zero phonon wave vector is needed for such coupling, *i.e.*, there must be defects present in the tubes. However, the required wave vector decreases with bundle thickness, whereas the Raman intensity of the low-energy side of the metallic peak, also called the Breit-Wigner-Fano (BWF) line, increases. They further claimed that for a single metallic tube, the strength of the BWF line increases with decreasing tube diameter. In contrast, the current work addresses the topic by demonstrating that **no BWF line is observed on the level of an individual metallic SWNT**, *i.e.*, no hybrid excitations of low-energy plasmon modes with phonon modes (plasmon-phonon modes) occurs in an individual metallic tube [52]. These experimental findings are systematically given in section 4.3. Further, the Raman spectrum of a small metallic bundle can be misleading at certain excitation-energies by revealing a semiconducting-like line-shape [48]. If however it shows a metallic line-shape, it is definitely metallic in character. The conclusion originates from the softening of the LO axial mode, which occurs only in metallic tubes and gives rise to the peak at $\approx 1540 \text{ cm}^{-1}$. The broadening originates from electron-phonon coupling relaxation processes on the level of an individual tube (section 4.5), however, when bundles are involved, the broadening originates from a coupling to continuum states, namely, phonon-plasmon coupling mechanism, where an asymmetric BWF line-shape appears [56, 57].

Finally, Lazzeri *et al.* [58] have recently shown how the electron-phonon coupling mechanism is the major source of the broadening of the G^- peak in metallic tubes. An elaborate discussion about the influence of the electron-phonon coupling mechanism on the Raman line-shape of individual metallic SWNTs, is given in section 4.5.

2.5. Dielectrophoresis

The application of electric fields, especially non-homogeneous fields, is a powerful tool for manipulating small objects with slightly differing electrical properties. Krupke *et al.* [59] were the first to exploit the dielectrophoretic separation technique in the case of carbon nanotubes. They have demonstrated how separation of metallic from semiconducting SWNTs in individual tube suspensions can be achieved based on the different polarizabilities of metallic and semiconducting SWNTs. The fact that the dielectric constants of semiconducting and metallic tubes are smaller and

2. Theoretical background

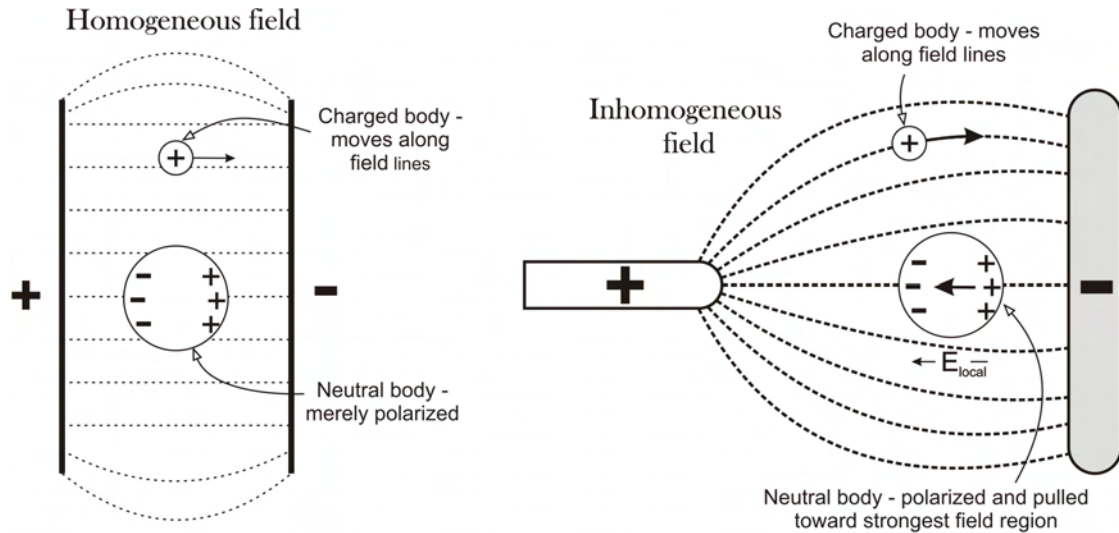


Figure 2.15.: A schematic illustration of the neutral and positively charged bodies response to both homogeneous and inhomogeneous electric fields. Adapted from Ref. [60].

larger, respectively, compared to that of water provided the possibility to separate the two tube types under the application of a strong inhomogeneous electric field. Under these conditions, an induced dipole moment interacts with the alternating inhomogeneous external field, leading to a movement of the metallic SWNTs in the direction of the high-field region, while the semiconducting SWNTs movement is toward the low-field region.

In the present work, the SWNTs were deposited via *low-frequency* dielectrophoresis, which allows the deposition of both individual metallic and semiconducting SWNTs from suspension. For details please refer to section 3.2.

2.5.1. Basics of dielectrophoresis

Translational motion of a neutral body can be caused by its response to an *inhomogeneous* electric field. When the body is polarized its motion is classified as *Dielectrophoresis*. The term is used *only* if an inhomogeneous field is applied and translates as motion of dielectric materials, since in Greek *phoresis* means motion. *Electrophoresis* is, in contrast, the translational motion of a charged body in a homogeneous or an inhomogeneous electric field, as both produce a net force on the charged body.

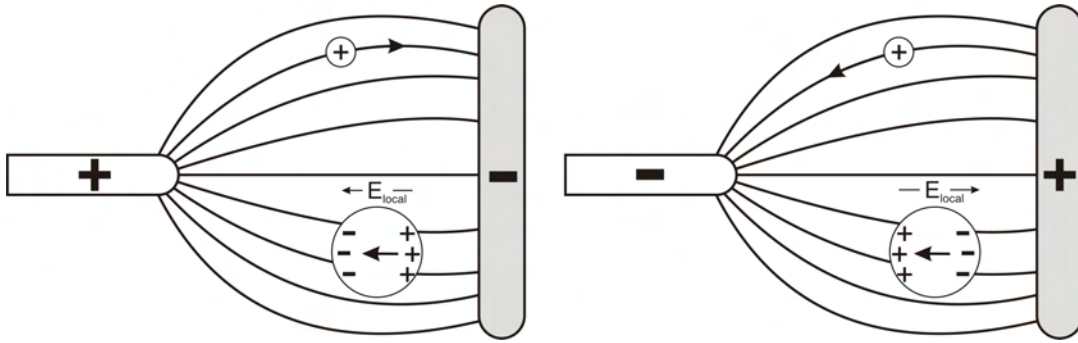


Figure 2.16.: The behaviors of neutral and positively charged bodies in both electrode polarities of an alternating inhomogeneous electric field. Adapted from Ref. [60].

Figure 2.15 demonstrates the difference in motion for neutral and charged bodies in homogeneous and inhomogeneous electric fields. The positively charged body is pulled toward the negative electrode under either field influence. The neutral body response though is to become polarized with two oppositely induced charged-regions. In a homogeneous field only polarization occurs as no net translational force results to cause any motion. Yet, under the influence of an inhomogeneous field, the neutral body experiences a net translational force, also called a *dielectrophoretic force*, which pulls it toward the strong field region. The net dielectrophoretic force results as the two field regions operate non-equally on the two equal but oppositely charged-regions of the neutral body. The total response of this so called *paraelectric* motion includes the initial polarization of the body in the field followed by the action of the field-inhomogeneity on the induced dipole. The net dielectrophoretic force results as one of the two charge distributions of the neutral body lies in a stronger field¹³. The paraelectric motion of the neutral body will be in the same direction under a *dc* field or an alternating potential, as its polarization can reverse in accordance to the electrode polarity, *i.e.*, up to a certain frequency in which the induced dipole can no longer follow the change in electrodes polarity. In Fig. 2.16 the contrasted behaviors of positively charged and neutral bodies in both electrode polarities of an inhomogeneous field are illustrated. The neutral body in both polarity schemes moves toward strongest field region as a net force toward the more intense field region results. The local field direction is reversed, however the polarized body is still pulled toward the region of highest field intensity. In contrast, the charged body

¹³For an elongated body like a SWNT, an additional torque arises which aligns the tube with the field direction.

2. Theoretical background

moves toward the negative electrode in both polarities. In a homogeneous or an inhomogeneous ac field though it will only vibrate, as the net effect over a full cycle is zero, *i. e.*, the charged body moves equally in both directions for each half-cycle.

The net dielectrophoretic force \vec{F} acting on a small polarized neutral body in a static electric field is given at equilibrium by:

$$\vec{F} = (p_x \partial/\partial x + p_y \partial/\partial y + p_z \partial/\partial z) \vec{E}_{\text{ext}} = (\vec{p} \cdot \nabla) \vec{E}_{\text{ext}} \quad (2.28)$$

where \vec{p} is the dipole moment vector oriented in an arbitrary direction and \vec{E}_{ext} is the external electric field. From Eq. 2.28 it is clear that the force is non-zero only for an inhomogeneous electric field where dielectrophoretic motion can occur.

A linear dependence of a dipole moment on external field is defined for an isotropic dielectric body by:

$$\vec{p} = \vec{\alpha} v \vec{E}_{\text{ext}} \quad (2.29)$$

where $\vec{\alpha}$ is the polarizability¹⁴ and v is the volume of the homogeneous body.

Following the vector transformation

$$(\mathbf{A} \cdot \nabla) \mathbf{B} = \nabla(\mathbf{A} \cdot \mathbf{B}) - (\mathbf{B} \cdot \nabla) \mathbf{A} - \mathbf{A} \times (\nabla \times \mathbf{B}) - \mathbf{B} \times (\nabla \times \mathbf{A}) \quad (2.30)$$

the dielectrophoretic force can be expressed as:

$$\vec{F} = (\vec{p} \cdot \nabla) \vec{E}_{\text{ext}} = \nabla(\vec{p} \cdot \vec{E}_{\text{ext}}) - (\vec{E}_{\text{ext}} \cdot \nabla) \vec{p} \quad (2.31)$$

since $\nabla \times \vec{E}_{\text{ext}} = 0$ (the electric field is irrotational) and $\vec{p} = \vec{\alpha} \vec{E}_{\text{ext}} v$ (homogeneous dielectric).

Then the dielectrophoretic force¹⁵ is:

$$\begin{aligned} \vec{F} &= \vec{\alpha} (\vec{E}_{\text{ext}} \cdot \nabla) \vec{E}_{\text{ext}} v = \vec{\alpha} \left(\nabla |\vec{E}_{\text{ext}}|^2 - (\vec{E}_{\text{ext}} \cdot \nabla) \vec{E}_{\text{ext}} \right) v = \vec{\alpha} v |\vec{E}_{\text{ext}}| \nabla |\vec{E}_{\text{ext}}| = \\ &= (\text{polarizability}) \cdot (\text{volume}) \cdot (\text{local field}) \cdot (\text{field gradient}) \end{aligned} \quad (2.32)$$

or

$$\vec{F} = \frac{1}{2} \vec{\alpha} v \nabla |\vec{E}_{\text{ext}}|^2 \quad (2.33)$$

¹⁴The polarizability $\vec{\alpha}$ is a tensor for an anisotropic polarized body.

¹⁵In the simple case of isotropic linear dielectrics, the equivalent forms for the field factor are:

$$(\vec{E}_{\text{ext}} \cdot \nabla) \vec{E}_{\text{ext}} = |\vec{E}_{\text{ext}}| \nabla |\vec{E}_{\text{ext}}| = \frac{1}{2} \nabla |\vec{E}_{\text{ext}}|^2$$

The dielectrophoretic force acting upon a body is proportional to the first power of both its volume and polarizability, but, depends on the *square* of the electric field intensity, emphasizing that it can additionally occur in an alternating field.

2.5.2. The dielectrophoretic force on a small sphere

In order to find the dielectrophoretic force acting on a spherical object in an inhomogeneous electric field, both sphere and medium are assumed ideal¹⁶. If a sphere containing a fluid of relative dielectric constant ε_{r_2} is inserted into an infinite fluid of relative dielectric constant ε_{r_1} , the external electric field \vec{E}_{ext} in the fluid is distorted by the sphere. A field \vec{E}_i interior to the sphere is created and relates to the external field as follows:

$$\vec{E}_i = \vec{E}_{\text{ext}} \frac{3\varepsilon_{r_2}}{\varepsilon_{r_1} + 2\varepsilon_{r_2}} \quad (2.34)$$

As the dielectrophoretic force is proportional to the volume of the body it acts upon (Eq. 2.33), for a spherical object it is proportional to $4\pi a^3/3$, where a is the radius of the sphere.

The induced moment $\vec{\mu}_{\text{ind}}$ of a polarizable sphere is given by:

$$\vec{\mu}_{\text{ind}} = 4\pi a^3 \varepsilon_1 \left(\frac{\varepsilon_2 - \varepsilon_1}{\varepsilon_2 + 2\varepsilon_1} \right) \vec{E}_{\text{ext}} = (\alpha v) \vec{E}_{\text{ext}} \quad (2.35)$$

where ε_1 and ε_2 are the permittivities of the infinite medium and small sphere, respectively, and v and \vec{E}_{ext} are the sphere volume and external electric field. The product of the polarizability and volume can be rearranged:

$$\alpha v = 4\pi a^3 \varepsilon_1 \left(\frac{\varepsilon_2 - \varepsilon_1}{\varepsilon_2 + 2\varepsilon_1} \right) = 4\pi a^3 \varepsilon_{r_1} \varepsilon_0 \left(\frac{\varepsilon_{r_2} - \varepsilon_{r_1}}{\varepsilon_{r_2} + 2\varepsilon_{r_1}} \right) \quad (2.36)$$

so the dielectrophoretic force expression (note the structure of Eq. 2.33) is then:

$$\vec{F} = \left(\frac{1}{2} \right) \underbrace{\left(\frac{4\pi a^3}{3} \right)}_{\text{volume}} \underbrace{(\varepsilon_{r_1} \varepsilon_0) \left(\frac{3(\varepsilon_{r_2} - \varepsilon_{r_1})}{\varepsilon_{r_2} + 2\varepsilon_{r_1}} \right)}_{\text{polarizability}} \nabla |\vec{E}_{\text{ext}}|^2 \quad (2.37)$$

or

$$\vec{F} = 2\pi a^3 \varepsilon_{r_1} \varepsilon_0 \left(\frac{\varepsilon_{r_2} - \varepsilon_{r_1}}{\varepsilon_{r_2} + 2\varepsilon_{r_1}} \right) \nabla |\vec{E}_{\text{ext}}|^2 \quad (2.38)$$

¹⁶An ideal dielectric is defined to have a zero conductivity, whereas a real dielectric has both a dielectric constant and a conductivity.

2. Theoretical background

Table 2.1.: The variation in the relative polarizability factor $\varepsilon_{r_1} \left(\frac{\varepsilon_{r_2} - \varepsilon_{r_1}}{\varepsilon_{r_2} + 2\varepsilon_{r_1}} \right)$ of different systems. Adapted from Ref. [60].

ε_{r_2}	ε_{r_1}	$\varepsilon_{r_1} \left(\frac{\varepsilon_{r_2} - \varepsilon_{r_1}}{\varepsilon_{r_2} + 2\varepsilon_{r_1}} \right)$	Example
80	1	0.963	Water droplet in air
∞	1	1.00	Metal ball in air
12	2	1.25	Silicon ball in hydrocarbon liquid
1	2	-0.20	Air bubble in hydrocarbon liquid
2	80	-38.50	Fat or oil drop in water
4000	80	75.40	BaTiO ₃ crystal in water
∞	80	80	Metal ball in water

The term $\varepsilon_{r_2} - \varepsilon_{r_1}$ in the numerator refers to the replacement of the dielectric medium with that of the sphere. The dielectric constant (permittivity) is defined $\varepsilon_{1,2} = \varepsilon_{r_{1,2}} \cdot \varepsilon_0$ with the permittivity of vacuum $\varepsilon_0 = 8.854 \times 10^{-12}$ C/Vm times the relative dielectric constant ε_r . Based on Eq. 2.37, a general expression of the dielectrophoretic force upon a small sphere¹⁷ reads:

$$\vec{F}_{\text{sphere}} = \frac{3}{2}(\text{volume})\varepsilon_1 \left(\frac{\varepsilon_2 - \varepsilon_1}{\varepsilon_2 + 2\varepsilon_1} \right) \nabla |\vec{E}_{\text{ext}}|^2 = 2\pi a^3 \varepsilon_1 \left(\frac{\varepsilon_2 - \varepsilon_1}{\varepsilon_2 + 2\varepsilon_1} \right) \nabla |\vec{E}_{\text{ext}}|^2 \quad (2.39)$$

From Eq. 2.39, the dielectrophoretic force should be zero if the dielectric constants of the sphere and of the surrounding medium are equal. On the other hand, the force can not increase without limit as the polarity of the sphere increases. Even if the dielectric constant of the sphere is constantly increasing, the increase in the force is limited and is determined by the size of the dielectric constant of the surrounding medium. Table 2.1 illustrates the variation in the relative polarizability factor contained within \vec{F}_{sphere} for different relative dielectric constants of sphere (ε_{r_2}) and surrounding medium (ε_{r_1}).

The field lines within a sphere (Eq. 2.34) are parallel (non-parallel) to the external field when both homogeneous sphere and medium are in an external homogeneous (inhomogeneous) field. However, if $\varepsilon_{r_2} > \varepsilon_{r_1}$, *i.e.*, the sphere is more polarizable than the medium, the field lines external to the sphere also focus (concentrate) at its surface. The resultant field inhomogeneity causes adjacent spheres to attract each other, which result in a bunching effect. Often the effect further causes '*pearl*

¹⁷The field in the sphere is assumed to maintain the sphere dipole size, *i.e.*, its polarization degree.

chains' formation, where for a large enough bunching effect, the particles can even bridge a gap between electrodes [60].

2.5.3. The formation of an inhomogeneous electric field

Inhomogeneous fields are required to achieve a dielectrophoretic response where the expression for the dielectrophoretic force on a sphere is defined in Eq. 2.39. The equation states that alternating fields can be used, however intense fields are needed if stronger dielectrophoretic forces are desired. The term $\nabla|\vec{E}|$ in Eq. 2.32 further emphasizes the necessity of a field gradient, *i.e.*, the variation of the field intensity with distance.

Various fields and electrode geometries are available for the different applications of dielectrophoresis. Some are listed in Ref. [60]. In general, one needs to consider whether extreme variations in the dielectrophoretic force throughout an extended region are desired, or whether, the force strength should be equal upon specific particles wherever they might be in the supporting medium. It is normally assumed that for any dielectrophoretic application the electrodes determine the field 'seen' by the particles at each specific region within the layout pattern.

2.5.4. Dielectrophoresis in real dielectric materials

Already in the 60's [61, 62] it was observed that the dielectrophoretic response of either living cells or other particles, shows a strong dependence on two factors: the *frequency* of the external field and the *conductivity* of the suspending medium¹⁸. Consequently, the expression for the dielectrophoretic force, given in Eq. 2.39, must include the frequency and conductivity dependence.

The simple dielectric constants of the particle and of the medium are replaced by the complex dielectric constants:

$$\varepsilon^* = \varepsilon - i\frac{\sigma}{\omega} \quad \text{and} \quad \hat{\varepsilon}^* = \varepsilon + i\frac{\sigma}{\omega} \quad (2.40)$$

where ε and $i\sigma/\omega$ are the real and imaginary parts of the complex permittivity or its complex conjugate, and σ is the conductivity.

¹⁸For carbon nanotubes, both particle and medium conductivities are important at low frequencies ($\omega \lesssim 1$ MHz) as shown in Eq. 2.44 below.

2. Theoretical background

The expression of the dielectrophoretic force in Eq. 2.39 is therefore corrected for a real spherical particle:

$$\vec{F}_{\text{sphere}} = 2\pi a^3 \Re \left(\frac{\varepsilon_1^* (\varepsilon_2^* - \varepsilon_1^*)}{\varepsilon_2^* + 2\varepsilon_1^*} \right) \nabla |\vec{E}_{\text{ext}}|^2 = 2\pi a^3 \varepsilon_1 \Re \left(\frac{\varepsilon_2^* - \varepsilon_1^*}{\varepsilon_2^* + 2\varepsilon_1^*} \right) \nabla |\vec{E}_{\text{ext}}|^2 \quad (2.41)$$

From Eq. 2.41 one realizes that the dielectrophoretic force exerted upon the sphere is due to the difference between the sphere's and liquid medium's polarizabilities $\vec{F} \propto \Re(|\varepsilon_2^*| - |\varepsilon_1^*|)$ *i.e.*, it is a net force. The dielectrophoresis technique directly uses the differences in the polarizability or conductivity to obtain its selectivity of collection.

2.5.5. Dielectrophoretic force on SWNTs

For the case of single-walled carbon nanotubes, the general expression for the dielectrophoretic force derived for a long tube ($L \gg d$) aligned parallel to an inhomogeneous *ac* field \vec{E} of angular frequency ω is given by:

$$\vec{F}_{\text{SWNT}} = \frac{1}{2} \left(\frac{\pi d^2 L}{4} \right) \varepsilon_l \Re \left(\frac{\varepsilon_t^* - \varepsilon_l^*}{\varepsilon_l^*} \right) \nabla |\vec{E}|^2 = \frac{\pi d^2 L}{8} \varepsilon_l \Re \left(\frac{\varepsilon_t^* - \varepsilon_l^*}{\varepsilon_l^*} \right) \nabla |\vec{E}|^2 \quad (2.42)$$

where the complex dielectric constants of the tube and the surrounding liquid are the ε_t^* and ε_l^* , respectively [63]. L is the tube length and is assumed much bigger than the tube diameter d . In principle, the expression also contains a depolarization factor which accounts for the particle shape [63], however, its value is negligible (on the order of 10^{-5}) for the tubes studied here. By simple algebra, the dependence of the dielectrophoretic force \vec{F}_{DEP} on the dielectric constant and conductivity can be derived for the low- and high-frequency regimes. The sign of the dielectrophoretic force changes for the case of metallic and semiconducting SWNTs at the different regimes, as illustrated in Fig. 2.17.

The derivation starts from the real part of the complex permittivities as given in Eq. 2.42 and results in the following expressions for the high- and the low-frequency regimes:

$$\vec{F}_{\text{DEP}} (\omega \rightarrow \infty) \propto \left(\frac{\varepsilon_t - \varepsilon_l}{\varepsilon_l} \right) \quad (2.43)$$

$$\vec{F}_{\text{DEP}} (\omega \rightarrow 0) \propto \left(\frac{\sigma_t - \sigma_l}{\sigma_l} \right) \quad (2.44)$$

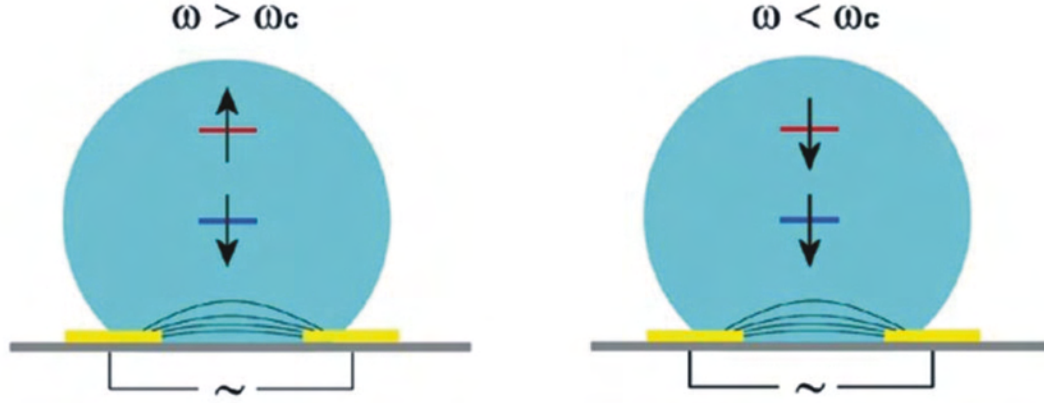


Figure 2.17.: Schematic illustration for the setup used in tube separation experiment. A side view of a drop of tube suspension is demonstrated on top of the electrode array. Field lines during deposition are demonstrated. Metallic and semiconducting SWNTs (blue/red) are attracted or repulsed due to positive (\downarrow) or negative (\uparrow) dielectrophoresis force, depending if the field angular frequency ω is bigger or smaller than the crossover frequency ω_c . Taken from Ref. [63].

where $\varepsilon_{t,l}$ and $\sigma_{t,l}$ are the tube/liquid-medium dielectric constants and conductivities, respectively.

In this work, SWNTs were deposited from a surfactant-stabilized suspension on a pre-patterned electrode layout via low-frequency dielectrophoresis (DEP). In this frequency regime ($\omega \rightarrow 0$) both individual metallic and semiconducting SWNTs experience a positive DEP (the \vec{F}_{DEP} in Eq. 2.44 is positive) and thus both are deposited, as discussed below. Metallic SWNTs have both dielectric constant ($\sim 1000\varepsilon_0$) and conductivity values which are much bigger than those of water [64]. The conductivities of water at 0.01%, 0.1% and 1% SDBS concentrations are 4 mS/m, 29 mS/m and 230 mS/m, respectively as was measured by Krupke *et al.* [63]. The water dielectric constant ε_l varies between $\varepsilon_l = 75\varepsilon_0$ and $85\varepsilon_0$, depending on surfactant concentration and frequency used. According to Eqs. 2.43 and 2.44 as well as shown in Fig. 2.17, metallic SWNTs undergo a positive DEP process and thus a positive dielectrophoretic force ($\vec{F}_{\text{DEP}} > 0$) at any frequency and water conductivity. In contrast, the dielectric constant of semiconducting SWNTs ranges between $2\varepsilon_0$ and $5\varepsilon_0$, depending on the tube diameter¹⁹ [64]. The semiconducting SWNTs with a zero

¹⁹The value of the dielectric constant of the semiconducting SWNTs was calculated by the expression $\varepsilon_t^{\text{s.c.}} = 1 + \left(\frac{\hbar\omega_p}{5.4E_g}\right)^2$ with the plasma frequency ω_p , the energy gap $E_g \propto 1/d$ and $\hbar\omega_p \cong 5$ eV [64].

2. Theoretical background

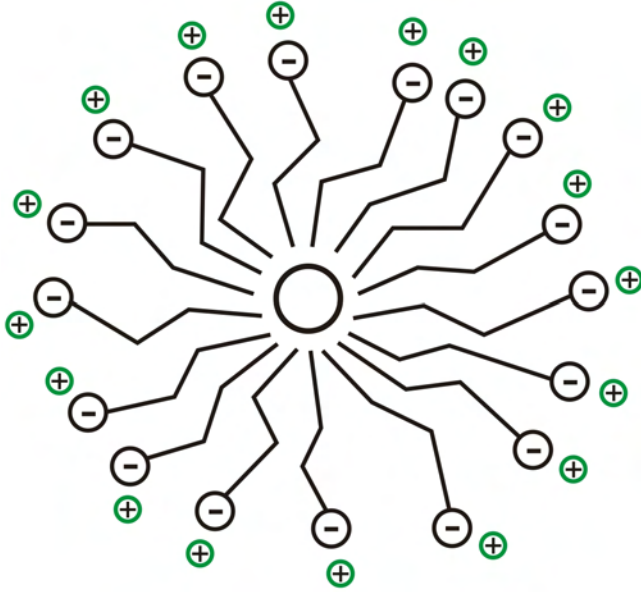


Figure 2.18.: Schematic illustration of an individual SWNT in a cylindrical SDBS micelle. The hydrophobic tail of the negatively charged benzene sulfonate headgroups are adsorbed at the tube surface. The resultant negatively charged tube is screened by the Na^+ counterions around this structure.

intrinsic conductivity should according to Eqs. 2.43 and 2.44 undergo a negative DEP process with a $\vec{F}_{\text{DEP}} < 0$ at any frequency and water conductivity, *i.e.*, $\varepsilon_t^{\text{s.c.}} < \varepsilon_l$ and $\sigma_t^{\text{s.c.}} < \sigma_l$ in both high- and low-frequency regimes, respectively. However, at low frequencies, semiconducting SWNTs can be deposited as a crossover frequency ω_c from negative DEP at $\omega > \omega_c$ to positive DEP at $\omega < \omega_c$ occurs. Krupke *et al.* [63] have explained this effect by assigning a finite conductivity to the semiconducting SWNTs. The sizeable conductivity of the semiconducting tubes can be visualized as follows. The insertion of a surfactant into water causes some dissociation between the negatively charged headgroup ions and their counterions. The total solution charge is however neutral. After inserting the SWNTs to form the surfactant-stabilized SWNTs suspension, the hydrophobic negative headgroups adsorb on the tubes surface while the counterions are arranged next to the headgroups as depicted in Fig. 2.18 (see appendix B for the SDBS structure). The structure illustrates immobilized negative headgroups at the tube surface, and mobile Na^+ ions, which diffuse around, yet with most near the micellated tube. This dissociation occurs as it is energetically favorable.

Placing the system in a static electric field will cause an electrophoretic response with the Na^+ ions moving in one direction. The magnitude of this movement is controlled by the electrostatic interaction with the negative headgroups. In contrast, a back and forth movement of the Na^+ ions will occur in an alternating field, where its magnitude depends on the mobility of the ions. The whole structure of the tube-

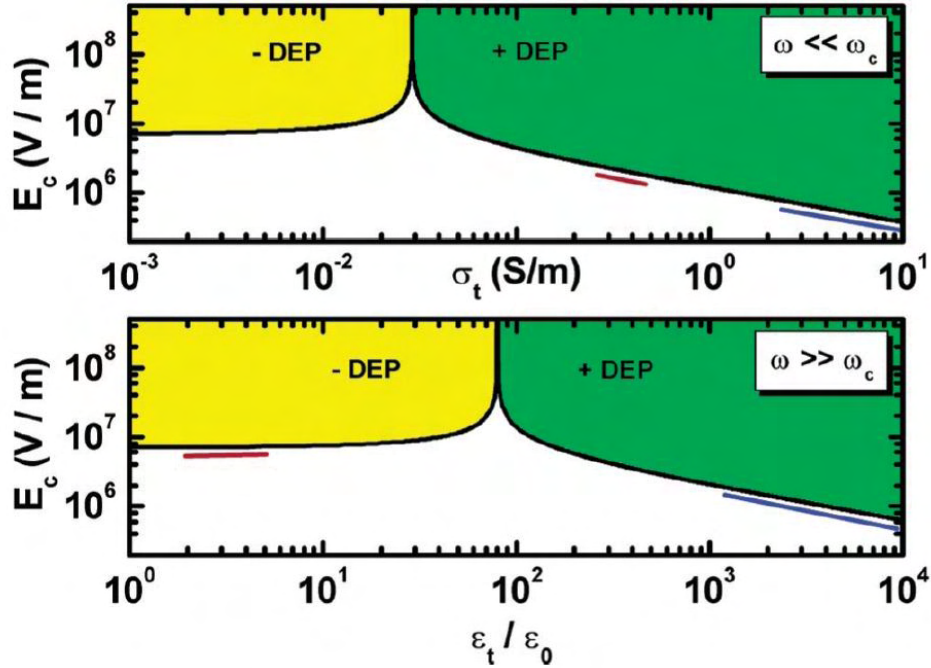


Figure 2.19.: Calculated minimum \vec{E}_{\min} needed for the DEP response. Upper/lower panels show the dependence of \vec{E}_{\min} on the conductivity (σ_t)/dielectric constant (ϵ_t) of the micellated tube. The E_c values which correspond to the given experiment are marked with blue/red for the metallic/semiconducting SWNTs. Higher values of E_c , are marked green/yellow for positive/negative DEP responses. Taken from Ref. [63].

surfactant- Na^+ thus becomes polarizable. Note that even though the tube seems polarized, its polarizability was provided by the movement of the weakly bounded Na^+ ions. It follows that experimentally, the semiconducting SWNTs act as having some finite conductivity at low frequencies²⁰. Nevertheless, the contribution of the conductivity gets smaller with increasing frequency, as implied by the expression of the complex dielectric constant, $\epsilon^* = \epsilon - i\sigma/\omega$. It was therefore concluded that the conductivity originates from a surface effect as similarly obtained in earlier experiments on latex beads [67] and tobacco mosaic virus (TMV) [68] where an electric double-layer at the solid-liquid interface was reported to modify the dielectric properties of the non-conducting particles.

Krupke *et al.* [63] further reported that their model agrees well with the DEP experiments on TMV in a potassium phosphate buffer, which yielded a surface-induced

²⁰Any conductivity due to doping was excluded, based on fluorescence data of similar material [65, 66].

2. Theoretical background

conductivity value of $\sigma = 0.085$ S/m. They additionally calculated the minimum field strength \vec{E}_{\min} required to manipulate the SWNTs via DEP. In their derivation they have accounted for only a competing force due to Brownian motion and neglected any other electrohydrodynamical forces. The minimum field strength \vec{E}_{\min} was estimated by equating the DEP potential energy to the thermal energy, yielding:

$$\vec{E}_{\min} \quad (\omega \gg \omega_c) \simeq \sqrt{\frac{k_B T}{\frac{\pi d^2 l}{8} \varepsilon_l \Re e \left(\frac{|\varepsilon_t - \varepsilon_l|}{\varepsilon_l} \right)}} \quad (2.45)$$

$$\vec{E}_{\min} \quad (\omega \ll \omega_c) \simeq \sqrt{\frac{k_B T}{\frac{\pi d^2 l}{8} \varepsilon_l \Re e \left(\frac{|\sigma_t - \sigma_l|}{\sigma_l} \right)}} \quad (2.46)$$

For a micellated tube with $d = 5$ nm and $l = 500$ nm in a 0.1 % SDBS suspension, the minimum field required is plotted in Fig. 2.19. The \vec{E}_{\min} is on the order of 10^6 V/m, in agreement with their and the present work's experimental observations. Further, the \vec{E}_{\min} was found smaller for the better conducting metallic tubes. Thus, positive dielectrophoretic forces are in general stronger for metallic than for semiconducting SWNTs [63].

3. Experimental

The SWNTs investigated in this work were produced by the pulsed laser vaporization technique at the University of Karlsruhe and were provided by Frank Henrich. The SWNTs have a near-Gaussian distribution of diameters, ranging between $\sim 1.0 - 1.5$ nm for both metallic and semiconducting SWNTs. The distribution was characterized based on our Raman measurements (Tables 4.1 and 4.2) and agrees well with fluorescence measurements on the same kind of material [66]. The synthesized SWNTs were deposited by the low-frequency dielectrophoresis method on a pre-patterned electrode array, where they were next electrically characterized by two-point resistance measurements. Further characterization of the individual SWNTs were carried out via confocal Raman spectroscopy, to study their vibrational properties.

3.1. SWNTs synthesis via the pulsed laser vaporization (PLV) technique

The SWNTs used and investigated here were produced by the PLV technique [69]. This technique is based on the laser ablation/sublimation of carbon under an inert atmosphere. For the specific tubes used here, a graphite target containing 1 atom % Ni and Co metal catalysts is vaporized by pulsed laser irradiation (1064 nm, 0.5 J/pulse, ~ 8 ns, 30 Hz) under 0.5 bar Ar atmosphere. The target is mounted on a ceramic rod so it can be placed exactly in front of the side arm of a T-shaped quartz tube, to be later irradiated by the laser. The setup in a temperature controlled hinge oven is shown on the left panel of Fig. 3.1, where its configuration is set to irradiate the side surface of the rotating and axially translating C:Ni:Co target. After the sealed tube is evacuated, the oven temperature is increased to 1150°C. The tube is then filled with 0.5 bar Ar gas (flowing at ~ 80 sccm). A typical vaporization rate is ~ 0.15 g/h in pure Ar. SWNT material is swept by the flowing gas from the

3. Experimental

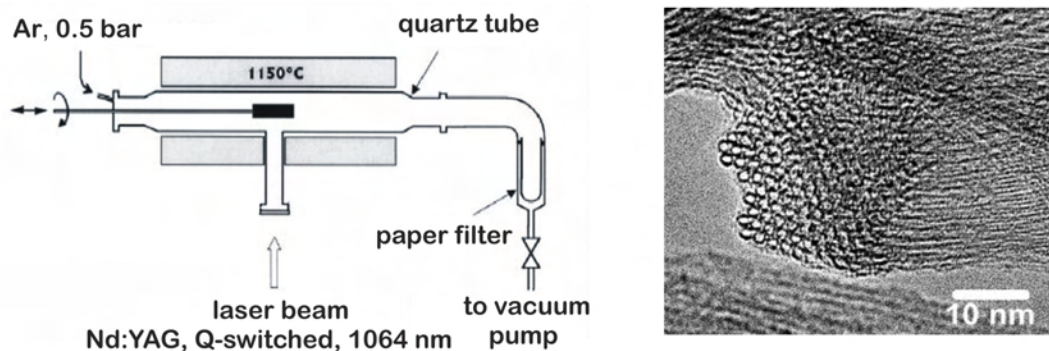


Figure 3.1.: (Left) A pulsed laser vaporization setup for the preparation of SWNTs. This setup is unique in its configuration with the carbon target being side-irradiated while rotating and axially translating. (Right) A high-resolution transmission electron microscopy (TEM) picture of a cross section of a bundle of single-walled nanotubes obtained by the pulsed laser vaporization technique with Ni/Co metal catalysts. The wall-to-wall distance between two tubes is in the same range as the interlayer distance in graphite (3.41 Å). Taken from Ref. [69].

high-temperature zone and collected on a filter or in the cold downstream region along the tubing to the filter. Depending on the metal catalyst used, the yield of nanotubes can vary drastically. A high yield of SWNTs bundles is obtained with Ni/Co or Ni/Y catalysts ($\sim 20\text{-}50\%$ by volume, ~ 20 nm diameter) [69] as can be seen on the right side of Fig. 3.1, which shows a transmission electron microscopy image of such a bundle.

3.2. Deposition of SWNTs via *low-frequency dielectrophoresis*

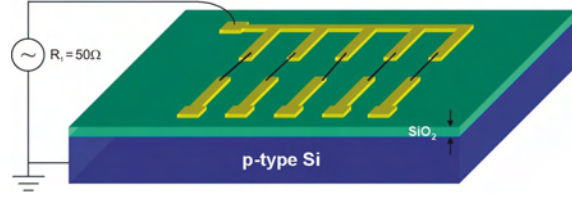
Of the as-grown SWNTs, 0.02 mg/ml were suspended in D_2O with 0.5 w-% sodium dodecylbenzene sulfonate (NaDDBS or simply SDBS)¹. The suspension was centrifuged at 154000 g for 2 hours with the upper 50% of the supernatant carefully decanted. The decant was next diluted with D_2O by a factor of one hundred to a concentration of a few ng/ml of individual SWNTs.

The layout and the wiring plan used for the deposition is schematically demonstrated in Fig. 3.2. The layout shows a set of electrode-pairs with 1 μm (or 0.5 μm) gap

¹Various surfactants are available to form stabilized-SWNTs suspensions. See appendix B for those used in the present work.

3.2. Deposition of SWNTs via low-frequency dielectrophoresis

Figure 3.2.: A drawing of the chip layout used for the SWNTs deposition and its wiring plan. The illustrated yellow electrodes have a finite gap (0.5 or 1 μm) and are placed on a p-type Si substrate (blue), which possesses a finite thickness of thermally oxidized SiO_2 (green). The black lines bridging the electrodes illustrate SWNTs. A load resistor of $R_1 = 50 \Omega$ is shown for the frequency generator. Taken from Ref. [70].



on a thermally oxidized p-type silicon substrate² (oxide layer is 800 nm thick unless otherwise specified). Many electrode pairs are prepared via standard electron beam lithography³ followed by a standard lift-off procedure. Approximately 40 nm thick Pd or Au was used as the top electrode material with $\sim 2\text{-}3$ nm Ti as an adhesion layer. A sputter coating technique was used to deposit the metal electrodes. The layout was wired to a function generator with a maximum frequency $f = 30$ MHz and a load resistor of $R_1 = 50 \Omega$. As depicted in Fig. 3.2 the unwired electrodes are floating and the substrate is grounded. Low-frequency dielectrophoresis was employed for the tube deposition and the frequency was set to 300 kHz with a $V_{\text{p-p}} = 1.5\text{-}2$ V, depending on the distance between the paired electrodes and the given tube concentration.

After switching ON the rf-frequency generator, a drop of the surfactant-stabilized SWNT suspension ($\sim 30 \mu\text{L}$) was applied to the chip with a pipette. A typical deposition time of a few minutes⁴ was then followed by rinsing the sample with methanol and gently blowing the drop off the surface by means of a regulated nitrogen gas flow. Finally, the generator was turned OFF. The sample was next unwired (with caution not to discharge it) and annealed for 2 hours at 200°C in air before being subjected to characterization by scanning electron microscopy (SEM) and atomic force microscopy (AFM) to assure the presence of an individual SWNT. The simultaneous deposition of individual SWNTs with reproducible alignment on several

²The boron doped p-type silicon substrate exhibits very low resistivity $\rho = 0.001\text{-}0.005 \Omega\text{cm}$ and thus serves as a metal electrode.

³The lithography step was performed in a LEO 1530 scanning electron microscope using RAITH ELPHY PLUS software.

⁴Depending on the gap between the electrodes, $V_{\text{p-p}}$ and the tube concentration used, the time deposition was varied to optimize the deposition results, *i.e.*, to achieve as many pairs as possible with only one SWNT.

3. Experimental

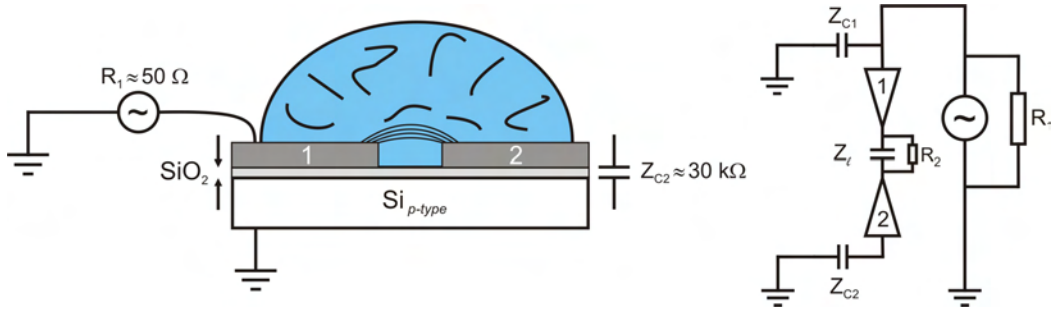


Figure 3.3.: On the left, a side view of the deposition of SWNTs onto an electrode pair is demonstrated. The applied drop contains stabilized-SWNTs suspended in SDBS. Lead 1 is wired to a frequency generator. An impedance of $Z_{C2} \approx 30 \text{ k}\Omega$ at 300 kHz couples the floated electrode (lead 2) to the grounded p-type Si substrate. The thermally grown SiO_2 is $800 \text{ nm} \pm 10 \text{ nm}$ thick. On the right, the top view of the circuit is schematically displayed with sharp tip electrodes. Z_l is the impedance of the medium between the electrodes. A resistor R_2 exists in parallel as some current can pass through the suspension medium. Close to the tip edge, the electrodes are about 200 nm wide.

contacts is the result of such a procedure [52, 71]. The deposition scheme is based on capacitive coupling between the floating leads and the ground. Even though the capacitive coupling in a solvent medium is quite complicated to calculate, it can be estimated from the given configuration geometry. In Fig. 3.3 the impedance Z_{C2} , which couples the floating electrode (lead 2) to the grounded substrate, is shown for one pair of electrodes. Based on geometry, a typical capacitance of $C \approx 100 \text{ pF}$ results in an impedance on the order of $Z_{C1} = Z_{C2} \approx 30 \text{ k}\Omega$ if a frequency of 300 kHz is used.

In principle, the potential difference between the driven and floating electrodes can be maintained up to a frequency of $\sim 20 \text{ MHz}$. At high-frequencies the capacitive coupling impedance Z_{C1} becomes comparable in magnitude to the load resistor of the frequency generator R_1 and the potential on electrode 1 will be smaller than the actual applied bias⁵. Nevertheless, for the deposition of both types, metallic and semiconducting SWNTs, low-frequency dielectrophoresis is required. Performing the deposition at 300 kHz ensures that the potential of the floating electrode remains coupled to the ground via Z_{C2} as long as no ohmic contact has been formed. Once a bridging SWNT produces an ohmic contact, the previously developed potential drops and the dielectrophoretic force \vec{F}_{DEP} is no longer present to attract additional

⁵At high-frequencies the coaxial cable impedance also becomes comparable in magnitude to R_1 . The additional loss in the coaxial cable also inhibits the potential from building up.

3.2. Deposition of SWNTs via low-frequency dielectrophoresis

tubes. The dielectrophoretic process which pulls the SWNTs toward the central area between the electrodes originates from the interaction between the induced dipoles $\vec{\mu}_{ind}$ of polarized SWNTs and the external inhomogeneous electric field located between opposing leads. The strength of the \vec{F}_{DEP} depends on the magnitude of the inhomogeneity of the field which in turn depends on the electrode geometry and therefore the electrodes were fabricated to have a sharp tip at opposing edges, as demonstrated in Fig. 3.3. If for example a metallic SWNT is trapped in a way that it bridges the electrodes, the initial impedance of the liquid medium Z_l is replaced by the metallic SWNT impedance of magnitude $Z_m \geq 6.5 \text{ k}\Omega$. Since $Z_m \ll Z_{C2}$, the current passes through the tube to electrode 2 and a potential-difference no longer exists. However, the surfactant-stabilized SWNT suspension contains at least 250 times more non-conducting surfactant molecules than tubes⁶. As the surfactant molecules adsorb at the tube surface, they can create a tunnelling barrier to the leads. Accordingly, even in the case of a metallic SWNT, the potential difference between the electrodes may remain. As discussed in section 2.5.5 the semiconducting SWNTs have also a finite conductivity due to their induced surface conductance. Besides bridging with a metallic tube or SWNT bundles (or switching OFF the generator), a semiconducting tube can create a low ohmic contact and stop the deposition. Accordingly, an optimum regarding the various free parameters was required in order to deposit only one SWNT at each contact. Further, the randomly-oriented polarized SWNTs in the suspension line up along the field lines during the deposition as their induced dipole points mainly along their axis. Consequently, in most cases a straight SWNT connects the electrodes.

The given layout possesses a set of 18 paired electrodes where each follows the above description. However, all floating electrodes are individually coupled to the ground, resulting in an independent deposition of SWNTs for the characteristic length scales involved (20 μm distance between pairs). Further, the scheme requires only one bond wire for all driven electrodes, regardless of how many pairs are displayed. Typically 5 out of 18 contact pairs are bridged by one individual SWNT. This representative result depends on the suspended SWNTs length-variations and the residual bundle content. Most of the remaining contacts are either not fully bridged (short tube-segments) or bridged by bundles. Since bundles have bigger volume

⁶Considering surfactant and tube concentrations of 0.5% and 0.02 mg/ml, respectively, one can in principle obtain (in w-%) 250 times more surfactant molecules than tubes, keeping in mind that the surfactant molecules are partially aggregated.

3. Experimental

than individual SWNTs, if present in the suspension, they will be attracted first by the dielectrophoretic force, as specified in Eq. 2.33. The dielectrophoresis technique is accordingly a very sensitive tool to judge the content of bundles in a surfactant SWNT-stabilized suspension⁷. Bare contacts occur if a combination of very low tube concentration and of short time deposition is used, or alternatively if the contact leads were of poor quality and could not drive the current.

3.2.1. Two-point resistance measurements

Contacts closed by individual SWNTs were characterized by electrical transport measurements and subsequently by resonant Raman spectroscopy. An example of a candidate SWNT can be found in Fig. 4.2. Electrical transport measurements were carried out with Keithley 6430 and 2400 SourceMeters. The measurements were performed at a constant source drain voltage V_{SD} , where the source drain current I_{SD} was measured while changing the gate voltage V_G . Unless otherwise specified, all electrical measurements were carried out under ambient conditions of room-temperature and pressure on the order of 10^{-5} mbar.

An illustration of such a setup in a two-point resistance geometry is given in Fig. 3.4. On the left of Fig. 3.4, the chamber in which the electrical measurements were carried out is shown. The schematic drawing on the right of Fig. 3.4 demonstrates how a bonded SWNT bridges the source and drain electrodes. The SWNT is placed on top of the oxide layer where its ends lie on top of the metal electrodes. This *tube-on-metal* configuration normally displays much higher contact resistances than the *metal-on-tube* arrangement. In section 4.1 the observed resistances for metallic and semiconducting SWNTs measured for the *tube-on-metal* design are specified for Au and Pd metal electrodes. Metallic SWNTs display an average resistance of a few hundred of k Ω s whereas for semiconducting SWNTs the average resistance in the ON state is a few hundred of M Ω s. In order to improve the contact resistances in a way that the current in metallic tubes reaches the saturation limit, a second lithography step was necessary to achieve the *metal-on-tube* configuration, and is discussed in section 4.6.3.

⁷Even if a SWNTs suspension presents very good fluorescence spectra it can still contain a certain amount of bundled material.

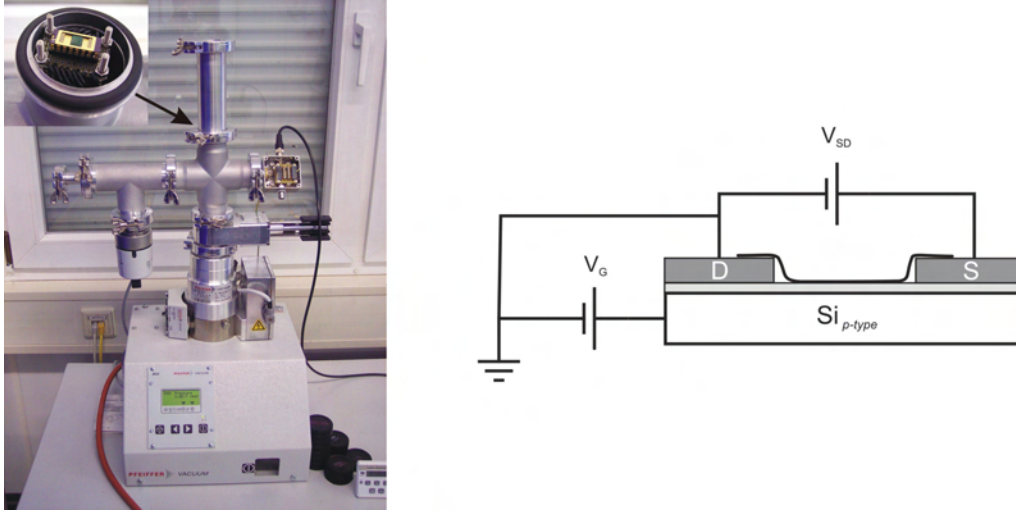


Figure 3.4.: (Left) The chamber used for electrical measurements. The inset shows a top view of a chip carrier sitting in the socket where the arrow shows its location in the chamber. (Right) A schematic illustration of a bonded SWNT prepared for electrical transport measurement. The driven source (S) and the grounded drain (D) electrodes are indicated. The degenerately doped Si substrate serves as a gate electrode. Note that the bridging SWNT adheres strongly to the underlying oxide layer via van der Waals interactions.

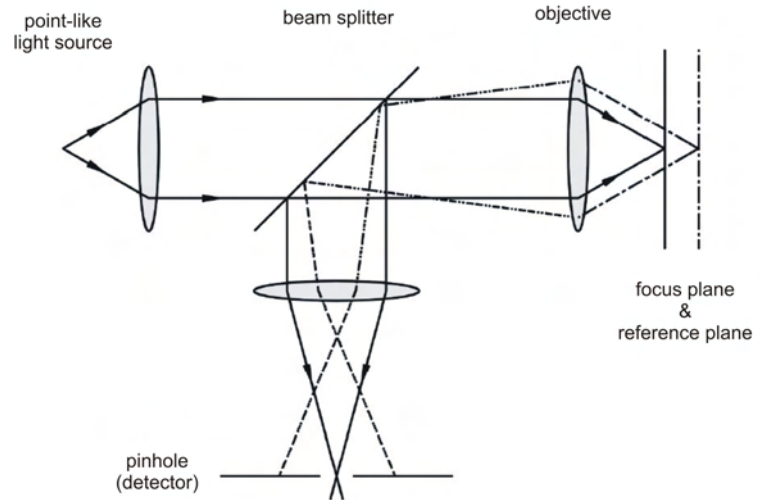
3.3. Confocal Raman Microscope (CRM)

Resonant Raman measurements were performed with a WITec CRM 200 confocal Raman microscope. The samples were excited with an Ar-ion laser at 2.41 eV (514.5 nm) or He/Ne laser at 1.96 eV (632.82 nm). A laser power of ~ 3 mW was applied to the sample where the power density is found by means of division by the spot size, as discussed in section 3.3.1. Raman spectra were recorded in air ambient at nominally room-temperature (or when specified under Ar atmosphere) with the polarization of the incident light parallel to the long axis of the electrodes. The spectra were recorded over a broad spectral range so that the high and low energy Raman modes could be measured simultaneously. This limits the spectral resolution⁸ to 6 cm^{-1} , however, the peak positions could be measured with better than 1 cm^{-1} accuracy (calibration error). The metallic SWNTs were excited by the red laser through the first pair of van Hove singularities (E_{11}^M) and the semiconducting SWNTs were excited by the green laser through the third pair for optical transition

⁸The spectral resolution was determined by the FWHM of emission lines originating from a standard gas discharged lamp, *e.g.*, Ne or Xe lamps.

3. Experimental

Figure 3.5.: Schematic drawing of the confocal microscope setup. Note that only rays from the image focal plane can reach the detector. Taken from Ref. [72].



(E_{33}^S), see also Fig. 4.5 in section 4.4. Some information regarding the principal setup of a confocal Raman microscope is given below.

3.3.1. The CRM 200 Raman microscope

The CRM 200 employs a triple grating Raman spectrometer along with a high spatial resolution confocal microscope. The setup which includes the microscope, the spectrometer and the detectors is optimized to provide high sensitivity, so signals could be easily and accurately obtained from a very small amount of material [72]. In this study the CRM 200 was used to collect the Raman spectrum of selected individual SWNTs. The capacitively controlled piezo stage ensured that the detected nanotube remains under the focused beam throughout the whole integration or accumulation time needed for a resolved signal (*i.e.*, allowing for correction of thermal drift).

Confocal Raman microscopy

In confocal microscopy a point-like light source (laser) is focused via an objective onto a sample. The scattered Raman light is collected via the same objective and focused into a pinhole that is located in front of the detector. The setup controlling the path of incident and scattered light is illustrated in Fig. 3.5. It ensures that only rays from the focal plane can pass the pinhole and reach the detector. For Raman imaging experiments, such a geometrical picture provides a three-dimensional image of high contrast.

An enhancement of the lateral resolution in confocal microscopy requires extremely small pinhole diameters, which leads to a major decrease in detection efficiency. The intensity dependence on the pinhole size is given in Fig. 3.6. The choice of optimum pinhole size is discussed in the next section.

In the setup of the CRM 200, the single wavelength excitation laser light is delivered through a single-mode optical fiber. The scattered Raman light is collected by the objective, passes through a holographic notch filter and is focused into a multi-mode fiber. The latter directs the scattered radiation toward the spectrometer that is equipped with both a CCD camera and a photon counting detector (APD). Note that the core of the multi-mode optical fiber operates as a pinhole. The laser is focused onto a sample which is located on a piezo table that can move in X, Y and Z directions. The beam-path from the laser source till the detector is shown in Fig. 3.7.

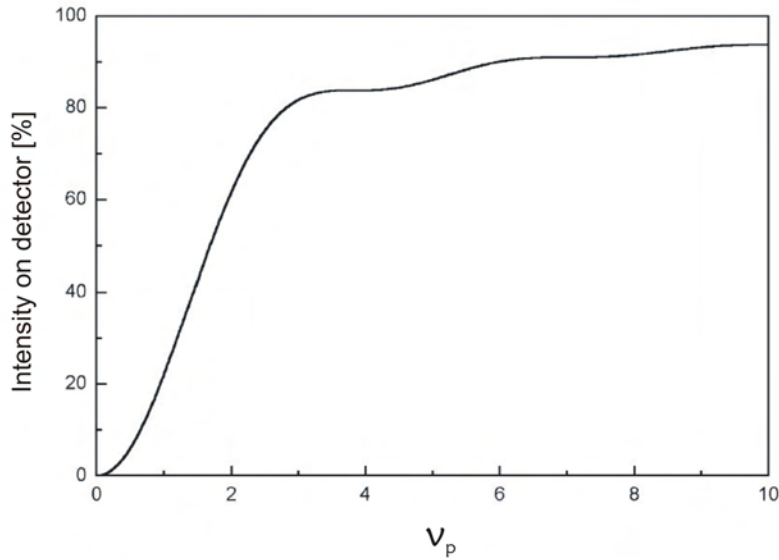


Figure 3.6.: Normalized collection efficiency as a function of pinhole size v_p . The collection efficiency is about 75% for maximum depth resolution ($v_p = 2.5$) however merely 6% for maximum lateral resolution ($v_p = 0.5$). Note that the pinhole size is given in optical coordinates^a via the relation $v_p = v/M = \frac{2\pi \cdot r_p \cdot n \sin \alpha}{\lambda_{\text{exc}} \cdot M} = \frac{\pi d_p \cdot N_A}{\lambda_{\text{exc}} \cdot M}$ with the numerical aperture $N_A = n \sin \alpha$, the radius (or diameter) of the pinhole (r_p or d_p), the magnification (M), the medium refractive index (n) and α defined as half of the objective aperture angle $0^\circ < \alpha < 90^\circ$. Taken from Ref. [72].

^aThe optical coordinates (u, v) are defined via: $u = kz \sin^2 \alpha$ and $v = k\sqrt{x^2 + y^2} \sin \alpha$. $k = \frac{2\pi}{\lambda_{\text{exc}}}$ is the light wave vector and is defined by the excitation wavelength (λ_{exc}) [72].

3. Experimental

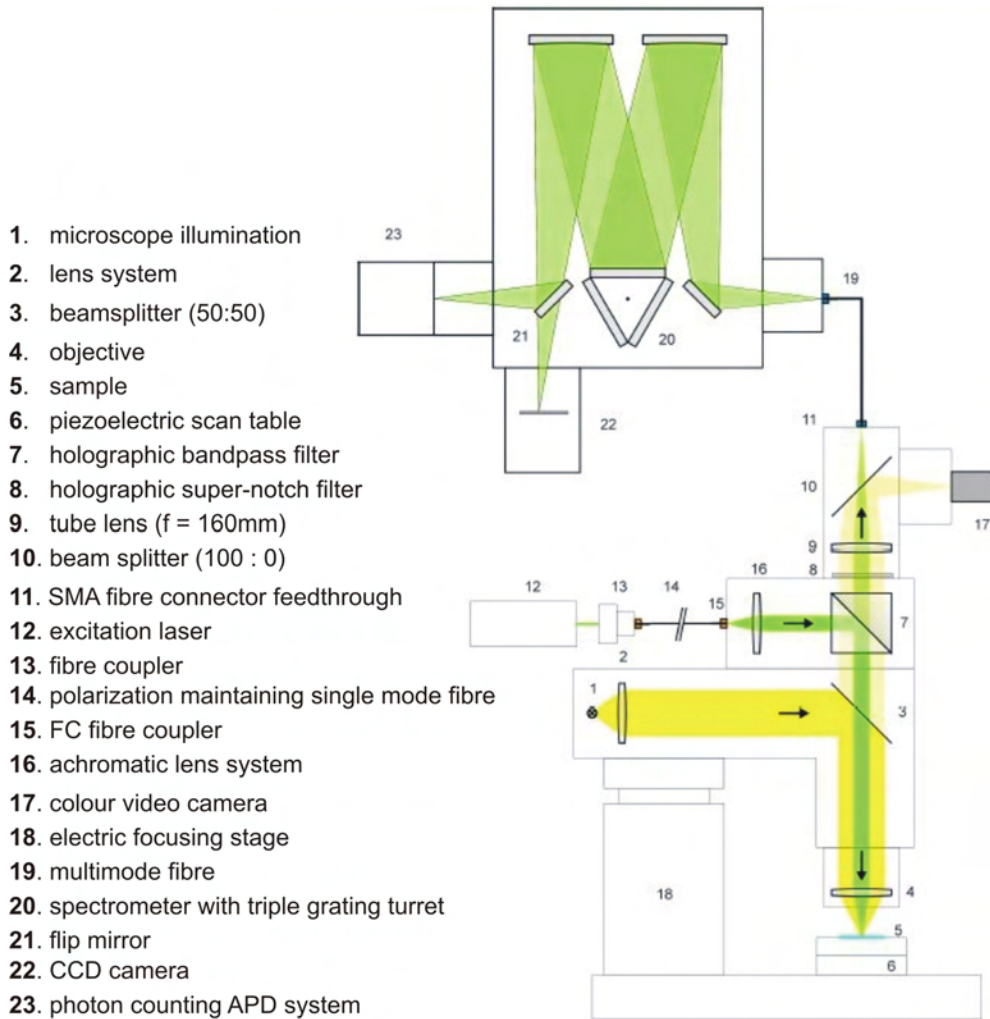


Figure 3.7.: Beam-path as given for a CRM 200 setup. The relevant parts are listed in the figure. Note that as fibers are used for beam delivery and signal pick-up, the excitation laser, the spectrometer and the detectors do not have to be firmly attached to the microscope. Taken from Ref. [72].

The optimum pinhole size

In general, the multi-mode flexible fibers are protected against mechanical strain and interference from stray light. The selected fiber can be adjusted laterally to achieve a maximum in scattered light collection efficiency. Typical pinhole sizes are 10 - 100 μm where our CRM 200 is equipped with either 25 μm , 50 μm or 100 μm core diameter fibers. The measurements in this study employed the 50 μm fiber. Using the 100 μm fiber however provided a better Raman signal, but was used only

Table 3.1.: $\frac{\pi d_p}{v_p \lambda}$ values for various wavelengths and pinhole sizes. v_p was assigned 2.5 (optical coordinates) to assure no loss in depth resolution. To obtain the highest lateral resolution, v_p should be below 0.5. The marked green and red lasers were used in this study. Numbers are rounded for the ease of presentation. Modified from Ref. [72].

Pinhole diameter d_p (μm)	λ (nm)					
	440	488	514	532	633	785
10	29	26	24	24	20	16
25	71	64	61	59	50	40
50	142	129	122	118	99	80
100	286	258	244	236	199	160
200	571	515	489	472	397	320

in cases where lateral resolution was of less importance. The optimal choice of pinhole size is determined by the following relation:

$$\frac{M}{N_A} = \frac{\pi d_p}{v_p \lambda} \quad (3.1)$$

with magnification M , pinhole diameter d_p and objective numerical aperture N_A . The choice of M and N_A is often limited to available objective. Therefore, one should chose an objective that either satisfies Eq. 3.1 or with bigger M/N_A ratio. Two one hundred fold (100x) objectives were used in our experiments. One with $N_A = 0.9$ and the other with $N_A = 0.7$, which yield the numbers ~ 111 and ~ 142 , respectively for the parameter M/N_A given in Eq. 3.1. The right side of Eq. 3.1 is defined by the wavelength λ and the pinhole size. Table 3.1 lists some $\frac{\pi d_p}{v_p \lambda}$ values for typical wavelengths and pinhole sizes.

Based on the M/N_A relation and the values given in Table 3.1 one can determine the optimal pinhole size for a specific experiment. For the 100x objectives with the 0.9 and 0.7 numerical apertures, if used at 514 or 633 nm wavelengths, the optimum pinhole size should be 50 μm for maximum depth resolution and 10 μm for maximal lateral resolution. However, since individual SWNTs were the targets for detection, 50 μm fiber was the smallest core diameter used. No Raman signal from SWNTs could be detected when using smaller pinhole sizes.

3. Experimental

Lateral resolution

Both numerical aperture and excitation wavelength determine the lateral resolution of the objective. The magnification value is of importance only for the determination of optimum pinhole size. In order to determine the maximum resolution of a classical microscope one uses the Rayleigh criterion:

$$\Delta x = \frac{0.61 \lambda}{N_A} \quad (3.2)$$

with Δx defining the smallest distance between two separated point objects in the image plane. As mentioned above, a laser power of ~ 3 mW was applied on the sample. With Eq. 3.2 one can estimate the power density. Laser spots are about 350 nm and 430 nm in diameter if a 100x objective with $N_A = 0.9$ is used with green and red lasers, respectively. Alternatively, if the objective with $N_A = 0.7$ is used, spot sizes of ~ 350 nm and ~ 550 nm are obtained for the green and red lasers, respectively. The corresponding power densities are approximated 2.4 MW/cm² (350 nm spot size), 1.6 MW/cm² (430 nm) and 1 MW/cm² (550 nm).

4. Results and discussion

The challenge of achieving the bridging of an individual SWNT across preformed metal electrodes on a multiple contact chip became a simple task to accomplish when using a technique based on a low-frequency dielectrophoretic deposition, as developed by Krupke *et al.* [70, 73]. The technique was invaluable throughout this study. Besides being a simple and reasonably fast procedure, one of its major advantages is the beforehand knowledge of the SWNT position on the chip, that is, the deposited SWNTs can be found only in the areas between the electrodes. In most cases, the SWNTs are additionally aligned parallel to the pre-patterned electrodes, an advantage for subsequent characterization like the study of phonon modes by resonant Raman spectroscopy, which depends on the polarization of the incident photons with respect to tube axis. Nevertheless, in this thesis it was established that without extra fabrication steps, the observed resistances of both metallic and semi-conducting individual SWNTs were still high, compared to the quantum resistance. The experimental findings regarding the resistances of individual SWNTs, fabricated with and without an extra lithography step to make better electrical contacts, are displayed and discussed. A sequential study of the electrical transport and resonant Raman spectroscopy of the same individual SWNTs is presented. Subsequently, a *simultaneous* electrical and resonance Raman scattering study was performed on individual metallic SWNTs. The latter provides the effective-temperature of the phonons involved in the Raman scattering processes occurring in the metallic nanotube. Some preliminary results concerning how to realize the electrical behavior needed from an individual SWNT for electroluminescence experiments are also presented.

To the best of our knowledge, prior to the work of this thesis and associated publication [52], no systematic Raman study of individual SWNTs had shown additional electrical transport measurements to support the interpretation of spectral data, except for two attempts that were lacking a radial breathing mode (RBM) signal

in their Raman spectrum [74, 75]. In order to address the question whether the metallic or the semiconducting character of a SWNT, as derived from electrical transport measurements indeed correlates with a type specific Raman spectrum, we have studied 25 individual metallic and semiconducting SWNTs. As a result of these measurements we solve the debate about the line-shape of the peaks of metallic *versus* semiconducting SWNTs and how these arise from scattering processes, involving high-energy phonons.

4.1. Contact resistance measurements of individual SWNTs: tube-on-metal

Individual SWNTs were bonded for electrical transport measurements as discussed and illustrated in section 3.2.1. The observed average resistance was on the order of hundreds k Ω for metallic SWNTs (as illustrated in Fig. 4.1) and could reach up to 1G Ω in the case of semiconducting tubes (ON state). One major reason for these high values originates from the high contact resistances, as a very small contact area is obtained via the tube-on-metal configuration. In this situation most of the applied voltage drops at the contacts. In contrast, much lower contact resistances are obtained for the metal-on-tube configuration as observed by many groups over the world including the present work (section 4.6.3). Nevertheless, the initial objective was to perform a systematic study which correlates electrical transport with resonant Raman measurements on the same individual SWNT, using the tube-on-metal configuration. Figure 4.1 illustrates the contact resistances obtained for metallic SWNTs via Pd/Ti or Au/Ti metal electrodes in the tube-on-metal configuration. Although both metal combinations show high contact resistances, as long as the source-drain current could be measured as a function of gate voltage, a distinction between metallic and semiconducting tubes could be achieved, as discussed in section 2.3. Further, the Pd/Ti rather than the Au/Ti combination was eventually used for the study since it provided lower contact resistances.

Figure 4.1 further illustrates the way in which the Δ magnitude was determined, that is, the difference between the differential conductance at zero bias and the differential conductance maxima at approximately ± 0.8 V. The dependence of the bias on the differential conductance is characteristic for high- or low-contact resistances, as was demonstrated by Yao *et al.* [9] at different temperatures.

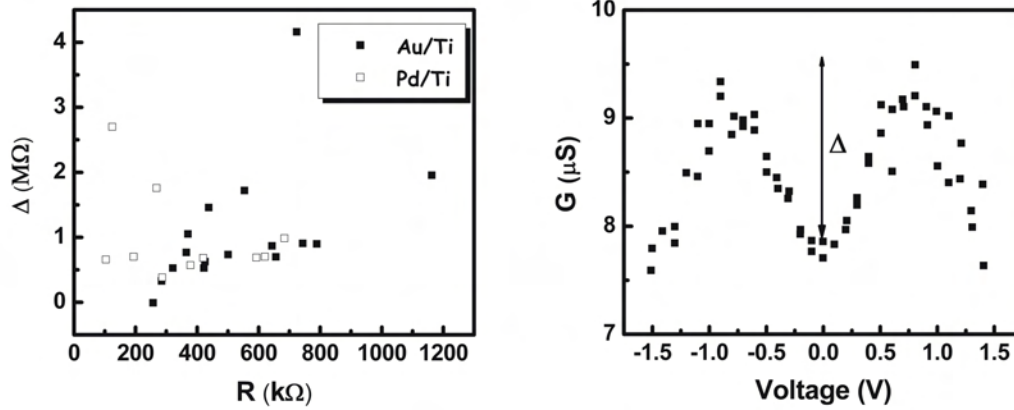


Figure 4.1.: Metallic SWNTs resistances for the tube-on-metal configuration with Pd/Ti or Au/Ti metal electrodes. The Pd/Ti combination reveals lower average resistances. The way in which the Δ conductance (resistance) at zero bias was determined after taking the derivative of the current with respect to voltage is shown on the right.

Since individual SWNTs were the test objects, it was first necessary to assure that no bundles were involved, *i.e.*, bridging the metal electrodes. This was done by imaging individual SWNTs with an atomic force microscope apparatus.

4.2. AFM imaging of aligned SWNTs

A MultiModeTM atomic force microscope (AFM) apparatus manufactured by Digital Instruments was used to image the SWNTs. The tapping mode for imaging was used in air ambient by oscillating a Silicon cantilever. The specific noncontact cantilever used (NSC15) has a resonant frequency which ranges between 265-325 kHz and an attached Silicon tip of less than 10 nm radius of curvature. Tip height is 15.2 μm . Figure 4.2 shows an example of a wired (*i.e.*, electrically contacted) individual SWNT deposited via low-frequency dielectrophoresis as discussed in section 3.2 and imaged by tapping mode AFM. Looking at the AFM image, one observes dots on the substrate and furthermore that the tube diameter varies along its length. These features are attributed to surfactant molecules. Surfactant-free tube-sections were therefore used to determine the SWNT diameter. The vertical resolution of the AFM (± 0.2 nm) allows one to distinguish an individual SWNT or a 2-tube bundle from a closed packed 3-tube bundle, which for the range of tube diameters

4. Results and discussion

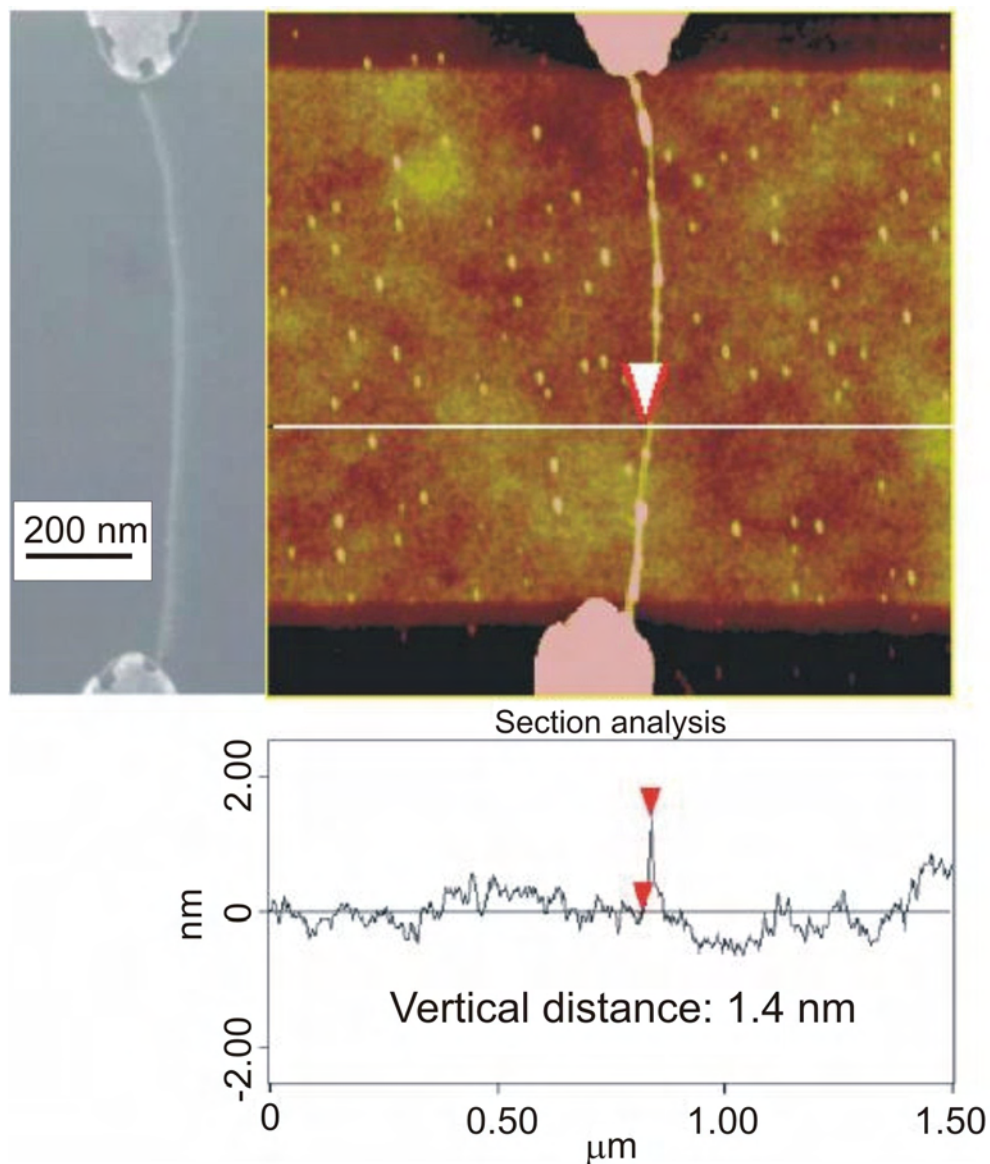


Figure 4.2.: Example of an individual SWNT, imaged by scanning electron microscopy (left) and atomic force microscopy (right). The tube was deposited between Pd/Ti electrodes via the low-frequency dielectrophoresis method. The measured height of the tube has been used to exclude the presence of a bundle with three or more tubes. Dimers remain unresolved. Dots in the AFM topography image reveal residual surfactant molecules, on and in the vicinity of the SWNT. The AFM cross section was taken at a surfactant-free tube segment. Sample w112c23p1.

used here (1-1.5 nm) and simple geometry arguments yields heights of 1.9 - 2.8 nm. A SWNT was thus assigned individual when its diameter was ≤ 1.7 nm, taking into account an error of ± 0.2 nm.

4.3. Electrical transport and resonant Raman spectroscopy on the same individual SWNT

Individual SWNTs for which both electrical transport measurements and clear RBM region spectra were obtained are discussed below [52, 76]. We emphasize the RBM appearance as it indicates a resonance occurrence. The single-resonance model implies that Γ -point phonons are involved in the scattering process and therefore directly observed in the spectrum. In contrast, the double-resonance model allows phonons with $q > 0$ to participate in the scattering processes as well. Since the phonon dispersion of the RBM mode is limited to $q \approx 0$, as indicated in Fig. 2.11, its signal is confined to a very narrow resonance window. Further, the G mode line-shape within the double resonance picture is excitation-energy dependent, *i.e.*, if for example a metallic nanotube is non-resonantly excited, its G line-shape can be misleading by displaying a narrow semiconducting-like peak shape rather than a broad one [48]. The appearance of a RBM signal is therefore crucial and eliminates non-resonantly excited tubes from further investigation.

Figure 4.3 shows the transport measurements and the corresponding Raman signals of two representative semiconducting and metallic individual SWNTs. Note that the SWNTs studied were fabricated in the tube-on-metal configuration without a second lithography step. The upper-left part of Fig. 4.3 represents a typical gate dependence as observed on 15 individual tubes (appendix C) where the source drain current, I_{SD} , strongly depends on the applied gate voltage, V_G . Switching between the ON and OFF states is accompanied by a rather strong hysteresis, possibly originating from the reorientation of dipolar surfactant or adsorbed water molecules [24], or alternatively due to trapped charges in the gate oxide [25]. The result is typical for Schottky-barrier type field effect transistors (SB-FET) based on individual semiconducting tubes, which exhibit a p-type behavior due to oxygen exposure [28, 77, 78]. The corresponding Raman spectrum is located in the upper-right part of Fig. 4.3 and shows a RBM signal at 193.7 cm^{-1} , a disorder D mode at 1348 cm^{-1} , and a narrow G mode at around 1590 cm^{-1} . The lower-left part of Fig. 4.3 (b) represents another type of gate dependence as observed on an additional 10 individual tubes (appendix C). The device can not be switched OFF at any gate voltage and exhibits a nearly constant I_{SD} for any V_G applied. This behavior is typical for a wired metallic tube, where the gate potential does not change the number of conduction channels. The corresponding Raman spectrum in the lower-right part of Fig. 4.3

4. Results and discussion

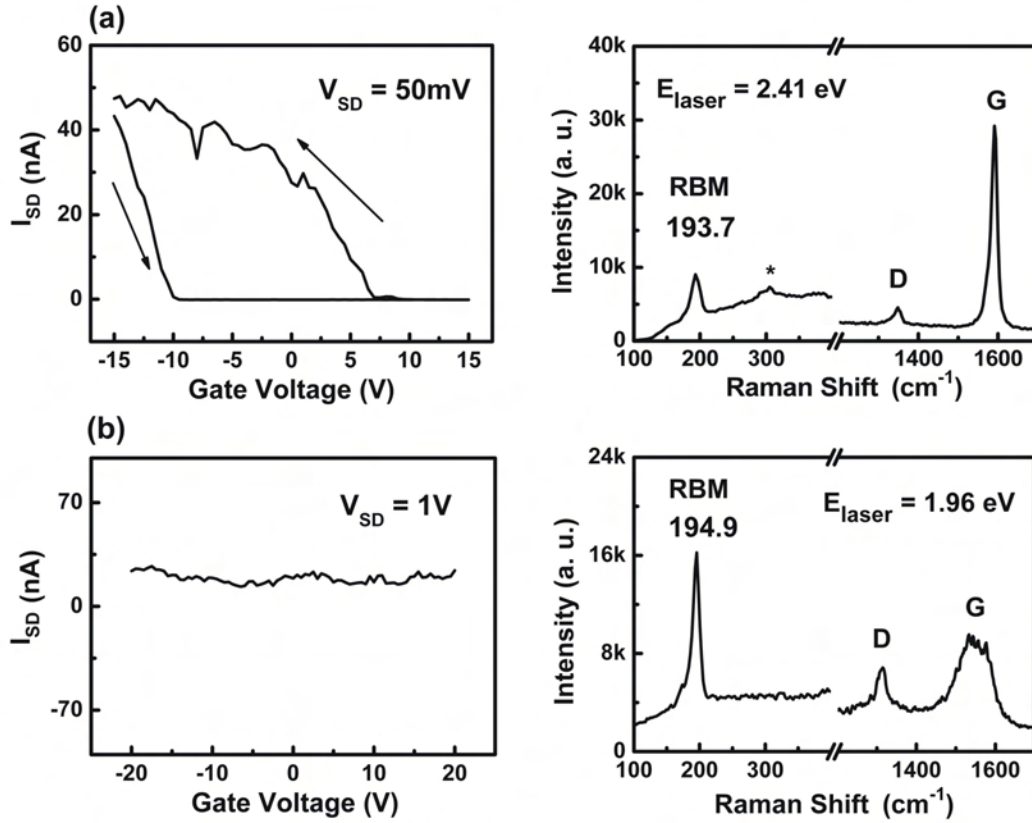


Figure 4.3.: Electrical transport measurements (left) and the corresponding Raman spectra (right) of an individual semiconducting SWNT (a) and an individual metallic SWNT (b). The type of tube is identified by the specific gate voltage dependence of the source drain current (I_{SD}) and the spectral shape of the G mode. For semiconducting SWNTs, the typical hysteretic gate dependence appears in combination with a narrow G mode. In contrast, for metallic SWNTs, showing no gate dependence, the G mode is broad. For most metallic or semiconducting SWNTs, the G mode appears rather weak or strong, respectively, compared to the RBM mode. Laser excitation energies E_{laser} , radial breathing mode frequencies and source drain voltage V_{SD} are indicated. A contribution from the Si substrate is indicated by an asterisk. The room-temperature Raman and transport measurement data were recorded in air and vacuum, respectively. Sample numbers are 3 and 12 as given in Tables 4.1 and 4.2 for the metallic and semiconducting tubes, respectively.

reveals a sharp RBM peak at 194.9 cm^{-1} , a D mode at 1310 cm^{-1} and a broad G mode peak ranging between $1500\text{-}1600 \text{ cm}^{-1}$.

The electrical behavior of the semiconducting SWNTs was further studied by applying different V_G cycles as shown in Fig. 4.4. The cycles always started at negative voltage. In the left part of Fig. 4.4 the first cycle was applied from -5 to 5V and back to -5V , whereas the last cycle started and finished at -20V . The collected data points

4.3. Electrical transport and resonant Raman spectroscopy on the same individual SWNT

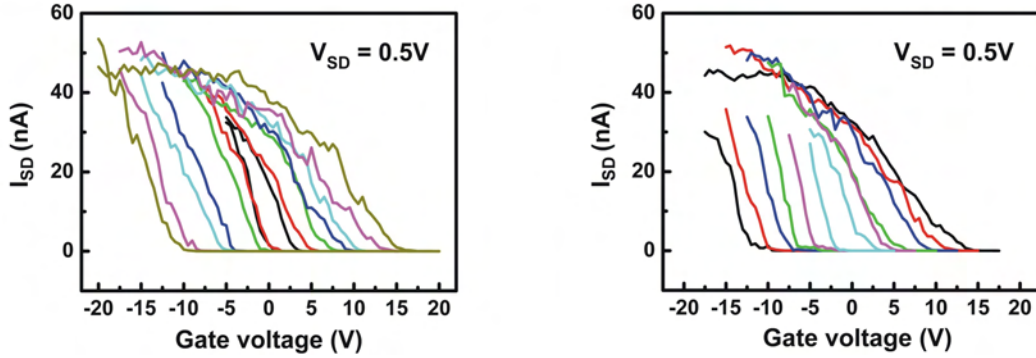


Figure 4.4.: Hysteresis effect in an individual semiconducting SWNT. (Left) gate dependence curves starting with small voltage range that increases to $\pm 20\text{V}$ and (Right) curves starting with high voltage range which decreases to $\pm 5\text{V}$. All electrical measurements were done on the same tube, with $V_{SD} = 0.5\text{V}$. The cycles started and finished at negative gate voltage. Sample w118c71p1a.

were in steps of 0.5V in all curves. The voltage range was increased by 5V between the different curves (*i.e.*, the second cycle started at -7.5V) where 7 curves are shown in total. In the right part of Fig. 4.4 the curves range decreased to $\pm 5\text{V}$, with the first starting at $\pm 17.5\text{V}$. Both parts of Fig. 4.4 show that the OFF (ON) state in all curves (left and right) shifts to lower negative (positive) voltage values, *i.e.*, the threshold gate voltage V_{th} in each curve, at which the SWNT begins to conduct, shifts by at least 5V where it can reach to about 25V as shown in the larger voltage ranged-curves. The threshold shift indicates that a screening of the gate voltage occurs [25]. It occurs either via a reconfiguration of local charges near the nanotube *e.g.*, water or surfactant molecules or alternatively via the injection of charges from the SWNT into its surrounding dielectric (here SiO_2) or its surrounding water and surfactant monolayer. Under the application of a gate voltage, charges injected from the tube screen the actual applied gate voltage. This occurrence reduces the actual applied gate voltage that the nanotube 'sees'. In the right part of Fig. 4.4 open curves are observed. The back cycle (from positive to negative voltages) in each curve seems to end with a higher current value than it began with. The origin of this occurrence is the screening of the gate voltage. As the data collection started a few seconds after the specific negative gate voltage (at which the cycle starts) was applied, some charge injection from the tube into its surrounding dielectric has already occurred. This causes the screening explained above and thus the current appears lower at the beginning of the measurement. Some charge reconfiguration

4. Results and discussion

may also contribute to the screening. Note that 15 minutes without either gate or source-drain voltage were given between the different measurements. The idea was to allow trapped charges or any dipolar molecule (surfactant or water) some time to relax. The results shown in Fig. 4.4 were obtained from the same tube and are a representative example for the devices studied here. In a recent study by Vijayaraghavan *et al.* [79] the same hysteresis behavior as in our devices was observed. They further measured the temperature dependence of the hysteresis behavior. It was concluded that the primary source of the hysteresis originates from the charge injection rather than the reorientation of the already existing dipolar water molecules (no surfactant was used in their experiments). Hysteresis behavior was still observed under conditions in which water molecules were definitely frozen. Hysteresis could therefore only originate from the screening charges that are injected from the nanotube itself into the surrounding dielectric [79].

4.4. (n,m) assignment

In order to assign $(n_1, n_2 \equiv n, m)$ values to our measured tubes, we compared the RBM frequencies of our individual metallic tubes with measured values from Telg *et al.* [80] and Fantini *et al.* [41] taking into account an excitation resonance window of $E_{\text{laser}} = 1.96 \pm 0.1$ eV (Table 4.1). In agreement with Hennrich *et al.* [81] we have identified tubes which belong to the lower and upper branches of E_{11}^M . The data from our individual semiconducting tubes were compared with excitation energy calculations of Reich *et al.* [82] taking into account an excitation resonance window of $E_{\text{laser}} = 2.41 \pm 0.1$ eV. Good agreement is observed for tubes with $(n-m) \bmod 3 = +1$ (Table 4.2). The identified tubes are labelled in Fig. 4.5.

Note that the suggested assignment is based only on our measured RBM frequencies as we have no means to measure the Raman excitation profiles. Accordingly, we were forced to rely on other experimental measurements for the correlated excitation energies. An accurate assignment must ideally include both RBM frequency and excitation energy.

4.5. G band broadening of metallic SWNTs

A clear systematic correlation between electrical transport measurements and Raman spectra for metallic and semiconducting SWNTs was displayed in Fig. 4.3 and

Table 4.1.: Raman data analysis of individual metallic SWNTs. Width of fitted G^- mode (ΔG^-), FWHM of the G mode and RBM frequency. V_G^{dep} stands for gate dependence. The data is compared with referenced experimental data and the SWNTs were assigned accordingly. Note the spectral resolution of 6 cm^{-1} .

sample no. (w118c)	Experimental				Comparison		
	V_G^{dep}	ΔG^- (cm^{-1})	FWHM (cm^{-1})	ω_{RBM} (cm^{-1})	ω_{RBM} (cm^{-1})	(n,m)	E_{11}^{M} (eV)
1. (75p3e)	no	43.7 ± 2.3	47.0 ± 1	202.1 ± 1.84	204.0^{\S}	(10,7)	2.07^{\S}
2. (103p2c)	no	52.1 ± 7.0	56.0 ± 5	202.1 ± 1.2	204.0^{\S}	(10,7)	2.07^{\S}
3. (106p1c)	no	74.8 ± 2.0	99.0 ± 1	194.9 ± 1.1	195.3^{\S}	(13,4)	1.93^{\S}
4. (66p1f)	no	61.8 ± 1.8	83.0 ± 1	161.0 ± 1.1 178.2 ± 1.2	160.3^a $179.9^{\#}$	(11,11) (14,5)	1.83^a —
5. (06p2e)	no	50.2 ± 1.8	68.0 ± 1	194.9 ± 1.2	195.3^{\S}	(13,4)	1.93^{\S}
6. (09p1b)	no	42.0 ± 1.5	56.0 ± 1	200.0 ± 1.3	201.5^{\S} 200.5^{\ddagger}	(15,0) (14,2)	1.86^{\S} 1.92^{\ddagger}
7. (09p3e)	no	58.5 ± 2.8	85.0 ± 2	185.6 ± 1.4	185.4^{\ddagger}	(11,8)	1.90^{\ddagger}
8. (09p1f)	no	41.4 ± 1.2	57.0 ± 1	196.0 ± 1.3	196.5^{\ddagger}	(13,4)	1.93^{\ddagger}
9. (45p2e)	no	54.5 ± 1.7	69.0 ± 2	162.6 ± 1.3 187.6 ± 1.3	$164.9^{\#}$ 189.6^{\S}	(15,6) (12,6)	— 1.94^{\S}
10. (09p3b)	no	56.9 ± 2.4	72.0 ± 1	168.0 ± 1.1	$170.4^{\#}$	(17,2)	—

Symbols \S , $\#$ and \ddagger denote Refs. [80], [83] and [41], respectively.

^a Extrapolated from Ref. [41], see Fig. 4.5.

is also seen in all supporting material presented in appendix C. We identify a narrow G mode peak for semiconducting SWNTs and a wide G mode peak for metallic SWNTs. As first proposed by Piscanec *et al.* [84], the strong electron-phonon coupling in graphite should be relevant in SWNTs as well, and in particular for metallic SWNTs. According to the single-resonance model, the Γ -point phonons ($q \approx 0$) are observed with high intensity in the Raman spectrum if resonant transitions occur (section 2.4.1). A broadening of the Raman modes should result if strong electron-phonon coupling processes take place, with the corresponding acoustic, high-energy or zone-boundary modes, as was demonstrated in Fig. 2.7. Indeed, the G band in SWNT bundles exhibits a broad asymmetric BWF line shape. Following the theory of Kempa [56], it originates from the formation of a plasmon band that reduces the required momentum for the photonic excitation of the hybrid plasmon-phonon mode. Consequently, the broadening has been assigned to metallic tubes and used as a tool by various groups [48, 85] to identify whether a SWNT is metallic or semiconducting. Kempa [56] further claimed that on the level of individual metallic tubes, the upper energy side of the G band (the G^+ mode) should dominate and

4. Results and discussion

Table 4.2.: Raman data analysis of individual semiconducting SWNTs. Width of fitted G^- mode (ΔG^-), FWHM of the G mode and RBM frequency. V_G^{dep} stands for gate dependence. The data is compared with referenced experimental data and the SWNTs were assigned accordingly. Calculated excitation energies for most tubes with $(n - m) \bmod 3 = -1$ exceed the resonance window of $E_{\text{laser}} = 2.41 \pm 0.1$ eV. Note the spectral resolution of 6 cm^{-1} .

sample no. (w118c)	Experimental				Comparison			
	V_G^{dep}	ΔG^- (cm^{-1})	FWHM (cm^{-1})	ω_{RBM} (cm^{-1})	$\omega_{\text{RBM}}^{\#}$ (cm^{-1})	(n, m)	$E_{33}^{\text{S}\text{¥}}$ (eV)	$(n - m) \bmod 3 =$
1. (93p1e)	yes	17.0 ± 6.1	20.2 ± 1	198.5 ± 1.3	198.5	(12,5)	2.49	+1
				193.0 ± 1.5	192.7	(10,8)	2.59	-1
2. (95p2c)	yes	24.7 ± 2.3	27.7 ± 1	197.9 ± 2.3	198.8	(12,5)	2.49	+1
3. (108p2b)	yes	20.6 ± 2.4	24.5 ± 1	187.5 ± 1.2	187.4	(15,2)	2.35	+1
					187.4	(13,5)	2.70	-1
4. (113p1f)	yes	21.8 ± 1.5	21.0 ± 1	193.3 ± 1.8	192.7	(10,8)	2.59	-1
5. (103p1a)	yes	18.1 ± 3.3	18.0 ± 1	195.2 ± 1.2	193.8	(15,1)	2.78	-1
6. (103p3c)	yes	19.6 ± 2.2	20.0 ± 1	194.1 ± 1.2	193.8	(15,1)	2.78	-1
7. (110p1e)	yes	20.8 ± 1.7	23.0 ± 1	191.5 ± 1.1	191.6	(14,3)	2.77	-1
					191.6	(11,7)	2.47	+1
8. (119p3a)	yes	37.9 ± 4.4	42.0 ± 1	178.8 ± 1.1	178.1	(17,0)	2.62	-1
9. (114p2a)	yes	20.0 ± 2.4	20.0 ± 1	196.5 ± 1.4	198.5	(12,5)	2.49	+1
10. (126p3f)	yes	30.1 ± 2.7	34.0 ± 1	180.8 ± 1.2	179.8	(13,6)	2.32	+1
					181.6	(12,7)	2.54	-1
11. (136p2e)	yes	23.0 ± 1.5	20.0 ± 1	190.6 ± 1.1	191.6	(14,3)	2.77	-1
					191.6	(11,7)	2.47	+1
12. (04p1f)	yes	21.6 ± 3.6	19.0 ± 1	193.7 ± 1.1	192.7	(10,8)	2.59	-1
13. (84p2d)	yes	24.1 ± 5.9	32.0 ± 1	230.4 ± 1.1	229.1	(13,0)	2.70	+1
14. (75p2e)	yes	17.3 ± 2.3	20.0 ± 1	231.1 ± 1.1	229.1	(13,0)	2.70	+1
15. (95p2f)	yes	38.0 ± 3.1	29.0 ± 1	166.8 ± 1.1	165.9	(13,8)	2.35	-1

Symbols $\#$ and ¥ denote Refs. [83] and [82], respectively.

only a weak BWF line intensity should be present on the lower energy side of the G band, namely the G^- mode should only appear as a shoulder (see appendix D for details). We however demonstrate that **no BWF line is observed on the level of an individual metallic SWNT**. In contrast, we propose an alternative *electron-phonon coupling* mechanism as concluded from an analysis of the Raman G modes line shapes that can test the actual coupling mechanism involved in metallic SWNTs [52]. Figure 4.6 shows the Raman G band for all measured nanotubes. Figures 4.7 and 4.8 additionally display the peak positions and widths of each metallic and semiconducting SWNTs investigated in Fig. 4.6.

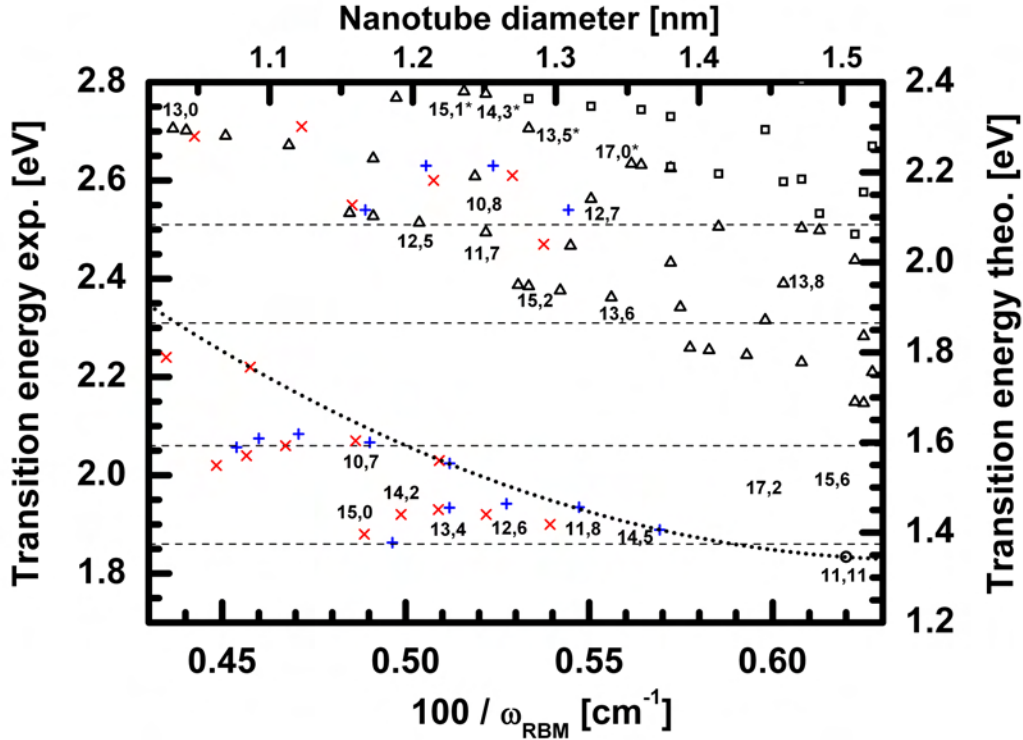


Figure 4.5.: Experimental and theoretical excitation energies of SWNTs *versus* the inverse RBM frequency based on data of Fantini *et al.* [41] (red crosses), Telg *et al.* [80] (blue pluses), and calculations of Reich *et al.* [82] (triangle and square for E_{33}^S and E_{44}^S transitions, respectively.) The dashed lines indicate the resonance windows $E_{\text{laser}} \pm 0.1$ eV ($E_{\text{laser}} = 1.96$ eV and 2.41 eV). The excitation energy of the (11,11) tube was derived by extrapolating the experimental (n,n) values of Ref. [41] (dotted line). Based on our Raman and transport measurements in combination with the above data we have identified the labelled tubes in our experiment. The identified tubes, highlighted with a star, belong to the $(n-m) \bmod 3 = -1$ family, which must have significantly lower excitation energies than theoretically predicted, in order to be detected at $E_{\text{laser}} = 2.41$ eV.

It is obvious that all nanotubes identified by transport measurements as semiconducting or metallic SWNTs exhibit a narrow or a broad G mode, respectively. This observation is in qualitative agreement with theory, which predicts narrow Lorentzian-line shaped G modes (G^+ and G^-) for semiconducting SWNTs and a broad BWF line shaped G^- mode for metallic SWNTs due to *phonon-plasmon coupling*. Yet within this theory, the G^- broadening is expected to be strong only in bundled metallic tubes and very weak in individual metallic tubes. However, our data on individual metallic tubes show that the G mode is dominated by a broadened G^- mode rather than showing a weak G^- shoulder. Moreover, the G

4. Results and discussion

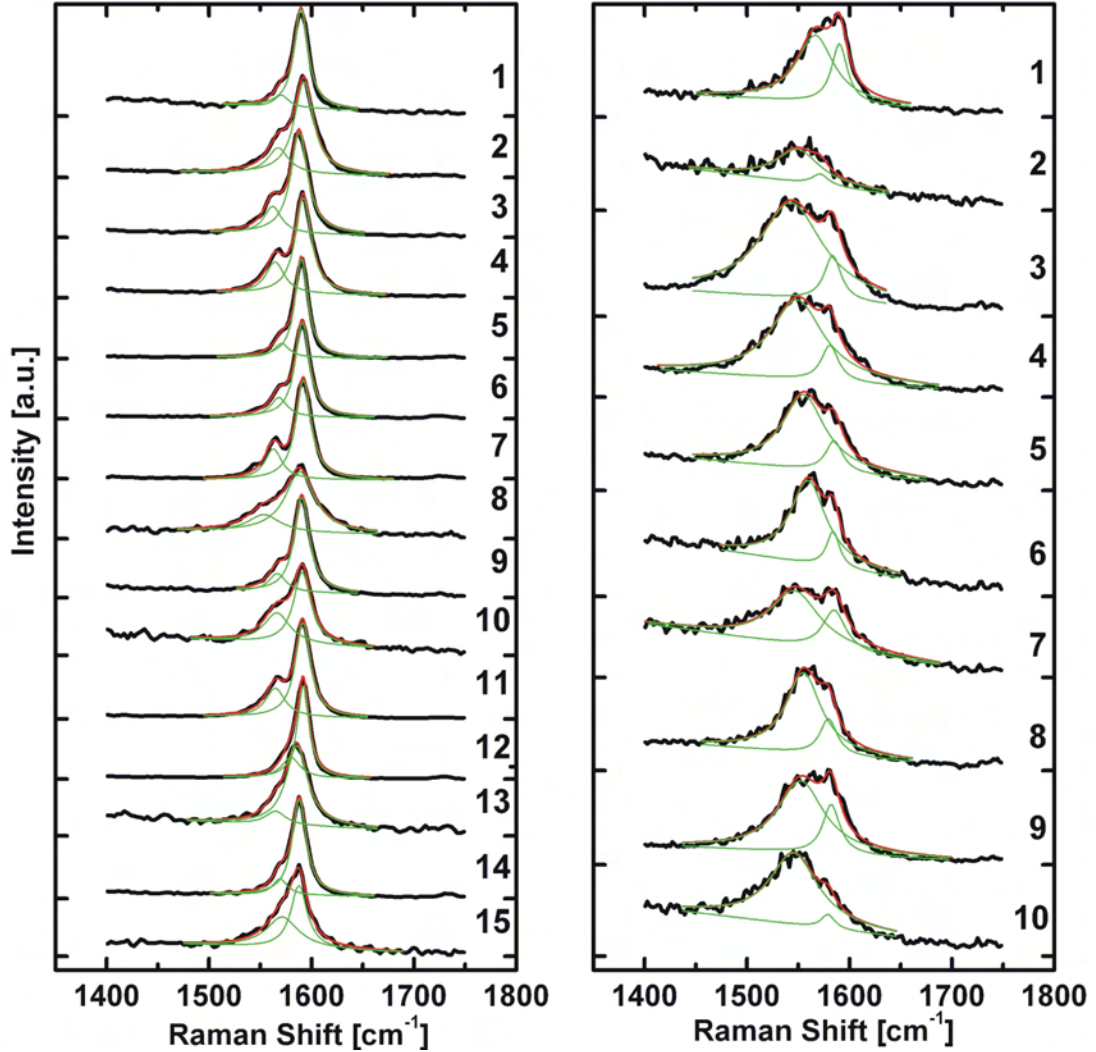


Figure 4.6.: Comparison between the Raman G modes of individual semiconducting (left) and individual metallic (right) SWNTs. The data has been fitted with two Lorentzian type components G^+ and G^- , corresponding to the circumferential (TO) and longitudinal (LO) vibrational modes respectively (red line). After background subtraction, a least square fit was obtained with the G mode positions and widths as free parameters (green line). Semiconducting SWNTs have a typical G^- width of $\Delta G^- \approx 20\text{-}30 \text{ cm}^{-1}$. For metallic tubes, $\Delta G^- \approx 40\text{-}60 \text{ cm}^{-1}$. The G^+ width, ΔG^+ , is for both tube types $\approx 20 \text{ cm}^{-1}$, a value which has been used to derive ΔG^- in cases where the double peak structure was not resolved. The spectra were shifted vertically for clarity. Sample numbering relates to Tables 4.1 and 4.2.

mode of individual metallic SWNTs were fitted well with two Lorentzians, taking into account the vibrational modes along the nanotube axis (LO) and the nanotube circumference (TO). This observation is important, since the model of Kempa [56]

4.5. G band broadening of metallic SWNTs

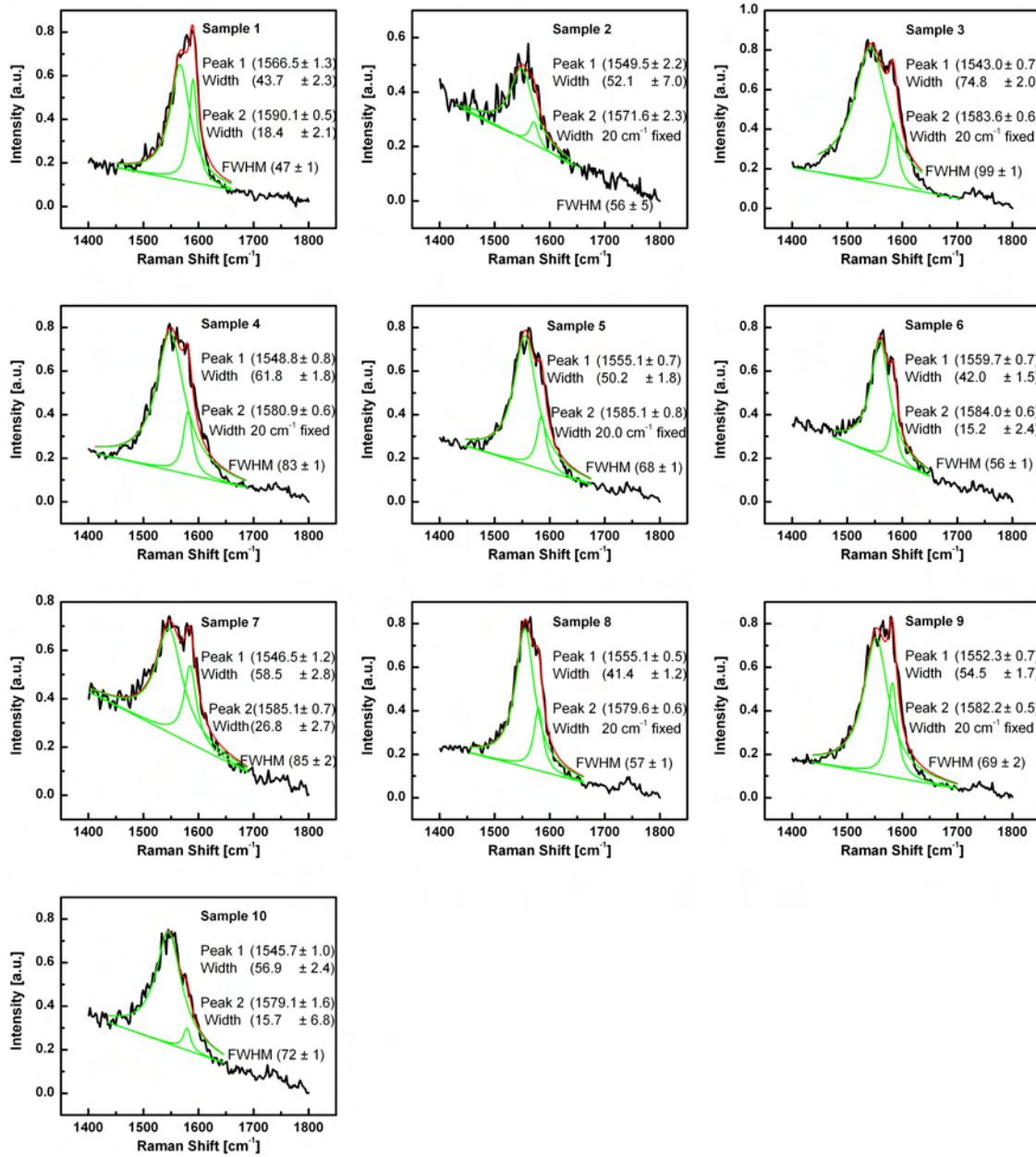


Figure 4.7.: G mode analysis of the individual metallic SWNTs shown in Fig. 4.6. The data has been fitted with two Lorentzian type components G^+ and G^- after background subtraction. Lorentzian curves and linear background are indicated in green and their sum is indicated in red as the least squares fit. Positions and widths of the peaks as well as the FWHM of the G bands are in cm^{-1} units. Note that in cases where the double peak structure was not resolved, the G^+ width was taken as 20 cm^{-1} and the G^- and positions were left as free parameters. Sample numbering relates to Table 4.1.

4. Results and discussion

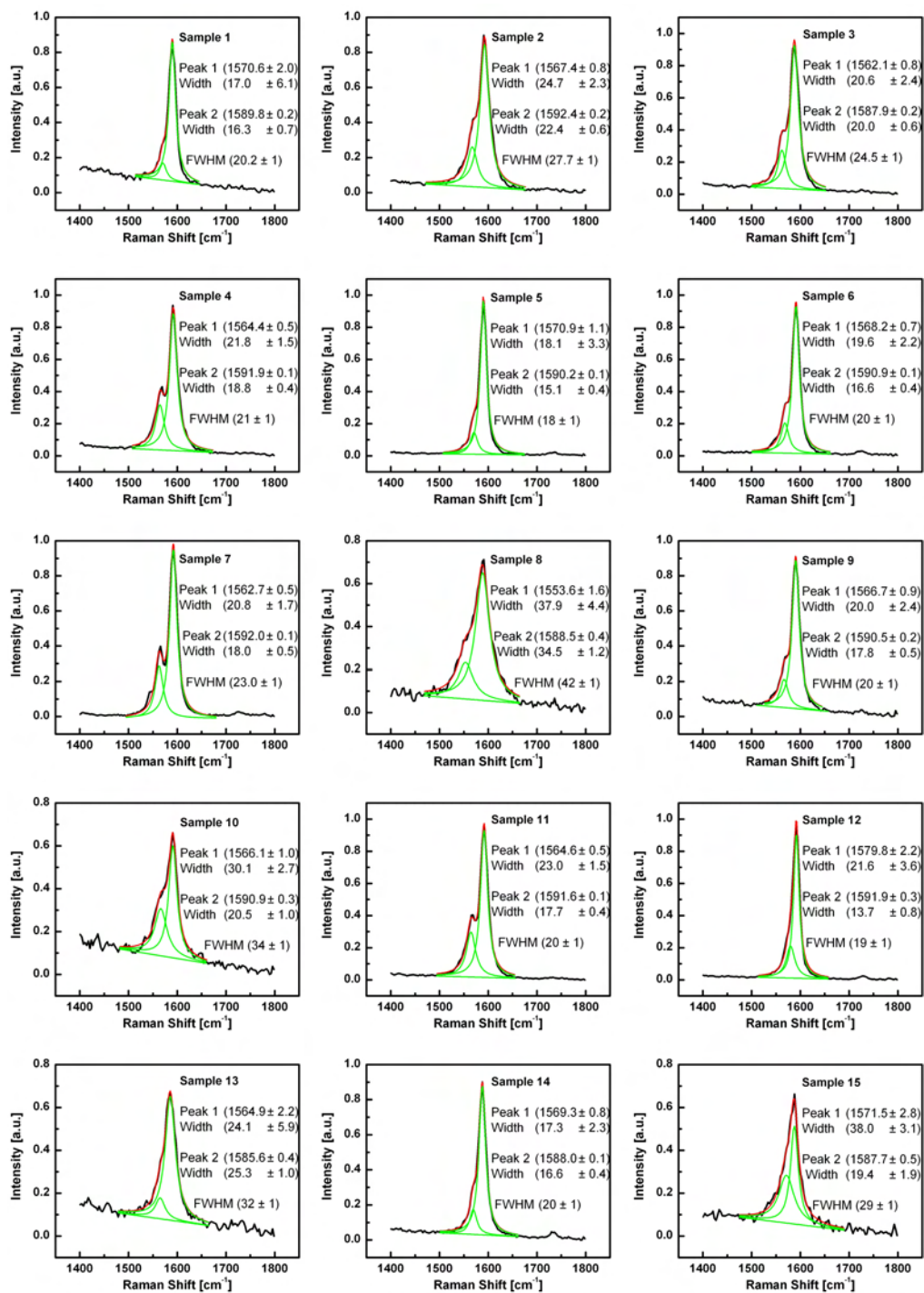


Figure 4.8.: G mode analysis of the individual semiconducting SWNTs shown in Fig. 4.6. For fitting procedure see caption of Fig. 4.7. Sample numbering relates to Table 4.2.

which states that the broadening is due to a phonon-plasmon interaction mechanism that causes the downshift and line-shape of metallic bulk samples, seems not to apply on the level of individual metallic SWNTs. The broad Lorentzian-type line shape of the G^- peak rather points to an electron-phonon coupling mechanism, where the LO mode couples strongly to the electronic system and thus possesses a shorter lifetime.

From the G mode line-shape for individual metallic SWNTs we conclude on the basis of our combined Raman and transport measurements, that it is possible to identify and discriminate individual metallic and semiconducting SWNTs. This conclusion is based on the width of the lower-energy G mode, ΔG^- , as demonstrated in Fig. 4.9. For individual metallic SWNTs the ΔG^- ranges between 40-60 cm^{-1} and between 20-30 cm^{-1} for semiconducting SWNTs (the majority of the latter however displays ΔG^- around 20 cm^{-1}). Taking into account the spectral resolution of 6 cm^{-1} , we derive 34-54 and 14 cm^{-1} for the intrinsic line width of the lower-energy G mode of metallic and semiconducting tubes, respectively. In addition, only a weak diameter dependence of ΔG^- is observed with our accessible diameter range. In contrast, after this part of the thesis was completed, Lazzeri *et al.* [58] have published a similar plot presenting a strong dependence of the ΔG^- on diameter. However, this was given over a much larger diameter range. Their plot (Fig. 4.10) displays data from various experiments of different groups that were obtained from nanotubes of different sources and diameters. Accordingly, all data points in one plot, including those of Fig. 4.9, gave a much larger diameter range and thus the dependency could more easily be recovered.

The theoretical argument for our proposed electron-phonon coupling mechanism that results in a broadening of the G band in metallic SWNTs may be formulated as follows. The resolved phonon dispersion of graphite, and in particular the highest optical phonon branches, obtained by high precision inelastic x-ray scattering experiments on a graphite single crystal [86] first led to the proposal of strong electron-phonon coupling by Piscanec *et al.* [84]. Based on the phonon dispersion, the strong electron-phonon coupling in graphite occurs with the Γ - E_{2g} and the K - A'_1 modes (appendix A), as at the Γ and K point-symmetries the phonon dispersion reveals an unusual behavior, which is a signature of a Kohn anomaly, as confirmed by the sharp kinks in the phonon dispersion (Fig. E.1 in appendix E).

After the realization of the strong electron-phonon coupling in graphite, Lazzeri *et al.* [58] have further demonstrated theoretically that electron-phonon coupling

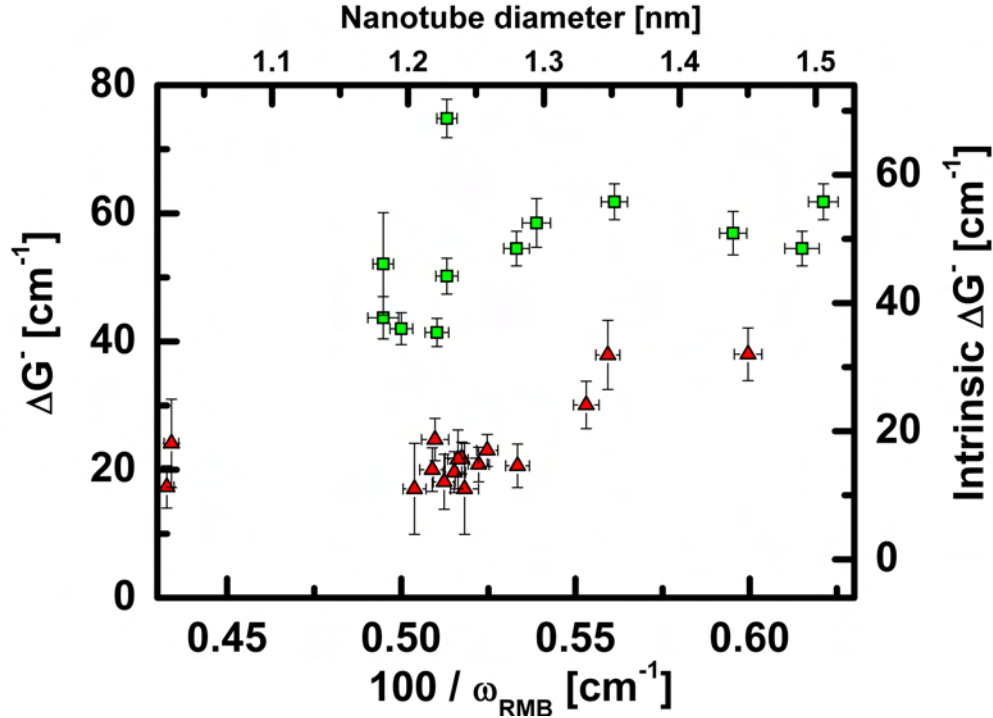


Figure 4.9.: Width of the G^- peaks from Fig. 4.6. ΔG^- plotted *versus* the inverse measured RBM frequency ω_{RBM} . ΔG^- for individual metallic SWNTs (green squares) is significantly larger than for individual semiconducting SWNTs (red triangles). Intrinsic ΔG^- denotes the values corrected for the spectral resolution. A weak diameter dependence is observed.

processes are the major cause for the broadening of both the G peak in graphite and the G^- peak in metallic SWNTs. Their explanation was based on the possible sources for peak broadening. Briefly, each phonon linewidth (γ) in a perfect crystal is the product of two interactions: (1) electron-phonon interactions and (2) phonon-phonon interactions. Therefore, a phonon linewidth is given by $\gamma = \gamma_{q\eta}^{\text{EPC}} + \gamma^{\text{an}}$, where $\gamma_{q\eta}^{\text{EPC}}$ stands for the electron-phonon interactions where q and η are the phonon wave vector and phonon branch, respectively, and γ^{an} stands for anharmonic phonon-phonon interactions. It is worth noting that the contribution to the linewidth due to *electron-phonon interactions occurs only in zero gap electronic systems*. Regarding the G peak in graphite, its anharmonic contribution to the peak broadening is negligible, and therefore one can determine the electron phonon coupling matrix element directly from the width of the peak. As mentioned in footnote 11 of section 2, the single G peak of graphite originates from the Γ - E_{2g} mode. A Raman spectrum was measured from a perfect (no disorder D-peak) single crystal of graphite. The value

obtained for the FWHM of the G peak was $\gamma_G = 13 \text{ cm}^{-1}$, at a spectral resolution of $\sim 1.5 \text{ cm}^{-1}$. As the anharmonic contribution was taken to be smaller than the spectral resolution, $\gamma_G^{\text{an}} < 1.5 \text{ cm}^{-1}$, the intrinsic electron-phonon interactions term could be estimated as $\gamma_\Gamma^{\text{EPC}} \sim 11.5 \text{ cm}^{-1}$. This estimation for graphite agreed nicely with Piscanec's *et al.* [84] and Lazzeri's *et al.* [58] calculations. Their main conclusions are given below.

The linewidths of both Γ -LO and Γ -TO modes in graphite were given by:

$$\gamma_\Gamma^{\text{EPC}} = \frac{\sqrt{3}a_0^2\hbar^2}{4M\beta^2}\langle D_\Gamma^2 \rangle_{\text{F}} \quad (4.1)$$

with $a_0 = 2.46 \text{ \AA}$, $\beta = 5.52 \text{ \AA eV}$ the slope of the π electronic bands near E_{F} , M the atomic mass of carbon and $\langle D_\Gamma^2 \rangle_{\text{F}}$ the electron-phonon coupling matrix element. Equation 4.1 can provide the value of $\langle D_\Gamma^2 \rangle_{\text{F}}$ directly if $\gamma_\Gamma^{\text{EPC}}$ is known. Substituting the value obtained above for graphite ($\gamma_\Gamma^{\text{EPC}} \sim 11.5 \text{ cm}^{-1}$) the electron-phonon coupling matrix element reads $\langle D_\Gamma^2 \rangle_{\text{F}} \sim 47 \text{ (eV/\AA)}^2$. This value compares very well with previous density functional theory (DFT) calculations $\langle D_\Gamma^2 \rangle_{\text{F}} = 45.6 \text{ (eV/\AA)}^2$ for both Γ -LO and Γ -TO modes, confirming that the anharmonic contribution γ_G^{an} is indeed small [84]. In the case of graphite, Piscanec and Lazzeri *et al.* [58,84] have also demonstrated how the dispersion itself can give a direct measure for $\langle D_\Gamma^2 \rangle_{\text{F}}$, which again agreed nicely with the value obtained from DFT calculations. This is briefly discussed in appendix E as it relates to the Kohn anomalies in the graphite phonon dispersion for the Γ -E_{2g} and K-A₁' modes.

Our and other groups' experimental findings of broad G⁻ peak for individual metallic SWNTs have encouraged further theoretical calculations by Lazzeri *et al.* [58] that could be supported by the available experimental data. They have computed the phonon frequencies for several metallic SWNTs, where based on these calculations, all metallic SWNTs of any chirality displayed a splitting of the corresponding Γ -E_{2g} mode in graphite into the TO and LO modes in SWNTs. Both calculations and the experimental findings from the various groups [48,52,85,87,88] present a lower frequency for the LO mode with a strong diameter dependence. Figure 4.10 illustrates this behavior, which contradicts what has been originally proposed in previous publications, *e.g.*, [57,87,89] claiming a strong diameter dependence for the TO mode instead. Further, Lazzeri *et al.* [58] stressed that such a counter intuitive behavior can only be understood if one assumes the presence of a Kohn anomaly

4. Results and discussion

in the phonon dispersion of metallic SWNTs as was demonstrated for the graphite dispersion [84]. In general, a Kohn anomaly lowers the frequency of phonons having significant interactions with electrons. Accordingly, the LO mode couples to electrons while the TO mode does not, as was indicated in section 2.4.5. The interaction of the LO phonon with the electronic system opens a small energy-gap, while its oscillation lowers the frequency of the LO mode compared to graphite and semi-conducting SWNTs, in a manner resembling a "temporary" Peierls distortion [50]. Thus, the LO mode frequency (ω_{LO}) is smaller than the frequency of the TO mode (ω_{TO}), and was accordingly assigned to the G^- peak, while the G^+ was assigned to the TO tangential mode. Figure 4.10 compares the DFT calculations with various experimental findings, where the agreement seems to be very good without any fitting parameters. Nevertheless, only the data points delivered as part of this thesis by Oron-Carl *et al.* [52] were double checked by electrical transport measurements, confirming an I_{SD} current independent of gate voltage. Lazzeri *et al.* [33, 58] have in addition produced an expression for the FWHM of the G^+ and G^- peaks linewidths ($\gamma_{\Gamma-\text{LO}}^{\text{EPC}}$ and $\gamma_{\Gamma-\text{TO}}^{\text{EPC}}$) *i.e.*, the contribution of each electron-phonon (LO and TO) interactions to the linewidth in relation to the tube diameter d and to the term $\langle D_{\Gamma}^2 \rangle_{\text{F}}$:

$$\gamma_{\Gamma-\text{LO}}^{\text{EPC}} = \frac{2\sqrt{3}\hbar^2 a_0^2 \langle D_{\Gamma}^2 \rangle_{\text{F}}}{\pi M \hbar \omega_{\Gamma} \beta} \frac{1}{d} \quad \text{and} \quad \gamma_{\Gamma-\text{TO}}^{\text{EPC}} = 0 \quad (4.2)$$

with $\hbar\omega_{\Gamma} = 196$ meV and all other parameters are the same as given above. The left equation is valid for SWNTs with $d \geq 0.8$ nm as mostly used in experiments and device fabrication. The main conclusion from the linewidth expressions in Eq. 4.2 is that only electron-phonon interactions which involve the LO mode contribute to the linewidth in metallic SWNTs. For semiconducting SWNTs, however, the contribution is zero from both the TO and LO modes.

Looking back at Figs. 4.8 and 4.9 and Table 4.2, the G^+ and G^- linewidths in the case of semiconducting SWNTs are similar, ~ 20 cm^{-1} and $\sim 20 - 30$ cm^{-1} , respectively. These experimental results display a small broadening greater than theoretically expected [58] which results from our spectral resolution of 6 cm^{-1} , so that the high and low energy Raman modes (RBM and G band) could be measured simultaneously. In the case of metallic SWNTs, the observed G^+ linewidth is the same as for semiconducting (~ 20 cm^{-1} , Fig. 4.7) and broader for the G^- mode $\sim 40 - 60$ cm^{-1} (Fig. 4.9 and Table 4.1). The large γ_{G^-} of the metallic SWNTs

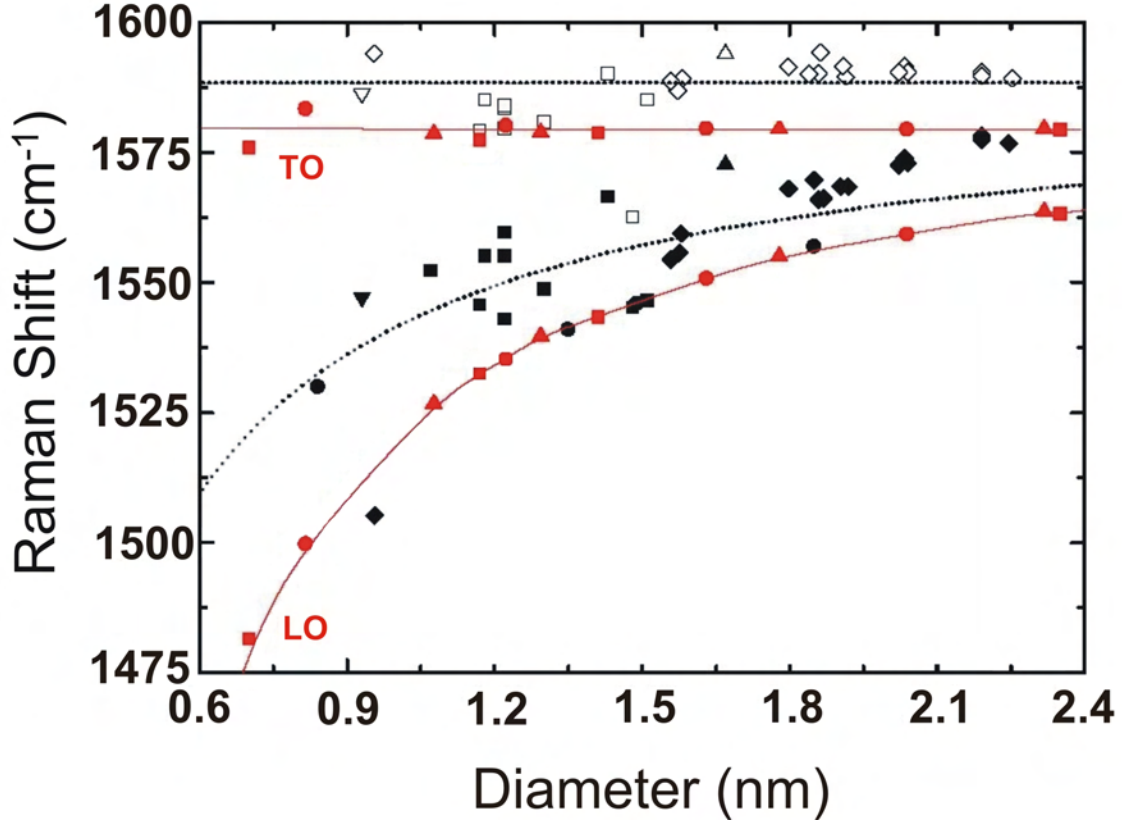


Figure 4.10.: Experimental (black) and calculated (red) data for the G^+ and G^- modes in metallic SWNTs. The experimental findings are indicated (G^- , G^+): Oron-Carl *et al.* [52] (\blacksquare , \square) Brown *et al.* [85] (\bullet , \circ) Jorio *et al.* [87] (\blacklozenge , \diamond) Maultzsch *et al.* [48] (\blacktriangledown , \triangledown) Doorn *et al.* [88] (\blacktriangle , \triangle). The DFT symbols are for armchair tubes (\bullet , \circ), for zig-zag tubes (\blacksquare , \square) and for chiral tubes (\blacktriangle , \triangle). The DFT data points are for armchair [from (3,3) to (18,18)], zigzag [from (9,0) to (30,0)] and chiral tubes [(5,2), (12,3), (16,1), (16,10), (20,14)]. The lines are a fit to the experimental and DFT data. Taken from Ref. [58].

results from the large $\gamma_{\Gamma-LO}^{EPC}$ linewidth whereas the small γ_{G^+} linewidth is due to the negligible anharmonic contribution¹.

The predicted $1/d$ dependence of the γ_{G^-} linewidth in metallic SWNTs given in Eq. 4.2 is demonstrated in Fig. 4 of Ref. [58]. The observed dependence again includes our experimental data and displays the γ_{G^-} values of metallic SWNTs *versus* diameter. The term $\langle D_{\Gamma}^2 \rangle_F$ in Eq. 4.2 was found by a fit to the experimental γ_{G^-} values, where the obtained value again agrees well with the DFT calculations [58].

¹Heating effects can cause an increase of $\sim 15 \text{ cm}^{-1}$ for both G^+ and G^- linewidths of metallic and semiconducting SWNTs as observed by Jorio *et al.* [87] and Scardaci *et al.* [90] for the temperature range of 80-600K [58].

This shows that the electron-phonon coupling matrix element for metallic SWNTs can be obtained by folding the one of graphene as demonstrated by the calculations of Lazzeri *et al.* [58].

4.6. Simultaneous electrical and resonance Raman scattering measurements

The strong C-C bond in metallic SWNTs is associated with their ability to carry very high current densities before failure ($\sim 10^9$ A/cm²) as compared to other metallic substances like Copper ($\sim 10^7$ A/cm²). Due to their quasi-ballistic electron transport on the μm scale, metallic SWNTs may be envisioned as good candidates for interconnectors in electrical circuits. However, high-field electrical measurements, including our own (section 4.6.3) indicate that various electron-phonon coupling processes may limit their ballistic behavior. The ballistic transport was shown possible up to more than a micron in the low-bias regime (~ 1.6 μm) while the electron mean-free path dropped significantly at the high-bias regime ($\sim 10 - 15$ nm) [9–11]. Strong electron-phonon coupling processes were already confirmed by Raman experiments (sections 4.3 and 4.5) for non-biased SWNTs. The analogous process of phonon generation during high-field electron transport could be easily detected by Raman scattering experiments as well. Here, we provide a complementary study of *simultaneous electrical and Raman measurements on individual SWNTs*. The idea was that a bias should increase electron-phonon coupling processes in a metallic nanotube, if the proposed mechanism is indeed correct. As the occupation of a specific phonon can be determined from the ratio of the Stokes and anti-Stokes peak intensities, a monotonic growth of this ratio may provide a straightforward proof for an increase in its occupation, *i.e.*, an increase in relaxation processes via electron-phonon interactions. In this thesis, preliminary results in monitoring high-energy phonon occupations by simultaneous electrical and Raman measurements are reported. These have already encouraged collaborating theoreticians to find a theoretical explanation. The optical high-energy phonons' effective-temperature was predicted as high as thousands of Kelvins by Lazzeri *et al.* [33]. Our objective was to test the strong electron-phonon coupling relaxation processes apparently occurring in metallic SWNTs and to further verify the predicted high effective-temperatures via the analysis of Raman spectra obtained from our biased metallic SWNTs. A

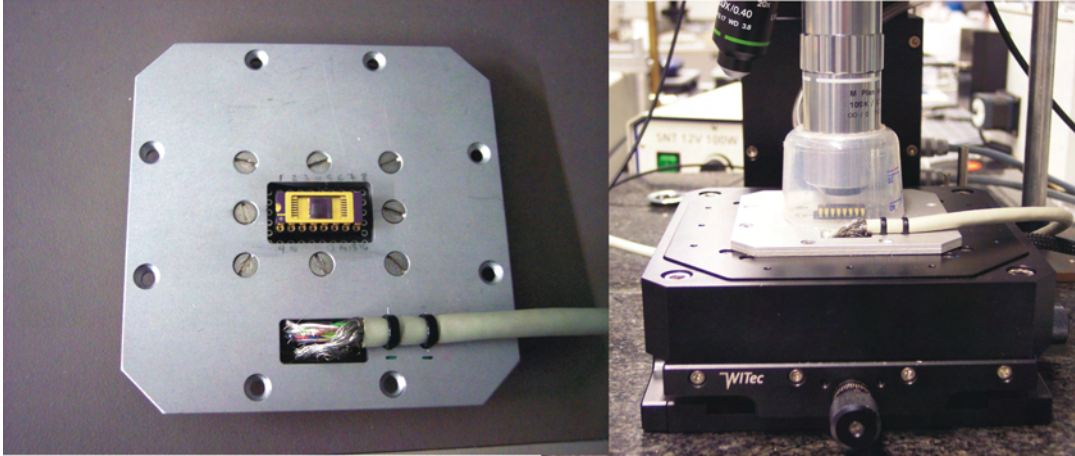


Figure 4.11.: A top view of the metal plate with its integrated socket and chip carrier is shown on the left. On the right, a long working distance objective with a surrounding plastic cover to keep the sample under Ar atmosphere is shown.

suitable device was therefore adapted on the piezo table of our Raman setup so as to collect spectra from electrically biased SWNTs.

4.6.1. The setup for simultaneous electrical and Raman measurements

In order to perform simultaneous electrical and Raman measurements, a metal plate was mounted on top of the piezo table of the Raman setup with an integrated socket of 16 legs that can hold a chip carrier. An electric cable connects the socket to a box possessing 16 channels. As one channel is required for the grounded drain electrode, if no gate voltage is applied, 15 channels are available as source electrodes from the same chip. A top view of the plate with its integrated socket is shown on the left side of Fig. 4.11, and a side view of the long working distance objective used for Raman spectroscopy ($WD=10$ mm, $N_A=0.7$, $M=100x$) and surrounded by a plastic cover is shown on the right. The long WD objective was required since the objective normally used ($WD=2.8$ mm, $N_A=0.9$ $M=100x$) could not reach close enough to the sample. The plastic cover was required in order to protect the sample from possible oxidation processes while biasing the tube [91]. This was realized by a constant Ar flow above the sample, which pressurizes the volume within the plastic cover thus effectively removing the air atmosphere from the surroundings of the sample and replacing it by Ar. Figure 4.12 shows both the electrical (left) and

4. Results and discussion

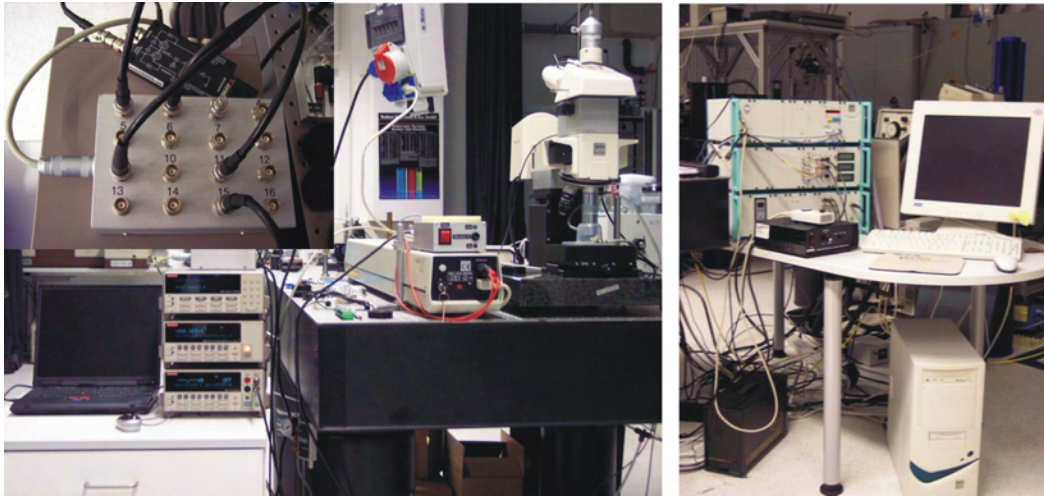


Figure 4.12.: The electrical and Raman parts of the setup used for simultaneous measurements. Source meters, channel boxes, He/Ne laser, confocal Raman microscope and electronics are shown. See text for details.

Raman (right) parts of the setup used. Two Keithley source meters which control the V_{SD} and the V_G , as well as a Keithley channel control are shown. The channel control is connected to the home made channel box built for these measurements (inset). Coaxial cables connect the ports of the Keithley and home made boxes, both provide 16 channels, while a Lab View program controls the whole electrical setup. The Raman microscope (CRM 200) is shown to the right side of the electrical setup as well as a He/Ne laser generating photons at 632.82 nm wavelength. On the right side of Fig. 4.12 the electronics controlling the spectrometer, detector (CCD camera), video camera and piezo table are shown next to the Raman computer.

4.6.2. Phonons' effective-temperature

Since phonons are bosons, their occupation number n , required in deriving the effective-temperature of a specific phonon, is given in equilibrium by the Bose-Einstein occupation factor:

$$n = \frac{1}{\exp\left(\frac{\hbar\omega_{\text{ph}}}{k_B T}\right) - 1} \quad (4.3)$$

with the Boltzmann constant k_B and the phonon energy $\hbar\omega_{\text{ph}}$ [92]. The occupation number is correlated to the Stokes and anti-Stokes peak intensities via the following

4.6. Simultaneous electrical and resonance Raman scattering measurements

relation:

$$\frac{I_S}{I_{AS}} = \frac{n+1}{n} \quad (4.4)$$

Rearranging Eq. 4.4 and substituting Eq. 4.3 yields:

$$n = \frac{1}{\frac{I_S}{I_{AS}} - 1} = \frac{1}{\exp\left(\frac{\hbar\omega_{ph}}{k_B T}\right) - 1} \quad (4.5)$$

and thus

$$\frac{I_{AS}}{I_S} = \exp\left(-\frac{E_{ph}}{k_B T}\right) \quad (4.6)$$

where $E_{ph} = \hbar\omega_{ph}$ is the phonon energy. Equations 4.4 and 4.6 therefore provide a measure for the occupation and effective-temperature of a particular phonon.

Figure 4.13 shows both the Stokes and anti-Stokes Raman peaks of the biased metallic SWNT shown in the inset. It seems that the contact in the tube-on-metal configuration may in fact contain two tubes. However, according to the I - V_{SD} given in Fig. 4.15, which shows the magnitude of current passing through the contact ($\sim 16 \mu\text{A}$), it could also be that the electrical transport corresponds to only one of the tubes. This may occur if for example one of the tubes is a semiconducting tube, or alternatively one tube does not carry any current because it is not contacted or interrupted.

The spectra of Fig. 4.13 are vertically shifted as to highlight the evolution of the Stokes and anti-Stokes G peaks, located to the right (left) of the elastically scattered Rayleigh light. The Stokes peaks of the RBM mode are harder to resolve in Fig. 4.13 because we wished to study the high-energy phonons that correspond to the G Stokes and anti-Stokes modes at the cost of lower spectral resolution. It is clear from Fig. 4.13 that the anti-Stokes G peaks intensity I_{AS}^G grows as the bias applied on the tube increases, *i.e.*, the phonon occupation grows. This growth could be the result of relaxation processes, *i.e.*, electrons are accelerated and relax under the emission of high-energy phonons, or simply be the result of a heating process, as the passing current heats the tube even more than the heating caused by the laser.

To exclude any thermal effects one must assure that the FWHM and the position of the Stokes peaks do not change at the different applied biases. This is required for assuring that a hyper-thermal effect rather than just a heating effect occurs in the nanotube. On the anti-Stokes side it is seen that the RBM mode intensity I_{AS}^{RBM}

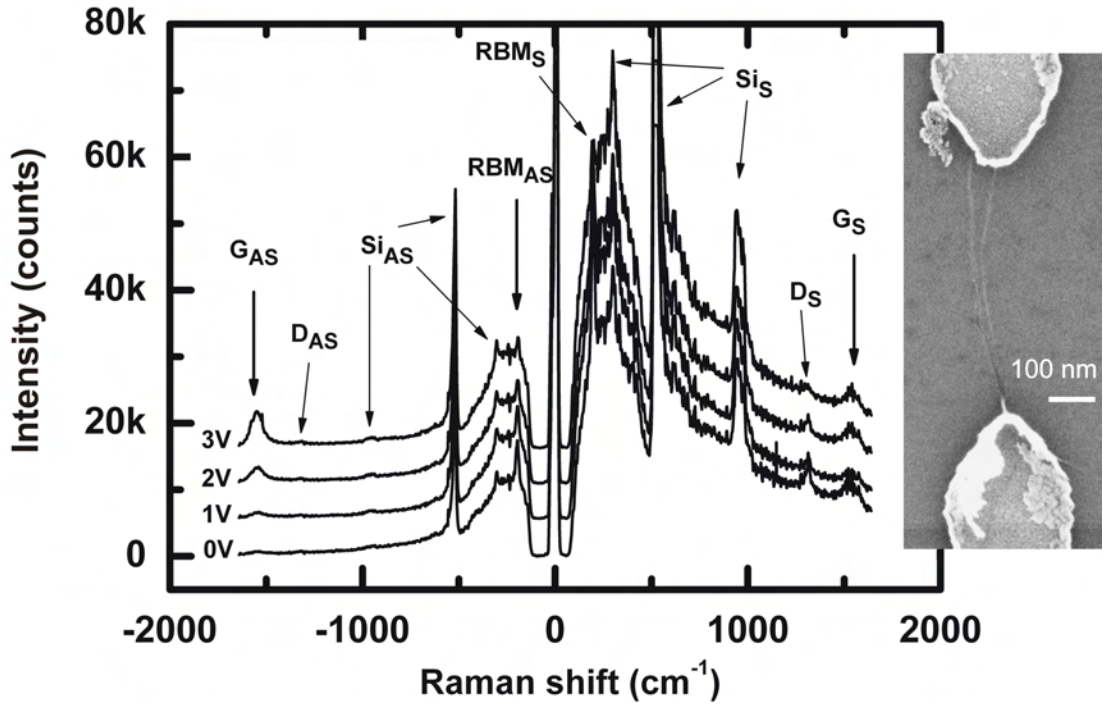


Figure 4.13.: The Raman spectra of a biased metallic SWNT at the source-drain voltages, $V_{SD} = 0, 1, 2$ and $3V$. The various Stokes (S) and anti-Stokes (AS) peaks originating from the tube and Si are indicated. The peak position of the RBM_S is 197.8 cm^{-1} . Its FWHM is $\sim 23 \text{ cm}^{-1}$. The G_S peak is centered at about 1530 cm^{-1} where its FWHM is about 60 cm^{-1} . The spectra are shifted vertically to follow the evolution of the G mode peaks intensity. Accumulation times of all spectra are 90 sec. (Right) SEM image of the biased metallic SWNT(s). Sample w129c123p2a.

changes with bias. As this mode is much lower in energy compared to the G mode, its intensity can be easily affected by the bias, *i.e.*, even a very small temperature increase can significantly change the mode intensity. However, position (197.8 cm^{-1}) and FWHM ($\sim 23 \text{ cm}^{-1}$) are the same for all four spectra. The high value obtained for its FWHM may suggest that more than one tube was detected. It may be that the tubes have similar diameter and thus the peak appears broader. Regarding the Stokes G mode, it reveals a broad peak as expected from a metallic SWNT. Its FWHM was measured to be about 60 cm^{-1} at all voltages applied.

To further assure that the Si/SiO₂ substrate remains at room-temperature, one needs to check its peak intensities at the different applied biases. The intensities of the first order Si peak at 521 cm^{-1} were found constant throughout all the experiments.

4.6. Simultaneous electrical and resonance Raman scattering measurements

As postulated in Eq. 4.6 the intensities of the Raman Stokes and anti-Stokes peaks can provide a measure for the phonons' effective-temperature. We first calculate the value for both RBM and G modes at 3V. We use the measured intensity ratios and the corresponding energies of the modes in a rearranged expression of Eq. 4.6:

$$T_{\text{eff}} = -\frac{E_{\text{ph}} \cdot e}{k_{\text{B}}} \ln \left(\frac{I_{\text{AS}}}{I_{\text{S}}} \right)^{-1} \quad (4.7)$$

with $E_{\text{ph}}^{\text{G}} \simeq 196$ meV, $E_{\text{ph}}^{\text{RBM}} \simeq 25$ meV and $k_{\text{B}} = 1.38 \cdot 10^{-23}$ J/K it follows that:

$$T_{\text{eff}}^{\text{G}} = -\frac{0.196 \cdot 1.602 \cdot 10^{-19}}{1.38 \cdot 10^{-23}} \ln (1.47)^{-1} \approx -5,900\text{K} \quad (4.8)$$

$$T_{\text{eff}}^{\text{RBM}} = -\frac{0.025 \cdot 1.602 \cdot 10^{-19}}{1.38 \cdot 10^{-23}} \ln (0.308)^{-1} \approx 246\text{K} \quad (4.9)$$

where the measured intensity ratios at 3V are 1.47 and 0.308 for the G and the RBM modes, respectively. The effective-temperature values obtained via Eqs. 4.8 and 4.9 immediately suggest that the model given in Eq. 4.7 is wrong. The intensity ratio value found for the G mode at 3V is > 1 . This contradicts the expression given in Eq. 4.4 defining the relation between the Stokes and anti-Stokes intensities ratio and the occupation number n . Following this relation, the $I_{\text{AS}}/I_{\text{S}}$ ratio value must be limited between 0 and 1. Furthermore, one must recall that the detected modes result from resonant processes occurring in a carbon nanotube. Even though both resonant and non-resonant processes occur, only the resonant ones are observed. To account for the enhancement/reduction occurring by the resonant processes, one needs to compare the theoretical (taking $T=300\text{K}$) and experimental ratios at 0V:

$$\left(\frac{I_{\text{AS}}}{I_{\text{S}}} \right)_{\text{G}}^{\text{theo}} \cong 5 \cdot 10^{-4} \quad \left(\frac{I_{\text{AS}}}{I_{\text{S}}} \right)_{\text{G}}^{\text{exp}} \cong 0.11 \quad (4.10)$$

The difference in the values given in Eq. 4.10 suggests that the anti-Stokes peak of the G mode is seen at zero bias *only* due to a resonant enhancement (of ~ 220 times). Thus, one can derive an expression which directly accounts for the resonant enhancement, namely to the normalization with respect to the 0V peak intensity. The enhancement/reduction pre-factor C is assumed voltage-independent and the ratios

4. Results and discussion

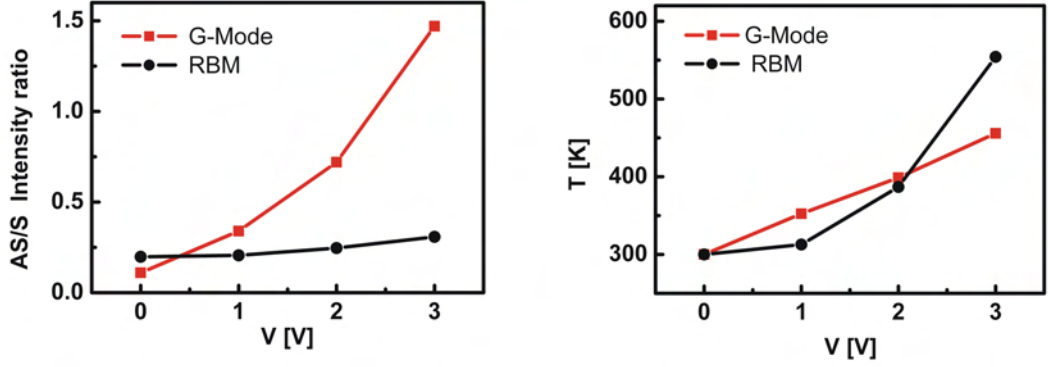


Figure 4.14.: Measured AS/S intensity ratios and calculated effective-temperatures *versus* applied voltage for both RBM and G modes. The intensity data points were obtained by the peak area after baseline subtraction. The error bars in temperature are $\pm 1\text{-}2\text{K}$ and therefore are not displayed. Sample w129c123p2a.

at room-temperature (T_1) and at some elevated temperature (T_2) are given by:

$$\frac{I_{AS}}{I_S}(T_1) = C \cdot \exp\left(-\frac{E_{ph}}{k_B T_1}\right) \quad \text{and} \quad \frac{I_{AS}}{I_S}(T_2) = C \cdot \exp\left(-\frac{E_{ph}}{k_B T_2}\right) \quad (4.11)$$

where a division between both expressions yields the effective-temperature T_2 :

$$T_2 = \frac{T_1}{1 - \frac{k_B T_1}{E_{ph}} \ln\left(\frac{R_2}{R_1}\right)} \quad (4.12)$$

The experimental ratios for the G mode are $R_1 = \frac{I_{AS}}{I_S}(T_1) = 0.11$ and $R_2 = \frac{I_{AS}}{I_S}(T_2) = 1.47$ at 0 and 3V, respectively, where $R_1 = 0.198$ and $R_2 = 0.308$ are the measured ratios at zero and 3V for the RBM mode. The effective-temperatures for both RBM and G modes are then obtained by substituting the relevant parameters in Eq. 4.12 (taking $T_1 = 300\text{K}$), yielding $T_2^G \approx 456\text{K}$ and $T_2^{\text{RBM}} \approx 552\text{K}$.

The measured AS/S intensity ratios and calculated effective-temperatures for the RBM and G modes of the biased tube in Fig. 4.13 are plotted *versus* the applied voltages in Fig. 4.14. The AS/S ratio of the G mode seems to vary more than that of the RBM mode. In contrast, the effective-temperature of the RBM mode shows to be slightly more affected by the bias as compared to the G mode. One explanation for the effective-temperature increase could be a heating effect where the nanotube simply heats up with voltage. As the energy of the RBM mode is comparable to the thermal energy, it could be that due to a heating effect, more

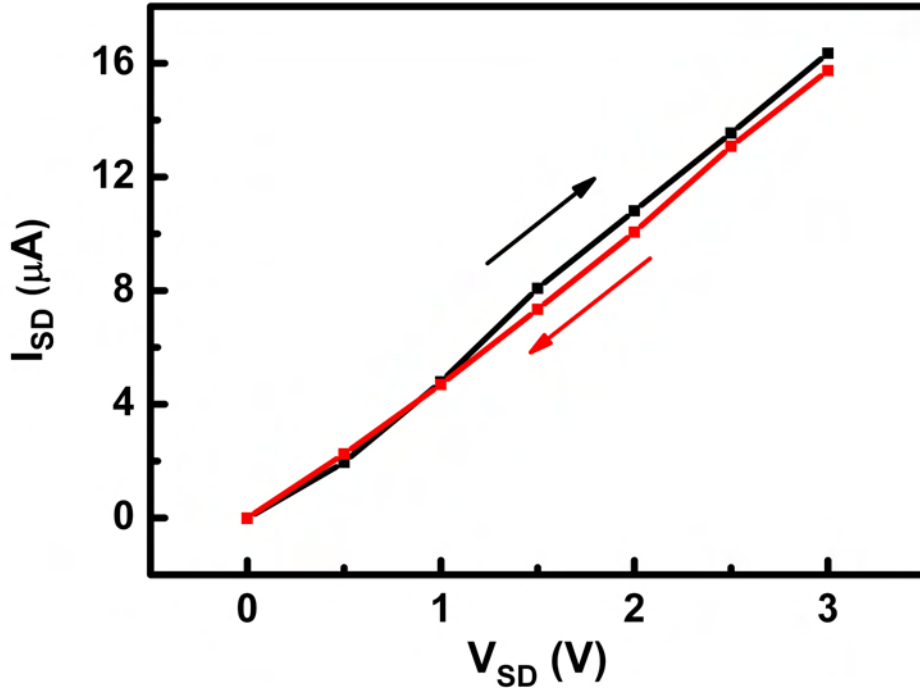


Figure 4.15.: I - V_{SD} curves from a biased SWNT in the tube-on-metal configuration. The curves relate to the metallic SWNT (inset of Fig. 4.13, w129c123p2a) detected by the Raman measurements at different voltages. Up (black) and down (red) cycles are displayed.

RBM phonons are created in the nanotube together with other non-Raman active low-energy phonons (*e.g.*, twiston). The temperature growth could in contrast imply an increase of electron-phonon coupling processes due to the induced bias. Yet, even though an increase in the AS/S ratio of the G mode with bias is revealed, its effective-temperature only moderately increases (from 300 to 456K)². It is further not clear if the phonon emission by the electrons occurs as a result of their acceleration along the tube, and thus phonons could be generated at any point along the tube or is it the case in which phonons can be emitted already at the contact, providing that the electrons have the required energy. The issue may be further elucidated by looking at the I - V_{SD} curve of the investigated metallic SWNT. Figure 4.15 displays the I - V_{SD} curves obtained from the electrical contact shown in the inset of

²We note that the model used for calculating the effective-temperatures assumes a voltage-independent resonant-factor C . It is however not clear if it changes with temperature.

4. Results and discussion

Fig. 4.13 with both up and down V_{SD} cycles. The curves are observed linear with a contact resistance of 187.5 k Ω . Their lack of slope change or current saturation may imply that the potential along the tube was smaller than 0.2 eV, as required for the emission of the high-energy G phonons, predicted by theory and other experimental findings [9–11]. In this case, it seems as if mostly RBM phonons were emitted by the accelerated electrons as the electrons could not attain the energy needed for the emission of high-energy phonons. Note that this interpretation implies that most of the potential drops across the contacts which is plausible given previous observations by other groups [93–96].

Another point to consider is that electrons may tunnel through high-resistance contacts into a SWNT device and be accelerated under the applied electric field. The displayed current should be lower as less electrons enter the tube, however, high-energy phonons emission should be still possible. Under these circumstances, it is conceivable that generated phonons are thermalized or not. If the phonons have a higher generation rate than relaxation rate, they could accumulate and display a high effective-temperature (see appendix F for hot phonons generation). Nevertheless, the predicted increase in phonon occupation (or effective-temperature) of particular high-energy phonons which preferably couple to the electronic system [33, 84] is not observed from our experimental data.

As the theoretically predicted high effective-temperature ($\sim 6000\text{K}$) could not be experimentally measured, it was initially believed that the absence of a saturated I - V_{SD} curve implies that no stimulated emission of high-energy phonons by accelerated electrons occurs because of high-contact resistances. We therefore next attempted to reduce the high-contact resistance. The idea was that low-contact resistances should allow higher potential along the tube and thus electrons could accelerate to higher energies. A higher potential should also bring the current to saturation, the point where ballistic behavior breaks down due to the emission of high-energy phonons by the accelerated electrons. By this scenario, one should expect higher AS/S intensity ratios, if the generated phonons are considered non-thermalized.

Given that lower contact resistances require a metal-on-tube configuration, a second lithography step was needed. New contacts with the metal-on-tube configuration were therefore produced, as well as a second metallization step realized on the con-

tact already analyzed in the above study (w129c123p2a). Surprisingly, no increase in intensity ratios, or alternatively, increase in effective-temperatures was achieved even though contact resistances were significantly improved, including the resistance of the contact studied in Fig. 4.13. In the next section we show the attempts to reach current saturation by reducing contact resistances via a second lithography step. Many of the new contacts were bridged by semiconducting SWNTs as the low-frequency dielectrophoretic technique was employed³. These tubes did not show current saturation and thus were not included further in the study.

We note that the detection of an anti-Stokes G peak at zero voltage was a rare event in the new metal-on-tube fabricated SWNT contacts. Most samples displayed a peak (if at all) only at some elevated bias. Some of these samples are shown in appendix G. This observation was also the case for the contact analyzed above (w129c123p2a) in Fig. 4.13 after the reduction of its contact resistance (measurements not shown in appendix G). One could speculate that a surface enhanced Raman effect was responsible for the initial high signal intensities coming from this contact. It may be that most of the original signal was in fact coming from the tube segment that was later covered by a second metal layer, thus showing much lower intensity of both Stokes and anti-Stokes peaks after the second lithography step.

4.6.3. Second lithography step: metal-on-tube

A significant improvement in contact resistance was achieved for devices in which a second metal layer was introduced on the initial contacts. Figure 4.16 shows a representative example of a SWNT that went through an extra lithography step (metallization) so as to achieve the metal-on-tube configuration. The SWNT edges are completely covered by the second Pd layer. This layer is about 1 μm wide to assure the full coverage of the first layer, *i.e.*, to account for any possible shifts in the lithography process. The sample is further annealed under vacuum at 500°C for one hour. Note that a new layout with well defined markers was required to achieve the perfect alignment presented in Fig. 4.16. The SWNTs for these devices were again provided by Frank Henrich, who initially dispersed the SWNTs in sodium cholate (appendix B) and later sorted them according to their length by a size exclusion

³Electron-phonon coupling processes can indeed occur in ON state semiconducting FETs as reported recently by Javey *et al.* [29]. The key point lies in device fabrication, namely the modulation of the Schottky barriers at the metal contacts.

4. Results and discussion

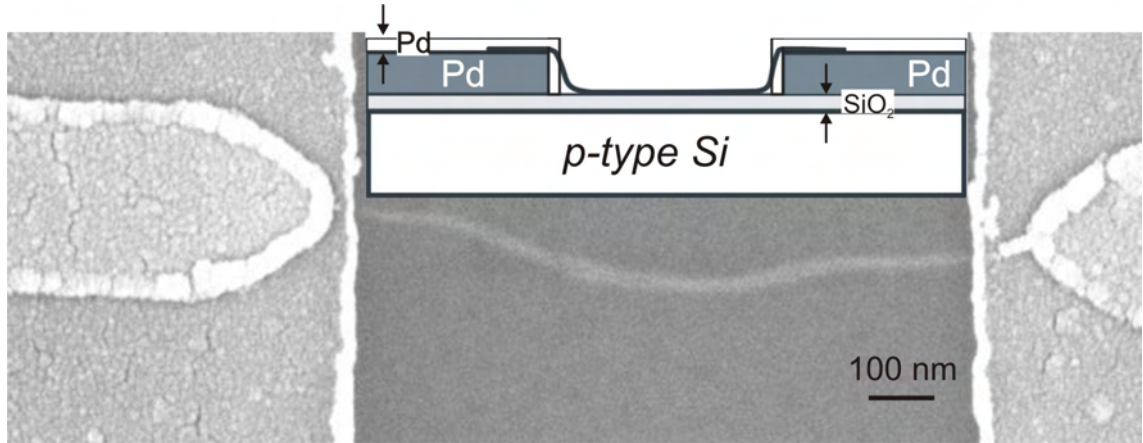


Figure 4.16.: 1 μm long SWNT in the metal-on-tube configuration. The second metal layer is approximately 20 nm thick. Pd was used in the first and second metallization steps. The scheme demonstrates a side view of the SEM image below. Note that the edges of the tube are perfectly covered by the metal. Sample w130c88p1c.

chromatography technique, adapted from Heller *et al.* [97]. It is worth mentioning that early extracted fractions were used. These SWNT suspensions contained a much higher content of long individual tubes (with 1-1.2 μm tube-length on average) as compared to the previously used centrifugated suspensions (with < 1 μm tube-length on average).

Devices similar to the one shown in Fig. 4.16 displayed much lower contact resistances (see Fig. 4.18). The improvement results from the fact that the edges of the tubes are surrounded by the electrode material and a bigger contact area is obtained between the electrode material and the tube. This metal-on-tube configuration causes a significant decrease of the tunnelling resistance. In addition, most samples started to show a deviation from linear behavior. The contact resistances of many such devices are summarized in Fig. 4.18. We recall from Eq. 2.21 that the total resistance is the sum of the resistances at the low and high bias regimes. The R_{low} results from the combination of contact resistance and the theoretical quantum resistance of a metallic tube. Figure 4.17 illustrates the way in which the R_{low} and the saturation current I_0 were obtained from the slopes of the I - V_{SD} curves. Note that even though the R_{low} should be voltage independent, it reveals a non-constant value as shown in the right part of Fig. 4.17. This may indicate a Luttinger liquid behavior however it may also simply occur due to a tunnelling barrier as discussed below. Many samples were analyzed in the same manner as indicated in Fig. 4.17.

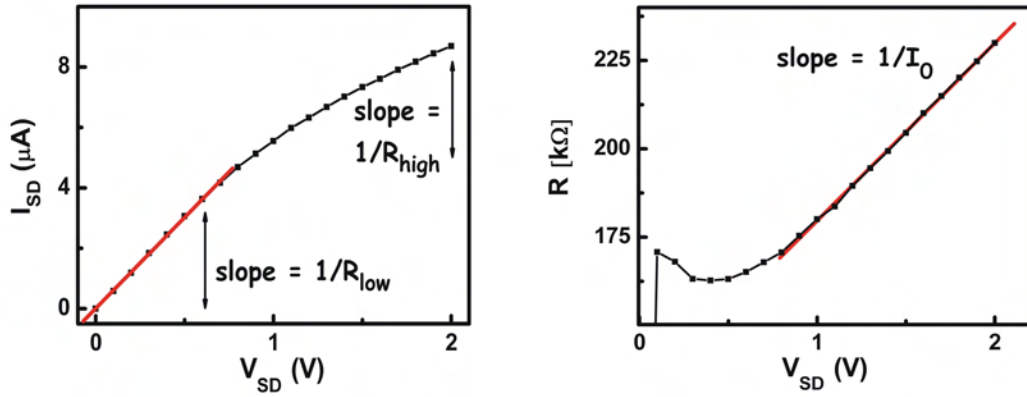


Figure 4.17.: (Left) An I - V_{SD} curve which shows a slope change as the current starts to saturate. (Right) I_0 derivation from a curve displaying the total resistance *versus* voltage. Linear fitting to the data is denoted in red. Sample w130c72p3a.

A summary of the saturation current *versus* contact resistance of various devices with different tube lengths and diameters is shown in Fig. 4.18. We note that the $0.5 \mu\text{m}$ long tubes were deposited from the decant portion of a centrifuged suspension rather than from a suspension obtained by the size exclusion technique. It seems that these samples possess small bundles rather than individual tubes. This observation is based on their current saturation magnitudes. In contrast, the SWNTs deposited from the size exclusion procedure reveal much lower saturation current and thus most likely are indeed individual tubes. They are highlighted by the horizontal dashed line denoting a current of $20 \mu\text{A}$. Note that theory predicts currents of 15 - $30 \mu\text{A}$ that can be carried by an individual metallic tube [9–11]. Resistances as low as ~ 39 and $\sim 45 \text{ k}\Omega$ were obtained for SWNT devices of 1.2 nm and 1 nm in diameter, respectively, denoted by vertical dotted lines. The contact resistances displayed in Fig. 4.18 illustrate a significant improvement with respect to those obtained from the tube-on-metal configured devices (Fig. 4.1). However, these results are still far from the theoretical quantum resistance value of $6.5 \text{ k}\Omega$ probably due to the continued presence of tunnelling barriers. The resistance magnitude of such barriers seems to depend strongly on the tube diameter used to fabricate the SWNT-device. Woong *et al.* [98], have reported recently on near-ohmic electrical contacts to metallic SWNTs with diameters bigger than 1.6 nm . They have shown that Pd or Rh contacts yield two-terminal resistance of $\sim 20 \text{ k}\Omega$ at room-temperature. For smaller diameters, $d \leq 1 \text{ nm}$ SWNTs, on the other hand, they have found much

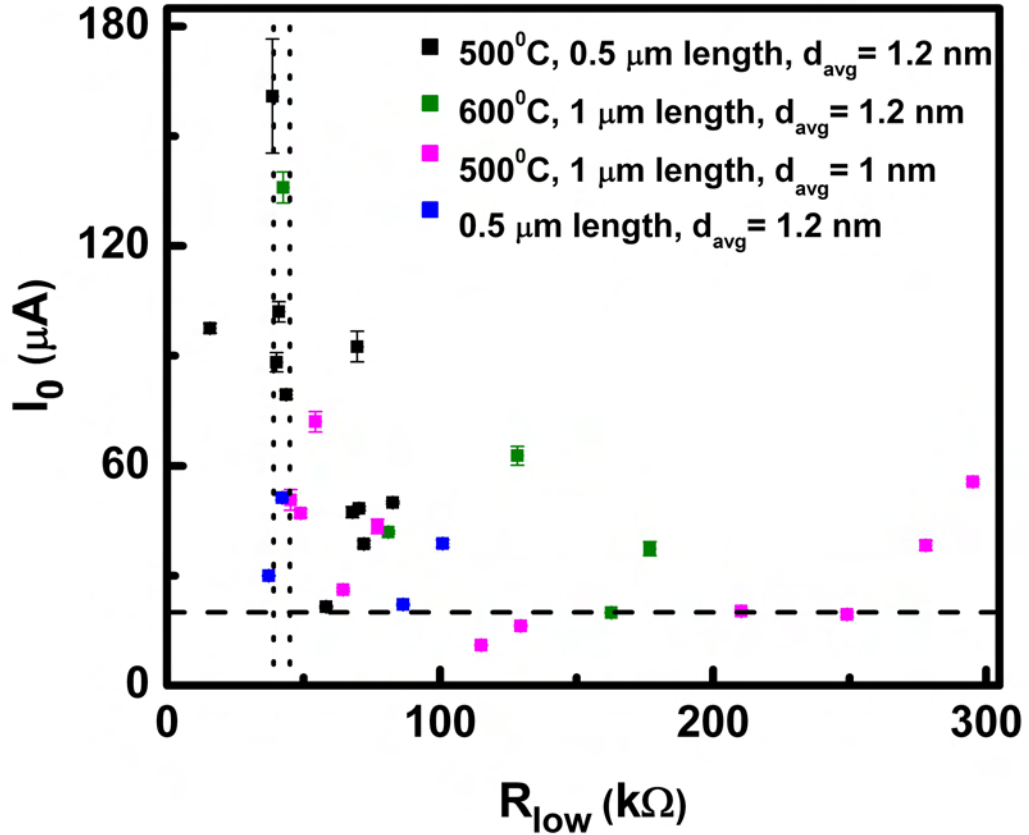


Figure 4.18.: A summary of current saturation I_0 versus R_{low} from various devices. The lengths, diameters and annealing temperatures are indicated. Data points from a few non-annealed devices are also shown (blue). Error bars in I_0 were determined from the fitting procedure described in Fig. 4.17. The two vertical lines denote the minimum R_{low} obtained for SWNTs of 1.2 nm and 1 nm average diameters. The R_{low} values are ~ 39 and ~ 45 k Ω , respectively.

higher resistances, on the order of hundreds of k Ω . These devices also displayed a non-linearity near zero bias, *i.e.*, a sign of a non-ohmic contacts due to tunnelling barriers. Looking back at Fig. 4.17, one sees that our sample, whose diameter is uncertain in a range between 1.0-1.5 nm, reveals a non-linearity near the zero bias. The behavior is hard to see from the I - V curve, however it is obvious from the right part of Fig. 4.17 where R_{low} appears voltage dependent in the range of $V_{\text{SD}} = 0$ -0.2V. Figure 4.18 additionally reveals that longer tubes have higher resistance values than shorter ones. It could be that the longer tubes have higher probability for scattering

centers (defects) that scatter electrons in the low-bias regime and in particular in the high-bias regime, where the electrons are additionally scattered inelastically under the emission of high-energy phonons.

Besides improving the contact resistances, the second lithography step provided us with the possibility to correct non-fully-bridged contacts. Capillary forces in many cases resulted in the misalignment of the SWNT with respect to one of the leads. The misalignment could be easily fixed by having a wider metal layer on top, as provided via the second lithography process. Before the stage of including a second metal layer to our study, the problem of capillary forces was treated by the use of a critical point dryer (CPD) apparatus. The technique assures that a super critical phase is obtained (of carbon dioxide) during drying and thus that capillary forces are negligible and do not cause misalignment. The concept is briefly discussed in appendix H.

4.6.4. Optimizing the AS peak at zero bias

In order to correctly evaluate the phonons' effective-temperature, detection of an anti-Stokes G mode peak at zero bias is necessary. Most samples though have shown an anti-Stokes peak only while biasing the tube, lacking a peak at zero bias (appendix G). Accordingly, various attempts were employed to enhance the anti-Stokes intensity and the anti-Stokes/Stokes intensity ratios, before and after biasing the tube, respectively. Our objectives were to find the exact excitation energy for the anti-Stokes process, reduce relaxation channels available for the phonons, and increase peaks intensities via higher excitation energies on smaller diameter tubes. Some of the strategies applied are discussed below.

Suspended SWNTs

A suspended tube should provide lower saturation currents as was shown by Cao *et al.* [99] and Pop *et al.* [100]. At high-bias, it is assumed that the phonons should possess a significantly higher effective-temperature, as the generated optical phonons can not relax via the substrate. An increase in the anti-Stokes/Stokes intensities ratio is therefore expected. Our attempt to suspend the SWNTs utilized an ammonium fluoride (87.5:12.5) solution. It was used to etch away the SiO₂ layer. The goal was to thin the oxide layer so that the tube is no longer supported. The samples were dipped into the ammonium fluoride solution for a duration of about 3 minutes.

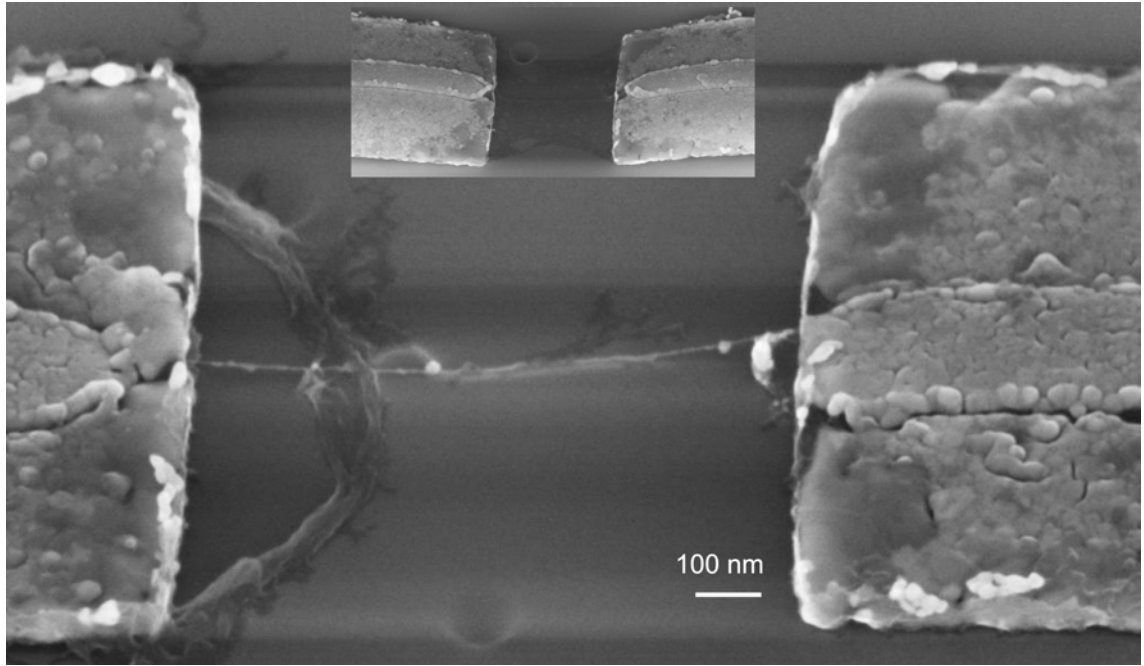


Figure 4.19.: SEM image of a 3 minutes etched contact by ammonium fluoride solution. The image was taken at 45° to demonstrate its strong adherence to the oxide layer except for its edges. Residues of SiO_2 are observed on the left side of the contact (sample w130c74p1b). Such residues contaminate the tube and are further illustrated in the inset (sample w130c81p1e).

They were subsequently dipped into water in order to stop the etching process. Shorter etching times were initially employed, however the tube still touched the oxide surface. It turned out that an increase in the etching duration does not provide better results as the electrode portion next to the bridging SWNT collapsed. Figure 4.19 demonstrates a contact bridged by an individual SWNT that has endured a 3 minutes etching process. The SWNT remained strongly adhered to the oxide layer except for its hanging edges. Also it is observed that some oxide material was trapped and contaminated the tube. The inset shows a similar problem with higher amount of oxide residues. It was further realized that the electrodes are too narrow in the vicinity of the contact for such a procedure. The whole structure collapsed and the tube remained supported by the oxide layer as demonstrated in Fig. 4.20 for a different contact. The major conclusion from the above results is that pre-patterned trenches should be employed for the tube deposition. The structure should include wider electrodes as to avoid any collapse occurrences. Further, tube contamination will be avoided as the tubes are deposited after the etching process.

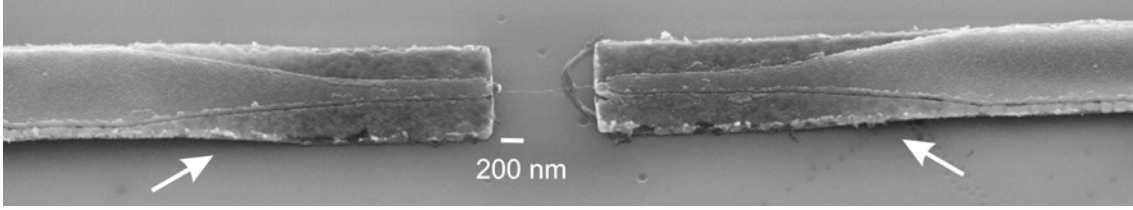


Figure 4.20.: SEM image of a collapsed contact. The image was taken at 45° to illustrate the steps occurring due to the etching process (marked by white arrows). The device remains with a non-suspended 1 μm long tube (sample w130c74p1c).

Small diameter SWNTs

NiCo SWNTs of 1 nm average diameter were produced by Frank Hennrich instead of the usual SWNTs material of 1.2 nm average diameter. The SWNTs were produced by the same technique as described in section 3.1, however with a slightly lower temperature (1000°C *versus* 1150°C). It is known that the excitation energies are increased for smaller diameter tubes, $E \propto 1/d$. The shift in excitation energy is demonstrated in Fig. 4.21 and was calculated to be ~ 43 meV for the transition energies of metallic SWNTs (E_{11}^M), within the black circle. The absorbance measurements were performed on surfactant-stabilized SWNTs suspensions in a D_2O medium rather than H_2O , as H_2O absorbs at the range of the first van Hove singularity of semiconducting tubes (~ 1800 nm, $E_{11}^{S,C}$).

Following the theory of Raman scattering, the intensity of emitted light is proportional to the 4th power of the frequency, $I \sim \nu^4$. Exciting the tube at shorter wavelength should to first order give more intense Raman signals. As previously mentioned, the modes of carbon nanotubes are obtained from resonant Raman rather than non-resonant Raman scattering processes. The above intensity enhancement may not follow the same power for the resonant processes however one might expect it to preserve its tendency. Since a general increase in all peaks intensities is expected by increasing excitation frequency, the desired anti-Stokes G mode intensity should also increase. If a ν^4 dependence is assumed, the anti-Stokes to Stokes intensity ratio is:

$$\frac{I_{AS}}{I_S} \sim \left(\frac{\nu_0 + \nu_{ph}}{\nu_0 - \nu_{ph}} \right)^4 \cdot \exp\left(-\frac{E_{ph}}{k_B T}\right) \quad (4.13)$$

Still, new samples of 1.0 nm on average diameter, produced in a similar manner as the device shown in Fig. 4.16, did not provide sufficient enhancement. The SWNTs

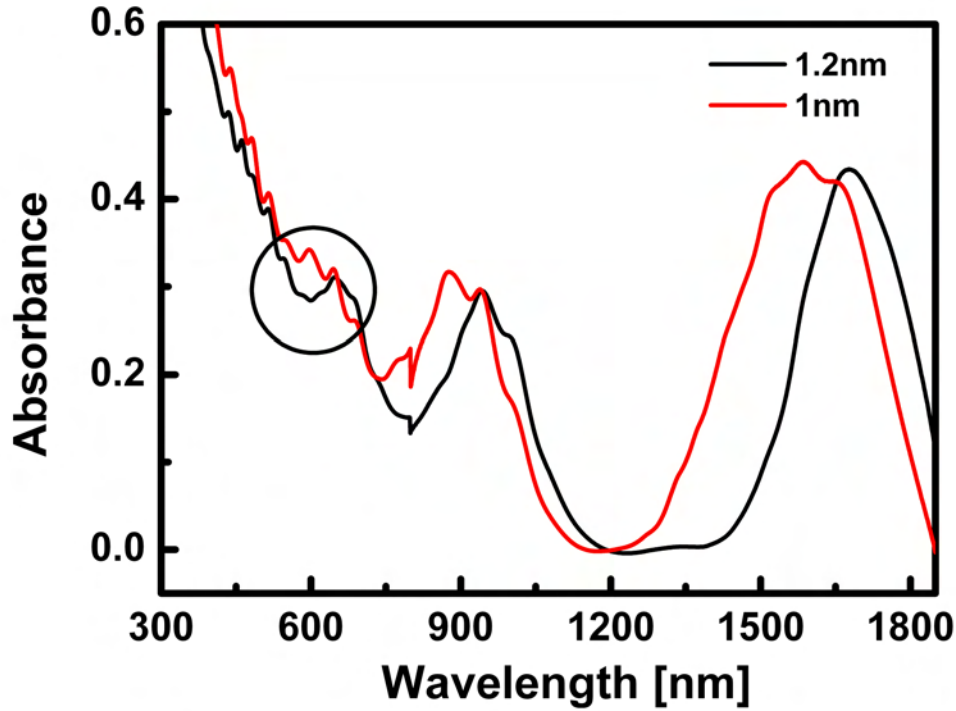


Figure 4.21.: UV-VIS-NIR spectra of 1 nm *versus* 1.2 nm NiCo SWNTs. The shift to higher excitation energies is shown for the smaller average diameter tubes (red curve). Circle denotes the excitation energies for metallic SWNTs (E_{11}^M). The other two main peaks corresponds to excitations of semiconducting tubes ($E_{11}^{S,C}$ and $E_{22}^{S,C}$). The steep increase in absorbance below 500 nm is due to π -plasmons. The measurements were performed on surfactant-stabilized SWNTs suspensions. Sharp wiggles are observed since the suspensions contained a large content of unbundled material. The surfactant and liquid were 1% NaCholate and D_2O , respectively.

were tested by both red (632.82 nm) and green (514.5 nm) lasers. The anti-Stokes G peak was still missing at zero voltage and appeared, if at all, only at elevated bias.

4.7. Towards electroluminescence

SWNTs are optically active nanostructures with a direct band-gap. Already in 2001, ambipolar electrical transport was reported in semiconducting SWNTs based field effect transistors (s-FETs) which facilitates the electrically induced optical emission from these devices [101]. This novel behavior was first observed from devices having

titanium carbide (TiC) contacts and SiO₂ passivation. Since then, more groups have reported the observation of infrared (IR) light emission from nanotube based FETs devices [102–104]. We attempted to obtain similar results using our own NiCo PLV SWNTs material. For this, a parallel study was performed to detect IR light from s-FETs devices fabricated via low-frequency dielectrophoresis.

Until recently, it has generally been accepted that an electrical ambipolar behavior is required for electroluminescence. Nevertheless, a recent study by Martty *et al.* [17] shows that near IR electroluminescence could also be achieved in unipolar s-FETs devices operating at high source-drain voltages, where light emission originates from radiative relaxation of excitons that were generated by high energy impact excitations. As electroluminescence could be observed from SWNT-based s-FETs with merely hole conduction, it was concluded that the mechanism for light emission is in fact based on only one carrier type, in contrast to the conditions required from ambipolar based s-FET devices [17].

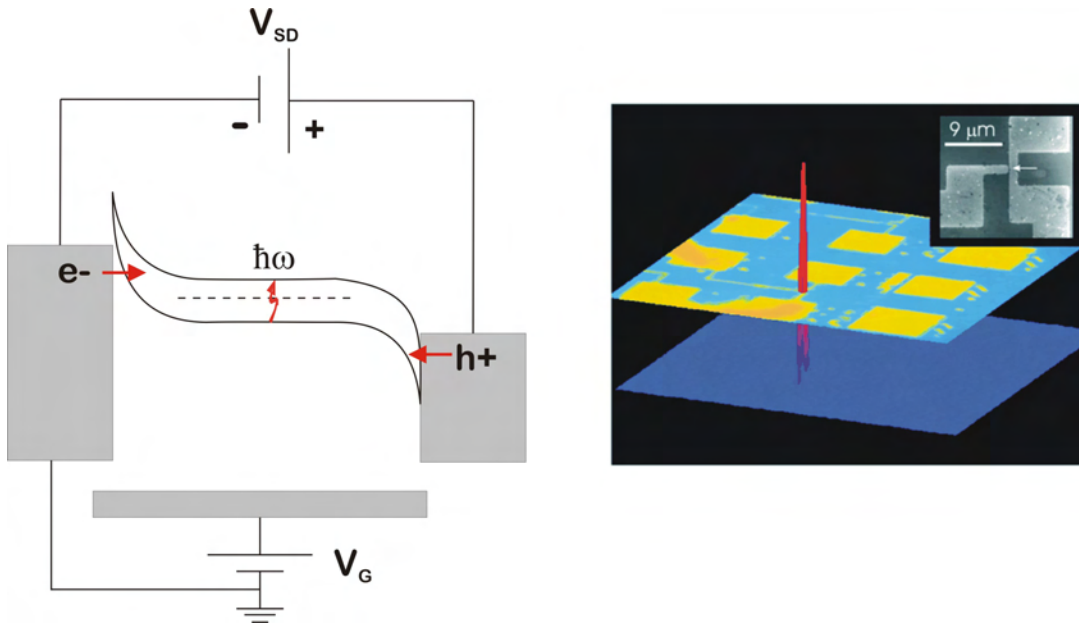


Figure 4.22.: On the left, an ambipolar scheme for IR light emission is illustrated. The injection of both electrons (e^-) and holes (h^+) is demonstrated through the SB barriers, with opposite electric field at each tube end. Their recombination inside the tube causes the emission of IR photons ($\hbar\omega$). A grounded gate electrode is also shown. On the right, a real light emission from an ambipolar SWNT s-FET detected by an IR camera. The light emission occurs only at the SWNT S-FET position shown by the white arrow in the inset. Taken from Ref. [102].

4. Results and discussion

The general idea of ambipolar behavior is to inject electrons and holes from opposite contacts into the channel (SWNT) where they radiatively recombine and emit IR light. This picture is illustrated by the scheme given in Fig. 4.22. A finite source-drain potential (V_{SD}) is applied and results in shifting the Fermi level of one of the metal electrodes. At the same time, a fixed gate field (V_G) is also applied where the combination of both V_{SD} and V_G potentials causes the situation of mutually coexisting barriers for electron (left contact) and for holes (right contact). The special band bending occurs because the tube bands (valence and conduction) are in fact fixed at the tube-metal interfaces. Their symmetry is a product of a mid-gap band lineup. If the $V_{SD} = 2 V_G$ potentials relation is to be used, as reported by Misewich *et al.* [102], an optimal light emission with equal electron and hole currents tunnelling through the thin Schottky barriers (SBs) is expected. The gate grounded electrode is located below the oxide layer. The inset on the right part of Fig. 4.22 is taken from the work of Misewich *et al.* [102] and demonstrates an IR light emission from a simultaneous injection of electrons and holes into a real semiconducting SWNT. The holes and electrons recombine and emit light similarly to silicon based devices. Various ways to achieve a s-FET SWNT-device with an ambipolar behavior were suggested throughout the years. It started from the junction property of a semiconducting SWNT with TiC contacts [101], continued with different ways of surface passivation processes which affects the alignment of the nanotube bands with respect to the metal electrode Fermi level [78] and ended with either thinning the gate oxide [105], adopting high- k gate dielectric materials [106] or performing gate structure engineering [107].

Since S-FETs are in fact one-dimensional SB SWNT devices, the modulation of their carrier-injection barriers is in fact the basis for the transistors action. Our study concentrated on thinning the gate oxide, as such geometry can provide a better control of the barrier heights by applying gate fields. Combined with V_{SD} one can control both height and width of the barrier. Once the barriers are reduced, controlling the channel conductance is significantly improved.

An electrical device is normally bonded to a chip carrier for electrical measurements. It is therefore important to ensure that the thin oxide is obtained only at the area at which the actual nanotube contacts are located and not where the leads for bonding are positioned, *i.e.*, to avoid short-circuits (see fabrication procedure in appendix I).

4.7.1. Ambipolar electrical behavior

Devices with both thin and thick oxide areas on the same chip (appendix I) were subjected to electrical measurements. Ambipolar electrical behavior was indeed achieved, however not frequently (in about 30% of the devices). Different source-drain and gate potentials combinations were applied to find the ambipolar domain where electron- and hole-currents overlap. The typical result we obtained is shown in Fig. 4.23.

The behavior is demonstrated by the change in source-drain current I_{SD} while changing the gate potential. Both cycle directions are given with the first one starting

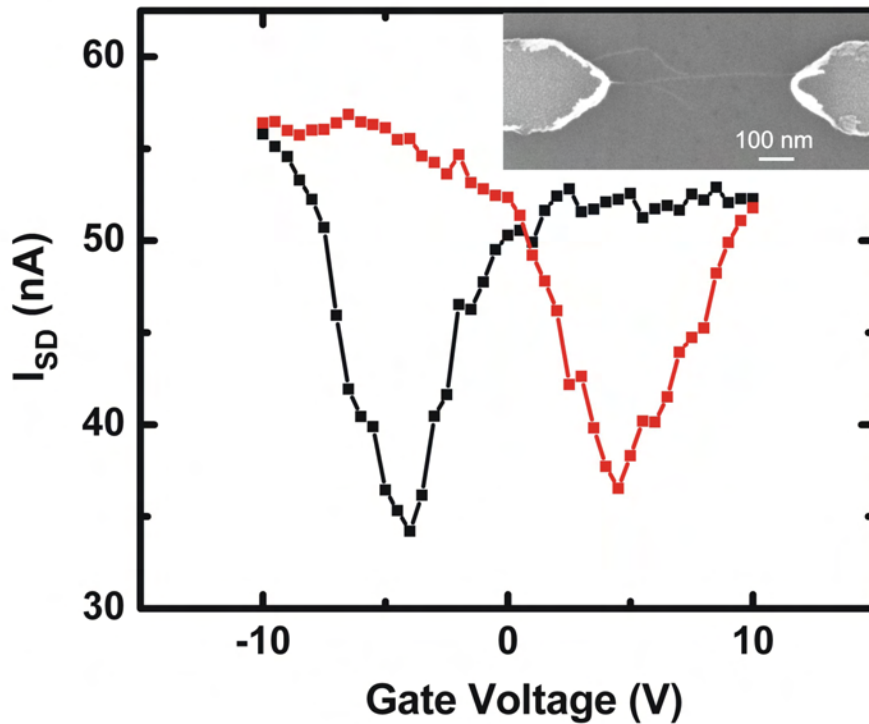


Figure 4.23.: Ambipolar electrical behavior observed from a SWNT s-FET device. A constant $V_{SD} = 0.3$ eV was applied while sweeping the gate voltage. The red cycle followed the black one. A strong hysteresis is observed. The hole conduction decreases for more positive gate voltages and changes to electron conductance at about -5 eV. The voltage range at which a V-shaped I_{SD} curve is observed is called the ambipolar domain, *i.e.*, where electrons and holes currents overlap. An image of the contact in the tube-on-metal configuration is shown in the inset. The tube is 0.5 μm long. Sample w130c02p1f.

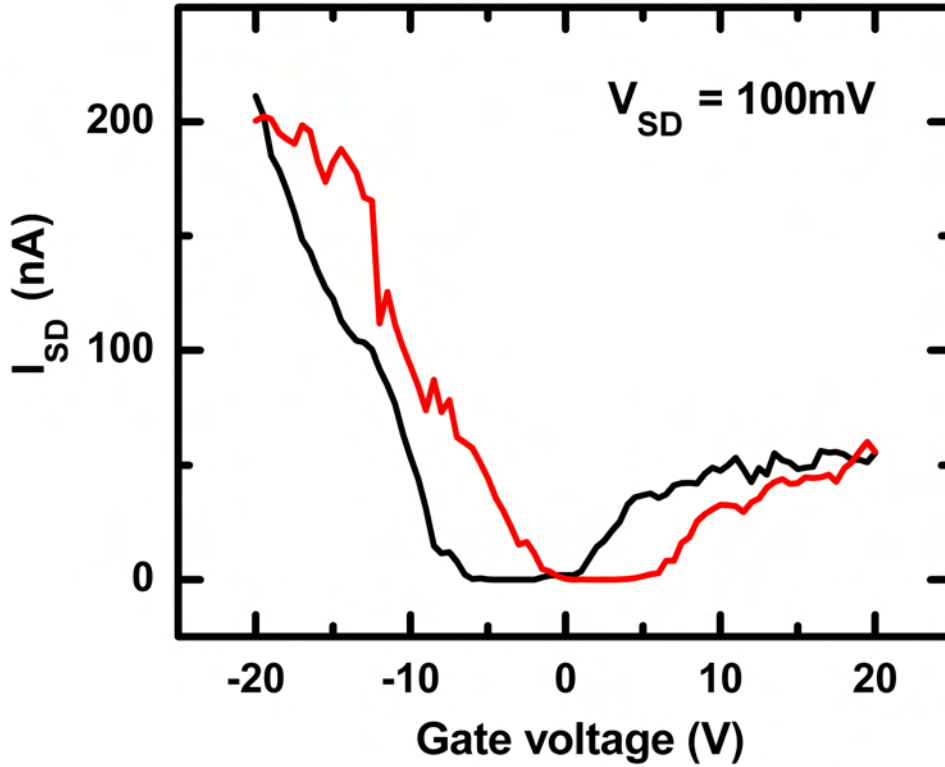


Figure 4.24.: Ambipolar behavior from a SWNT s-FET device with 800 nm gate oxide. A constant $V_{SD} = 0.1$ eV was applied while sweeping the gate voltage. The black cycle starting at negative gate voltage is followed by the red one. Stronger hole conduction is observed as well as a zero I_{SD} about and at zero V_G . Sample w118c81p2a.

at negative V_G . Note the strong hysteresis (section 4.3) and the non-zero I_{SD} at zero V_G . The non-zero current at zero gate bias is the result of the high capacitance between the SWNT channel and the gate electrode. This occurs for thin oxide geometry, where electric fields generated by the V_{SD} potential are stronger at the contacts, and affect the barriers to allow some current in the tube.

As mentioned above, the optimal light emission was reported for $V_{SD} = 2 V_G$ [102]. At this potential relation the bending is supposedly symmetric but only for a thick gate oxide geometry. With a thin gate oxide, one should deviate from this relation so as to obtain a higher electron conduction. It is known that due to the adsorption of oxygen on the electrode-SWNT interface, the alignment of the SWNT bands with respect to the electrode Fermi level is affected [78]. The SB is accordingly altered,

with holes or electrons tunnelling into the SWNT if the device is exposed to air or under high-vacuum and elevated temperatures, respectively.

As our devices were measured under a pressure of $\sim 10^{-5}$ mbar, the majority of semiconducting FETs devices showed a p-type character, and in particular if a thick gate oxide geometry was employed. However, on one occasion we detected an ambipolar behavior for a device with 800 nm thick gate oxide, as shown in Fig. 4.24. Hole conductance is observed to be stronger than the electron conductance. In addition, very high gate voltages were needed to obtain this performance. In contrast, moderate gate voltages are sufficient to achieve electron conductance with a thin oxide geometry, which is also improved if a deviation from the symmetric relation is employed. This was demonstrated in Fig. 4.23. Nevertheless, we could not detect any IR light from our FETs devices. Note that our setup does not provide clear information for the focal plane location. It therefore was not clear if the height of the objective ($WD = 10$ mm) was correctly positioned to collect light from the tube. As our device was fabricated with silicon as a substrate, no initial luminescence measurements could be used to find the correct location above the device. The silicon strongly fluoresces in the same range as the SWNT s-FET device, in addition to extra losses that could occur as the objective was not fully IR compatible.

4. *Results and discussion*

5. Summary and outlook

A clear correlation between electrical transport and Raman measurements was presented for both individual metallic and individual semiconducting SWNTs. The metallic SWNTs show a broad G mode (with $\Delta G^+ \approx 20 \text{ cm}^{-1}$ and $\Delta G^- \approx 60 \text{ cm}^{-1}$) while the semiconducting SWNTs show a narrow G mode (with both ΔG^+ and $\Delta G^- \approx 20 \text{ cm}^{-1}$). The fact that a broad G mode peak is dominating the spectra of individual metallic SWNTs can not be explained by the phonon-plasmon coupling model of Kempa [56]. Instead we propose a strong coupling of the underlying phonon mode to the electronic system as observed recently in graphite [84]. The data presented were discussed in terms of recently published theory [58]. It predicts frequency softening of the LO tangential mode along the nanotube axis and broadening of the G^- peak in metallic tubes as a result of the strong coupling of the LO mode to the electronic system. The strong coupling processes occurring in metallic SWNTs results in a much shorter lifetime for the particular phonon, as compared to semiconducting tubes.

The suggested mechanism of electron-phonon coupling processes in metallic SWNTs motivated us to perform a complementary study in which the Raman spectra of metallic SWNTs were investigated under an applied bias. A simultaneous study of electrical and Raman measurements on individual SWNTs was initiated. The idea was to verify the suggested mechanism of electron-phonon coupling in metallic SWNTs by an induced bias. Preliminary results showing the intensity growth of the anti-Stokes high-energy G peak in metallic SWNTs are presented. Nevertheless, we could not reach the high effective phonon temperature predicted by theory ($\sim 6000\text{K}$) for non-zero phonon occupation number ($n > 0$), *i.e.*, for non-thermalized phonons. Various ways in which one could improve the signal-to-noise of an anti-Stokes G peak as necessary for a more accurate estimation of the phonons' effective-temperature are discussed; some of them are ongoing projects.

5. Summary and outlook

The initial assumption that stronger electron-phonon coupling processes should occur in biased metallic SWNTs was based on the saturated $I-V_{SD}$ curves of individual metallic SWNTs [9–11]. However, it is not clear if the pronounced tendency of our curves towards current saturation is the real finger print for a stimulated emission of high-energy phonons. The distinction between heating processes occurring in the metallic SWNTs due to the applied bias and real phonon generation leading to an increase in the phonons' effective-temperature requires further study.

Outlook

Optimizing the anti-Stokes G peak at zero bias

To further improve the detection of an anti-Stokes G peak at zero bias, it will be interesting to use CoMoCAT SWNTs, produced by the chemical vapor deposition (CVD) technique. This tube material possesses an average diameter of about 0.8 nm [108]. The Raman measurement would apply a blue laser of 454 nm in wavelength (2.73 eV) so as to excite metallic SWNTs through their first pair of van Hove singularities, E_{11}^M . The use of such higher excitation energy is intended to energetically favor the scattering process of the anti-Stokes G mode (resonant enhancement) perhaps resulting in an intensity improvement relative to measurements on larger diameter tubes.

Raman imaging

The attempts in suspending the tubes or the use of higher excitation energies on smaller diameter tubes are in fact all trial and error procedures. In contrast, the determination of Raman excitation profiles for individual tubes should be very useful as it allows the detection of the optimized excitation energy of the various modes. So far, only mapping of the RBM modes was done on tubes in suspensions, as recently reported by Telg *et al.* [80]. The SWNTs in suspension were probed with a tunable laser as to find the highest intensity for the RBM mode of each detected tube. It would also be useful to analogously study the optimal excitation energy of the G anti-Stokes peak of *individual* SWNTs. Once the optimal excitation energy for the anti-Stokes peak is found, a bias can be applied to follow the evolution of the AS/S ratio. This procedure is expected to improve both anti-Stokes G peak intensity at zero bias as well as to allow more accurate determination of AS/S intensity ratios at elevated voltages.

Towards electroluminescence

Fabricating new devices (following the procedure described in appendix I) with sapphire rather than Si/SiO₂ as a substrate (to eliminate background fluorescence) should assist in finding the exact location of the focal plane for the IR light detection (using the long working distance objective, $WD = 10$ mm). The sample will be initially subjected to fluorescence measurements and only then to an electroluminescence test. The plan is to utilize the objective height obtained when the tube is detected for fluorescence.

Furthermore, the SWNTs should possess a smaller average diameter than that of the previously studied NiCo PLV SWNTs material ($d_{\text{avg}} \sim 1.2$ nm) due to detection considerations. IR light emitted from smaller diameter tubes should not be too far in the IR, especially since for a liquid nitrogen-cooled InGaAs detector the efficiency drops significantly at about 1600 nm. On the other hand, the use of smaller diameter tubes could be a disadvantage regarding the achievement of a mid-band lineup (the tubes are of larger band-gap). SWNTs with smaller band-gap are assumed to give symmetric devices, to which the injection of electrons and holes at the same time is easier. Finding the optimum conditions between detecting the electroluminescence and the ease of performance is therefore required.

5. *Summary and outlook*

A. Line-group notation

Single-walled carbon nanotubes have a line-group symmetry since they possess a translational periodicity only along their axis. Each nanotube defined by a specific chirality (n_1, n_2) belongs to a different line-group. Achiral tubes, however, belong to the same line-group in case they have an identical n . Since line-groups are in fact full-space groups for 1D systems, any state in the tube can be characterized by a set of quantum numbers, which consists of the linear momentum k and the angular momentum m . Achiral tubes possess additional vertical (σ_v) and horizontal (σ_h) mirror plane operations, resulting in additional parity quantum numbers.

The line-group notation for a specific irreducible representation is given by the general expression ${}_k\mathbf{X}_m^\pm$. The letter X represents the degeneracy of the representation, and can be assigned as A or B to denote a non-degenerate state whereas, E and G will represent doubly-degenerate and quadruply-degenerate representations, respectively. The letters A (even) and B (odd) give also the parity quantum number with respect to the σ_v operation in the case of achiral tubes. The m quantum number corresponds to the number of nodes ($2m$) in a wave around the circumference. In chiral tubes, the superscript (+) or (-) denotes even or odd parity under the horizontal U-axis operation (Fig. A.1), and in achiral tubes, under the σ_h operation; both for $k = 0$.

Following the above description, the irreducible representation ${}_0A_0^+$ denotes that the presentation is of a one-dimensional state located at the Γ -point ($k = 0$) that has zero nodes around the circumference ($m = 0$). The state has an even parity under both the vertical σ_v and horizontal σ_h reflection operations. It could also be that no parity is defined as for example in the following irreducible representation of a chiral tube: ${}_kE_2$, which represents a double-degenerate state (E) inside the BZ (excluding its boundaries $k \neq 0$ and $k \neq \pi/a$). Since $m = 2$, four nodes are obtained around the circumference. The irreducible representations at $k = 0$ can be given also in molecular notation, which correspond to the isogonal point groups D_{2nh} for achiral and D_q for chiral tubes [12]. In this notation, g and u subscripts denote

A. Line-group notation

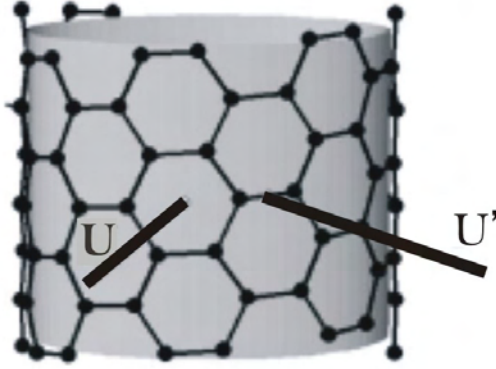


Figure A.1.: The U and U' horizontal rotational axis operations are perpendicular to the tube z -axis. Both exist in chiral and achiral tubes (here shown for a chiral (8,6) SWNT). The U-axis and the two-fold U'-axis point through the center of a hexagon and through the center of a C-C bond, respectively, where both are at 90° to the tube surface. Taken from Ref. [109].

even and odd parity under the σ_h mirror operation, respectively or in other words, denote symmetry for the inversion operation. Some examples of phonon symmetries under the σ_h operation can be found in Table 7.1 of Ref. [12] which are given in both line-group and molecular notations. Note that no mode with subscript u is Raman active. Further, in Ref. [110] one can find all the irreducible representations of chiral and achiral carbon nanotubes.

When an irreducible representation is given in the form A'_1 as for example in section 4.5, the prime denotes symmetry for a horizontal mirror plane. Right subscript 1 or 2 indicate symmetry for a vertical mirror plane or vertical \hat{C}_2 rotation operator (when present).

B. Surfactant-stabilized SWNTs suspension

Aqueous surfactant-stabilized SWNTs suspensions were produced with either sodium dodecylbenzene sulfonate (SDBS) or sodium cholate (NaCh). The chemical structures of the surfactants are given in Fig. B.1. Both surfactants produce stable suspensions, *i.e.*, no flocculation is observed within several weeks if 1 weight % of surfactant and 0.01-0.05 weight % tube material are used. It is assumed that the benzene rings in SDBS undergo π - π interactions with the rings of the carbon nanotube whereas the more bulky NaCh molecule may undergo a variety of possible interactions with the nanotube surface, *e.g.*, hydrophobic or acceptor-donor interactions, or even hydrogen bonds in case of acid treated tubes. In this thesis, NaCh was mainly used to produce suspensions for size exclusion chromatography which sorts as grown SWNTs according to their length [97].

A stabilized suspension is defined when the surfactant concentration is greater than the critical micelle concentration (CMC, for SDBS CMC = 0.097 weight % and

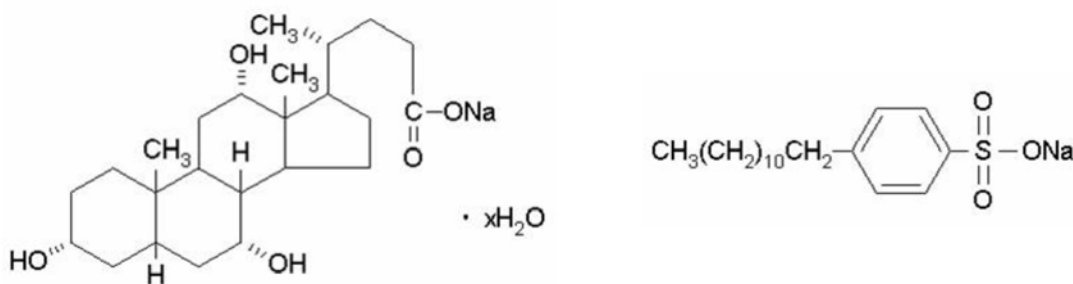


Figure B.1.: Sodium cholate (left) and SDBS (right) chemical structures. Note that the structure of sodium dodecyl sulfonate (SDS) is identical to that of SDBS, except for the benzene ring. In contrast to the SDBS and NaCh, it produces suspensions that show flocculation after a few days, *i.e.*, the nanotubes material starts to reaggregate (for 1 weight % SDS and 0.01-0.05 weight % tube material).

B. Surfactant-stabilized SWNTs suspension

for NaCh CMC $\simeq 0.6$ weight %¹. The micelles formed are dynamic in that their individual building block molecules exchange and diffuse continuously between the micelle and the solvent. The concentration used for the tube deposition was much lower than the CMC, and thus only the aliquot needed for deposition was diluted ($\times 100$) from the stabilized suspension and then immediately applied. In this thesis, the frequently used procedure for preparing the tube suspensions can be summarized as follows: SWNTs material (40 mg) was inserted and mixed homogeneously into 200 ml DD H₂O solution at a 1% SDBS (or NaCh) surfactant concentration². The resultant suspension was of 0.2 mg/ml tube concentration. Sequentially, the suspension was diluted by a factor of 10 and sonicated (with a TiAl₆V₄ alloy finger of 13 mm in diameter and 133 mm in length)³ for a duration of 10 minutes while cooling the plastic container via an ice bath. The suspension was then centrifuged at 154000 g for about 2 hours. The upper 50% of the supernatant was then carefully decanted into a glass container. The resultant suspension was thus at a tube concentration of 0.02 mg/ml (or 0.002 weight %) and 0.1% of SDBS (or NaCh). For the deposition, 20 μ L of tube suspension was inserted into 2 ml DD H₂O (diluted by a factor of 100) and immediately applied onto the electrically wired chip.

Sharp absorption peaks are the fingerprint of a surfactant-stabilized individual SWNTs suspension. In contrast, broad absorption bands are obtained from suspended bundles. A suspension containing mostly individual SWNTs will show fluorescence in the near infrared, however if mostly bundles are present, the fluorescence is quenched due to the adjacent metallic tubes in the bundle. Note that sharp absorption peaks and observable fluorescence spectra only indicate that a high fraction of the tube material is present as individual tubes. Yet, such measurements alone can not provide the quantitative extent of the bundled material present, and thus further characterization must be performed on the material for example by AFM or TEM measurements, *i.e.*, after a fraction of the material was transferred onto a surface. In general, the disadvantage of using any surfactant is the difficulty to remove it before electrical transport measurements.

¹The geometry of the NaCh molecule, which belong to the group of steroid amphiphilic bile salts compounds, is divided into a hydrophilic and a hydrophobic concave surface on each side of the molecule. Their common organizational growth principle or aggregation above their CMC was found to be by elongation [111]. The CMC values were measured by Krupke *et al.* [63].

²Other surfactant concentrations like 0.5% were also used.

³Maximum sonicator power is 200W. In this thesis, sonication procedures were performed at $\sim 40\%$ power.

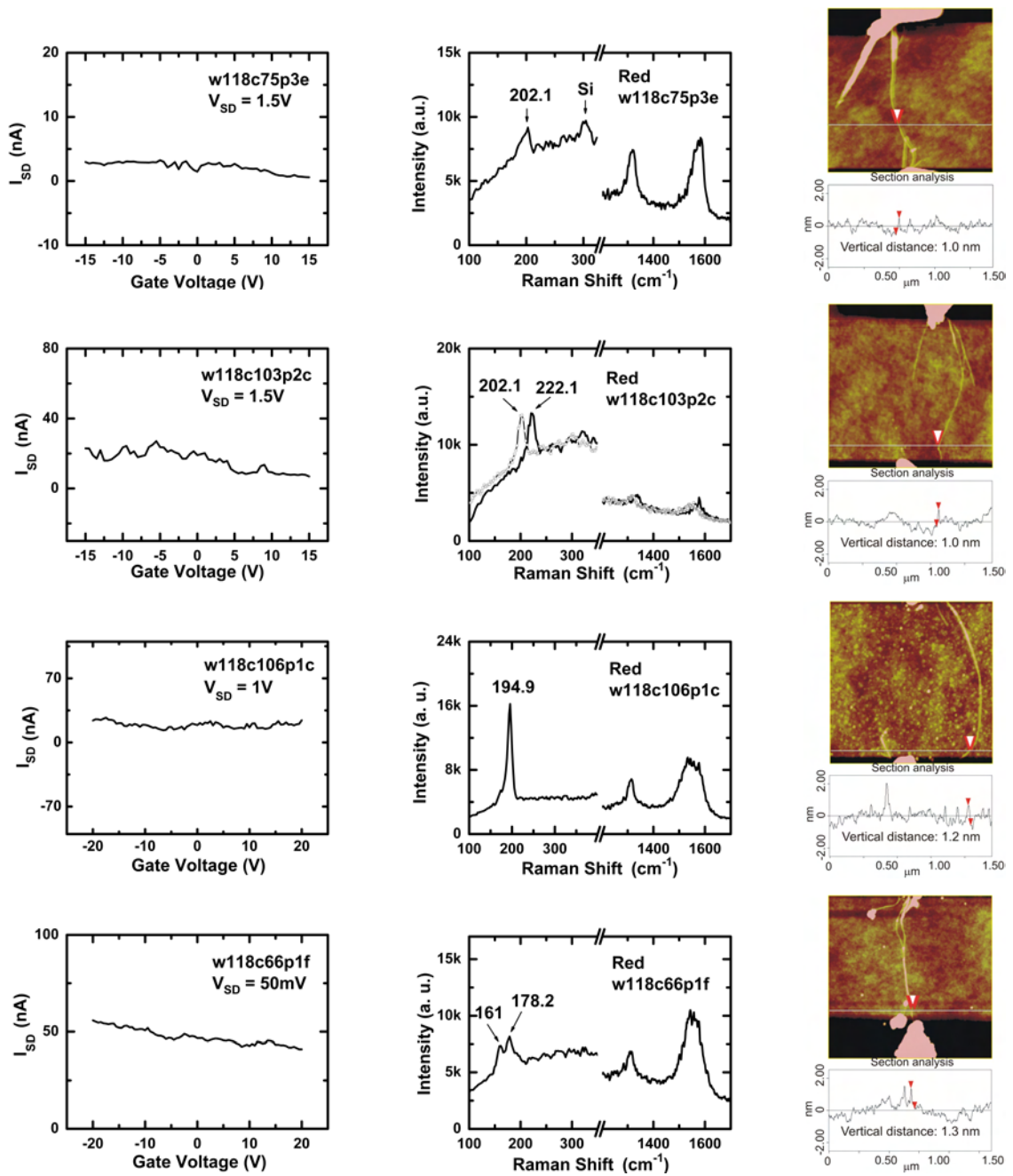
C. Electrical and Raman correlation

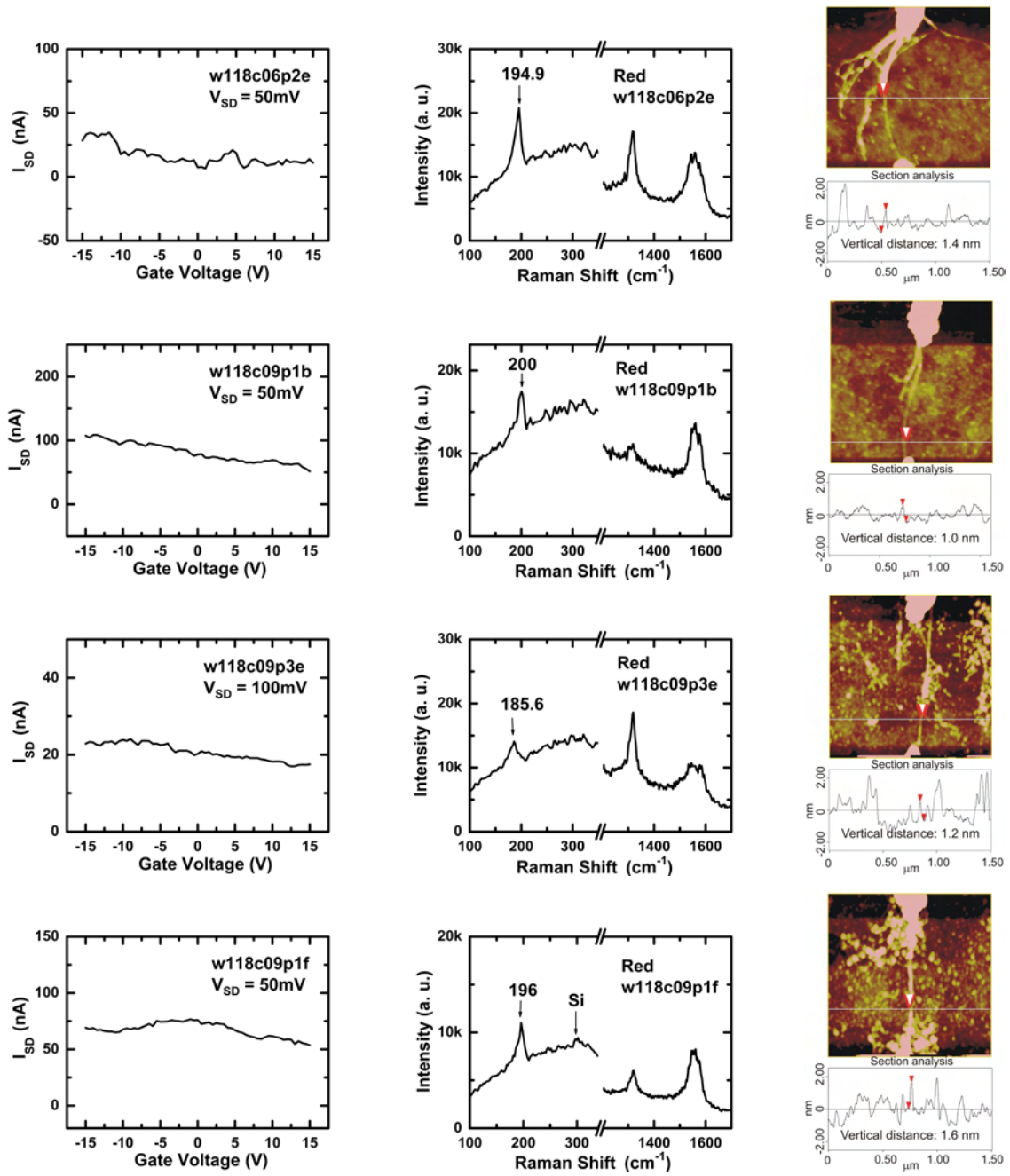
A correlation between electrical transport and resonant Raman spectroscopy measurements on 10 individual metallic (Table 4.1) and 15 individual semiconducting SWNTs (Table 4.2) is presented. AFM images of the individual SWNTs are also shown.

A broad G mode peak line-shape is clearly observed for the metallic SWNTs *versus* a narrow G mode for the semiconducting tubes. Red and Green refers to laser excitation energies of 1.96 eV and 2.41 eV, respectively.

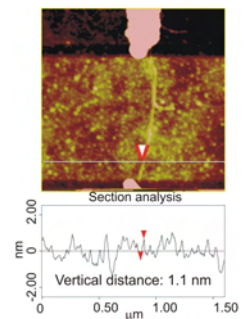
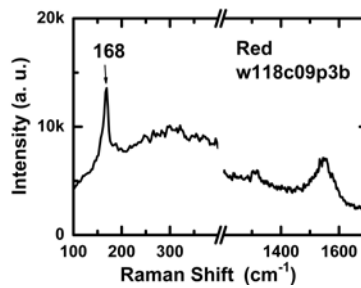
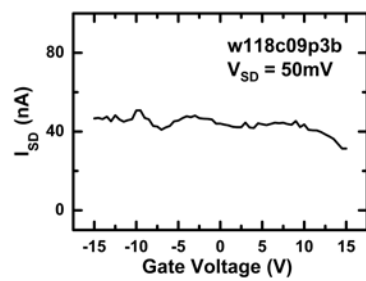
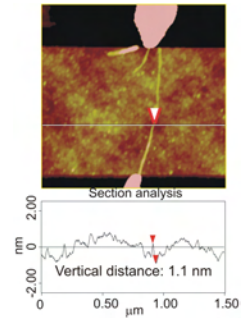
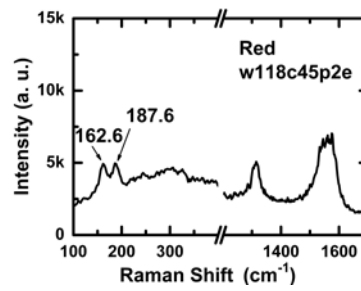
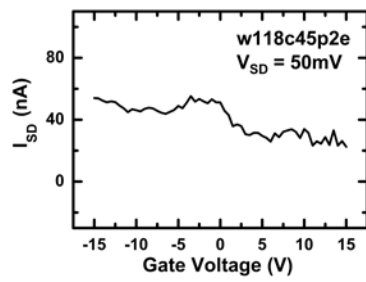
All Raman spectra were taken at 3 mW laser power via a 100x objective ($N_A = 0.9$, $WD = 2.8$ mm) and a 50 μm fiber core-diameter. Accumulation times were 10 sec. Two Raman spectra are shown in cases where either the bridging tube or a non-bridging tube-segment could be detected (*e.g.*, sample w118c103p2c). When two RBM signals are observed in the Raman spectrum, both short tube-segment and bridging tube were detected simultaneously (*e.g.*, sample w118c66p1f). As both peaks show a frequency that could match a metallic tube, both are presented (also in Table 4.1). Same applies for the semiconducting w118c93p1e tube.

C.1. Metallic SWNTs

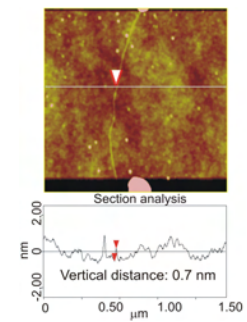
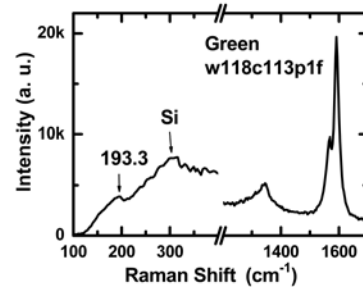
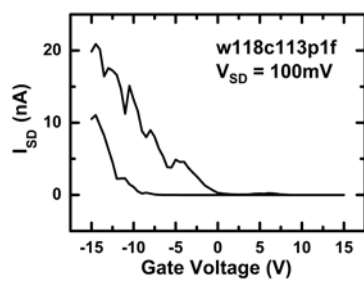
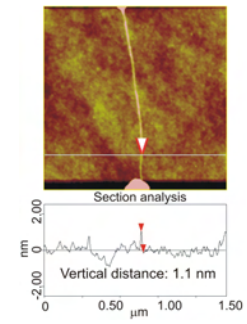
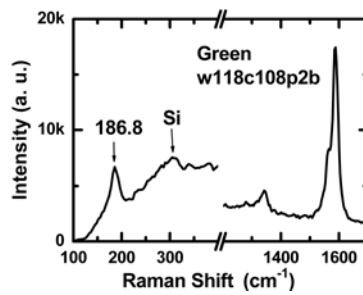
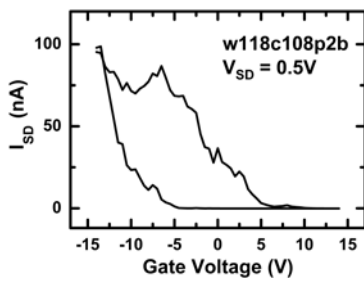
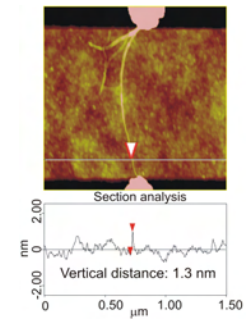
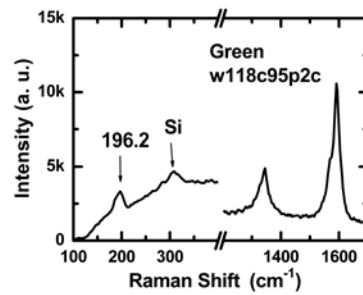
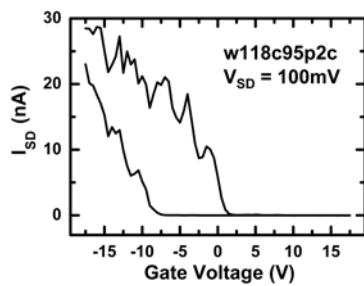
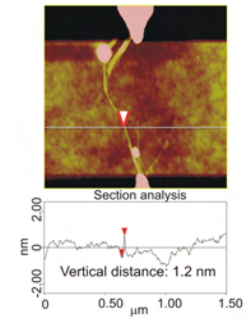
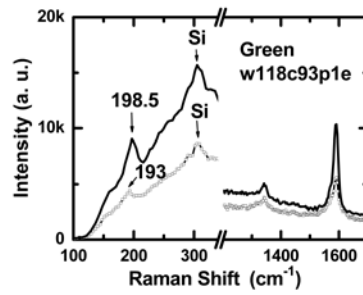
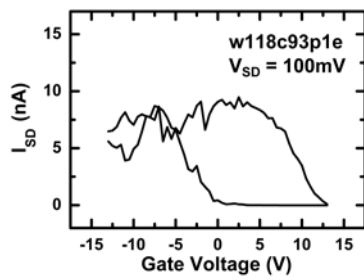




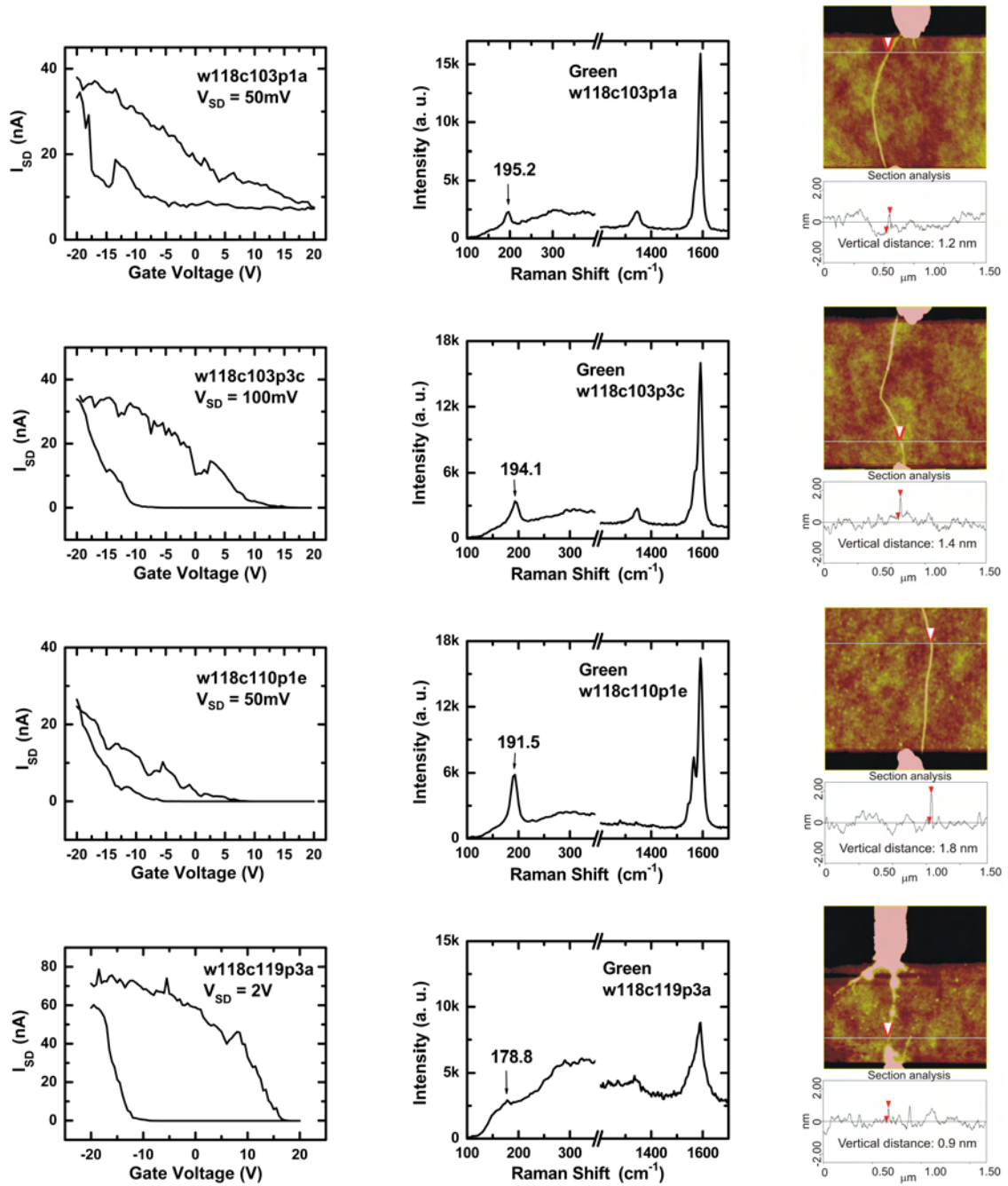
C. Electrical and Raman correlation

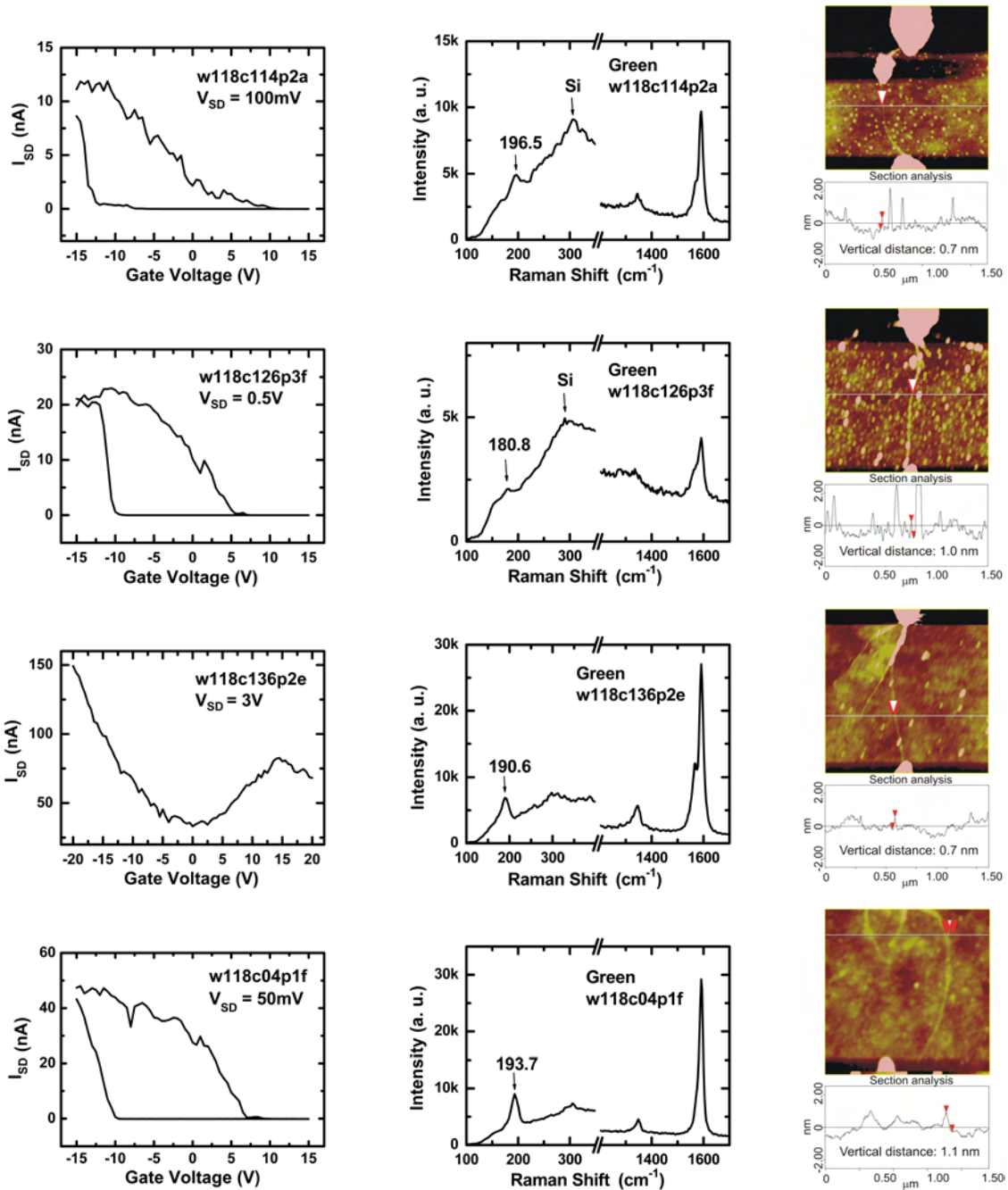


C.2. Semiconducting SWNTs

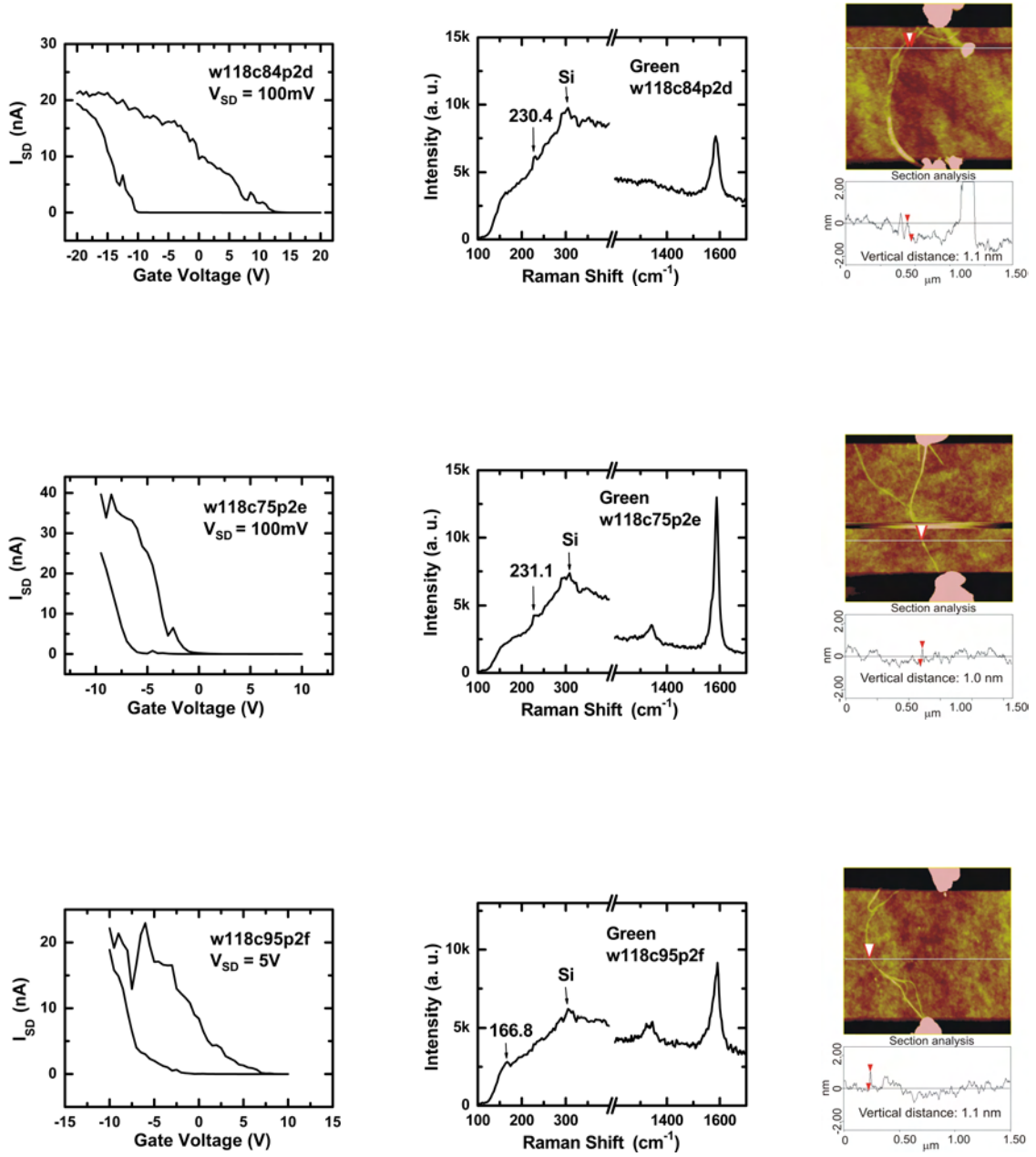


C. Electrical and Raman correlation





C. Electrical and Raman correlation



D. Asymmetric BWF line-shape

The G band in metallic SWNTs is normally fitted with a Lorentzian line-shape for the higher-frequency G^+ peak and a BWF line-shape for the lower-frequency G^- peak [85]. Both frequency and broadening of the G^- peak are assigned to a coupling mechanism of discrete phonons to an electronic continuum, where the asymmetric line-shape of this peak is given by the following expression [112]:

$$I(\omega) = I_0 \left(\frac{[1 + (\omega - \omega_{\text{BWF}})/q\Gamma]^2}{1 + [(\omega - \omega_{\text{BWF}})/\Gamma]^2} \right) \quad (\text{D.1})$$

where the parameter $1/q$ accounts for the coupling interaction of the discrete phonons (of q wave vector) with the continuum of electronic states, ω_{BWF} is the BWF peak frequency at maximum intensity I_0 and Γ accounts for broadening.

The formula is commonly used to describe Raman spectra of various semiconductors (*e.g.*, Figure 4.9 of Ref. [112] showing room-temperature Raman spectra for a p-type Si at different excitation energies) as they contain different electronic excitations which can be studied by the Raman scattering technique. Since 1999, it has been also used to fit Raman bands of various sp^2 carbon materials and in particular to fit the broad feature at $\sim 1540 \text{ cm}^{-1}$ of metallic SWNTs bundles [51, 85, 113, 114].

A model describing the plasmon modes in a single metallic SWNT and bundles of metallic SWNTs was developed by Kempa [56]. It shows that hybrid plasmon-phonon modes occur in metallic SWNTs, which form the BWF line-shape of the G^- peak, where its intensity is enhanced in metallic SWNTs bundles. Its main conclusion is shown in Fig. D.1 where a strong asymmetric BWF line-shape is obtained for a metallic bundle, however, only a weak shoulder for an individual metallic SWNT is found.

These calculations agree with experimental findings on metallic SWNT bundles (*e.g.*, Figure 3 of Ref. [63]) however, do not agree with the observed line-shape of an individual metallic SWNT as discussed and demonstrated in section 4.5.

D. Asymmetric BWF line-shape

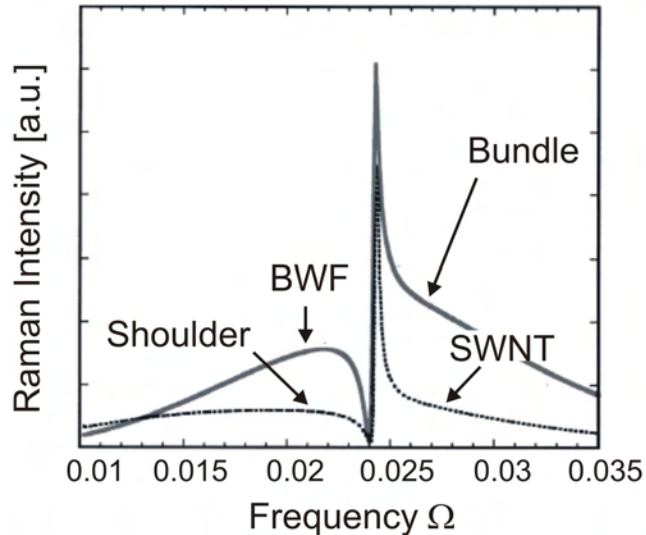


Figure D.1.: Calculated Raman intensity *versus* the normalized frequency $\Omega = \hbar\omega/E_F$. A strong asymmetric BWF peak is observed for a bundle composed of 9 metallic (9,0) zig-zag tubes (solid line), compared to only a weak shoulder for an individual (9,0) metallic tube (dotted line). Taken from Ref. [56].

Recently, an experimental study about the vanishing of the BWF component in individual metallic SWNTs was published by Paillet *et al.* [115]. Both RBM and G modes of individual metallic SWNTs were spectroscopically measured. In accordance with our thesis conclusions, they claimed that the BWF feature vanishes in isolated metallic SWNTs. Note that this work was published at the same time as ours [52]. In contrast to our study though, their determination for metallic character was based only on resonance conditions, *i.e.*, metallic tubes should be excited by the specific excitation energy used. No additional electrical measurements were performed. The G band of their isolated metallic CVD grown SWNTs was fitted with few narrow Lorentzian components, in contrast to only two shown in our study with a broad Lorentzian G^- feature. Furthermore, the presented data included only two spectra of individual tubes without any supporting material. Nevertheless, their main conclusion agrees with ours, namely that the BWF line-shape appears solely in metallic SWNTs bundles and is missing in individual metallic SWNTs.

E. Kohn anomaly in graphite

The Kohn anomaly is a phenomenon that is normally observed in metals and is defined as an abrupt change in the frequency of lattice vibrations on certain Fermi surfaces [116]. The frequency of certain phonons in the BZ abruptly changes due to a change in the screening ability of conduction electrons. These phonons, which cause virtual excitations of electrons, are of $q \leq 2k_F$ wavevectors and connect two electrons on the Fermi surface, *i.e.*, $k_2 = k_1 + q$, with k_1 and k_2 electron wavevectors. The sudden frequency change is observed as a dip in the phonon dispersion. Note that the electrons' screening ability reduces dramatically as $q > 2k_F$, that is, electronic excitations no longer occur.

As the electronic structure of graphite is semimetal in character, its atomic vibrations are partially screened by the conducting electrons. The Fermi surface of graphene is the point where the electronic gap is zero. This occurs at the two equivalent points K and K' of the BZ, and since the two points are connected by the vector K, Kohn anomalies can occur for $q = \Gamma$ and $q = K$ phonon wave vectors (Fig. 2.7). The optical high-energy and zone-boundary modes at the Γ and K points are the phonons responsible for the Raman G and D peaks in carbons, respectively. Figure E.1 shows the recent experimental points of various phonon branches obtained by inelastic x-ray scattering experiments on a graphite single crystal [86]. Piscanec *et al.* [84] have compared their DFT calculations with these data points in order to prove that the electron-phonon coupling matrix element can be directly obtained from the phonon dispersion. The experimental data for the LO mode (red), the TO mode (blue) and the (longitudinal acoustic) LA mode (green) as well as the resultant phonon dispersion obtained from their DFT calculations are indicated by the colored circles and solid lines, respectively.

Two Kohn anomalies are illustrated in the phonon dispersions at the Γ and K points by the discontinuities in the frequency derivative of the highest optical branches (HOBs) of the E_{2g} and the A'_1 modes at these points. Each red line displays the

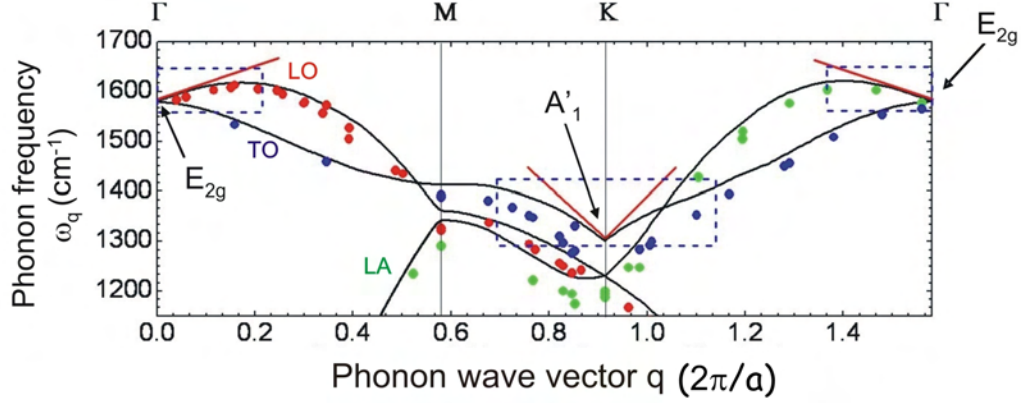


Figure E.1.: Computed phonon frequencies along the Γ -K and Γ -M high-symmetry directions (solid lines) and the data points obtained from inelastic x-ray scattering experiments (colored circles). The Γ - E_{2g} and the K- A'_1 modes of the HOBs at the Γ and K points are indicated. Red lines are the linear dispersions obtained from Eq. E.1. Modified from Ref. [84].

change in phonon frequency and exhibits a non-zero slope, which indicates a non-analytic behavior of the phonon dispersion. Note that at the Γ -point the E_{2g} mode of the HOB is doubly degenerate, whereas near Γ , the two modes split into an upper optical branch (LO) and a lower optical branch (TO), where the non-zero slope corresponds only to the LO branch. The $\alpha_{\Gamma}^{LO} \neq 0$, $\alpha_{\Gamma}^{TO} = 0$ and $\alpha_K \neq 0$ are the slopes of the LO and TO phonon branches at the Γ -point and the slope of the phonon branch at the K-point, respectively. Their theoretical expressions were given by:

$$\alpha_{\Gamma\text{-theo}}^{LO} \propto \frac{\sqrt{3}\pi^2 \langle D_{\Gamma}^2 \rangle_F}{\beta} \quad \text{and} \quad \alpha_K^{\text{theo}} \propto \frac{\sqrt{3}\pi^2 \langle D_K^2 \rangle_F}{\beta} \quad (\text{E.1})$$

with $\beta = 14.1$ eV and are plotted in Fig. E.1 by the linear red lines. Both expressions were then used to find the experimental values for α_{Γ}^{LO} and α_K using the experimental data points. Good agreement was found with the calculated values.

F. Hot phonons

The term hot phonons is generally used when various non-equilibrium phonon temperatures can simultaneously exist in a certain crystal. Here, the term is used with respect to the high-energy optical phonons' occupation that is believed to be the major cause for high-field ballistic transport limitation in metallic SWNTs. The initial goal from the theoretical point of view was to justify the experimental scattering length of $l_{\text{high}} \sim 10\text{-}15$ nm in the high-bias regime, as reported by Yao *et al.* [9], Park *et al.* [10] and Javey *et al.* [11]. The main conclusion from Lazzeri *et al.*' calculations [33] was that the phonons involved in high-bias electron transports are not in thermal equilibrium. The conclusion opposes what was generally assumed before. The main points of the theoretical treatment are given below.

An analytic expression for the scattering length was derived and is given in Eq. F.1. It can be seen that this formula contains the phonon occupation number, n . Lazzeri *et al.* [33] have considered the contribution merely from the emission of phonons by back scattered electrons, based on the assumptions in these early experimental papers [9–11], where only back scattering by Γ -point and K-point phonons were considered in deriving the electron scattering length at high-bias, *i.e.*, $l_{\text{high}} = (1/l_{\Gamma}^{\text{bs}} + 1/l_{\text{K}}^{\text{bs}})^{-1}$, where bs stands for back scattering. Forward scattering processes were neglected since they do not change the electron's propagation direction and thus do not contribute to the resistance, *i.e.*, they have a negligible effect on the current. It was also assumed that as long as the bias is smaller than 1V, the mobile electrons belong to the π bands near the Fermi energy E_{F} (footnote 4 of section 2.3.2). Scattering into higher energy bands was neglected. The computed scattering length $l = \tau v_{\text{F}} = \tau \beta / \hbar$ for a metallic SWNT was given by:

$$l_{q\eta} = \left(\frac{4\pi}{\sqrt{3}} \frac{M\hbar\omega_{q\eta}}{\hbar^2 a_0^2} \frac{\beta^2}{|\tilde{D}|^2} \right) \left(\frac{d}{n_{q\eta} + 1} \right) \quad (\text{F.1})$$

where $|\tilde{D}|^2$ is the square of the electron-phonon coupling matrix element of a tube of

F. Hot phonons

diameter d , τ is the decay time of an electron, v_F is the Fermi velocity, and all other parameters are as given in section 4.5. The matrix element $|\tilde{D}|^2$ of an arbitrary metallic SWNT was derived from zone-folding the corresponding matrix element of graphene. The approach was shown to be valid as long as curvature effects are negligible. The scattering lengths of three different tube diameters: 0.8, 1.49 and 2.5 nm, using the graphene phonon frequencies $\hbar\omega_\Gamma \simeq 196$ meV and $\hbar\omega_K \simeq 161.2$ meV were calculated. The original hypothesis from early experiments was that the phonons are thermalized and thus no phonon accumulation occurs ($n \simeq 0$). Under this condition, Eq. F.1 simplifies to:

$$l_{\text{high}} = 65 d \quad (\text{F.2})$$

Eq. F.2 generates a scattering length which is one order of magnitude higher (~ 100 nm for a tube of diameter 1.5 nm) than the experimental scattering length (~ 10 -15 nm) obtained for 1-3 nm in diameter metallic SWNTs [9–11]. Three independent experiments on a variety of different tubes obtained similar results and thus no experimental uncertainty should be the cause for the disagreement. Further, the calculated electron-phonon coupling matrix elements of graphite [84] have been shown to reproduce very well those extracted from the experimental graphite phonon-dispersions or from the D-peak dispersion. It was therefore concluded that the hypothesis of thermalized phonon occupation ($n \simeq 0$) was probably wrong. It was suggested that only a significant phonon occupation could explain the small experimentally measured scattering length, *i.e.*, $n > 0$.

Hot phonons could be generated only if the condition of excitation rate $>$ thermalization rate occurs during high-field transports. Under these conditions ($n > 0$) one must consider the contribution of both phonon absorption and emission. The scattering length was consequently re-estimated:

$$l_{\text{high}} = \frac{65 d}{2n + 1} \quad (\text{F.3})$$

According to this expression a tube with $d = 1.5$ nm could recover the experimental scattering length (~ 10 -15 nm) only for occupation numbers of $n = 2.7$ -5. This corresponds to an optical phonons' effective-temperature of $T_{\text{eff}} \gtrsim 6000$ K. This high value supports the speculation that the phonons involved in high-bias electron transports are not in thermal equilibrium. Note that the temperature is related only to Γ -point phonons ($q \approx 0$) that are directly excited by first order scattering processes. This temperature is not the nanotube temperature.

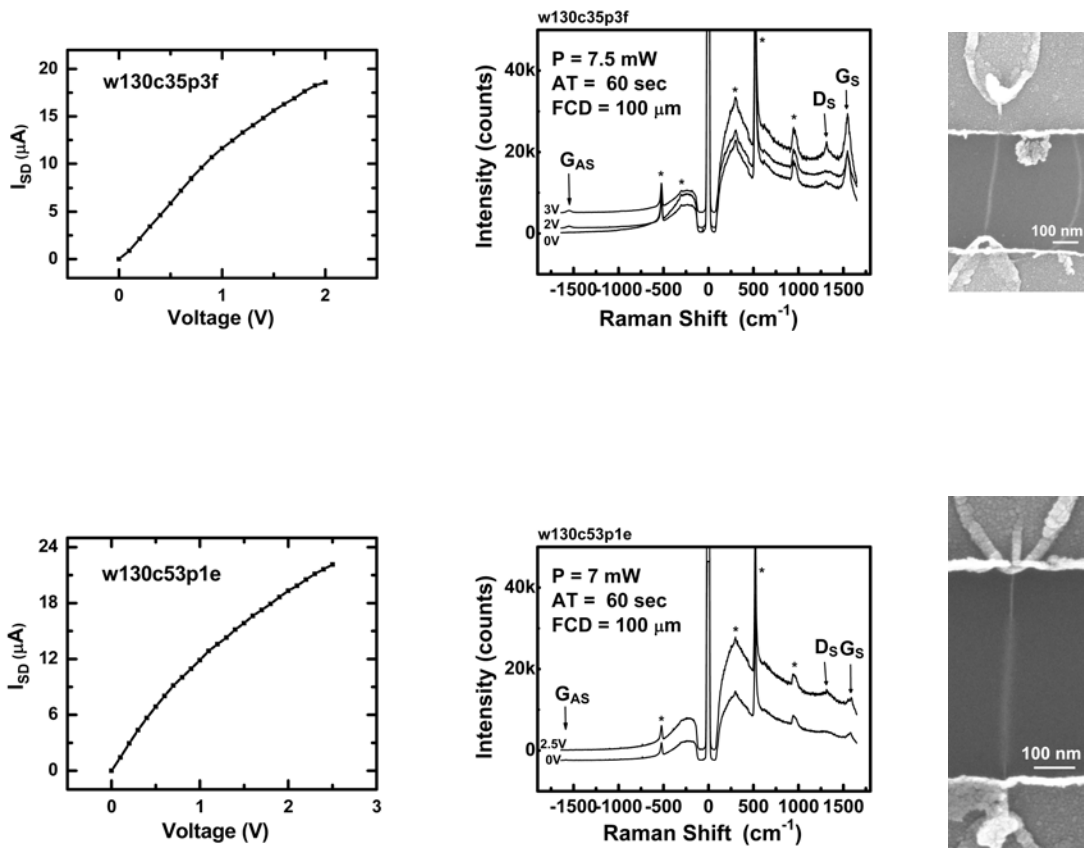
G. $I-V_{SD}$ curves, Raman spectra and SEM images of biased SWNTs

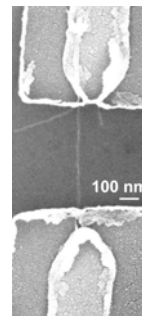
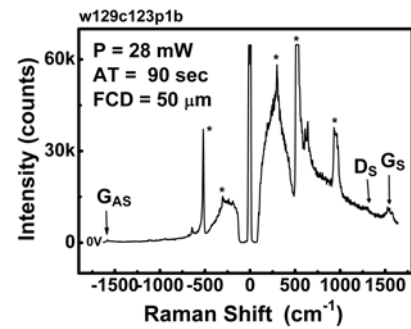
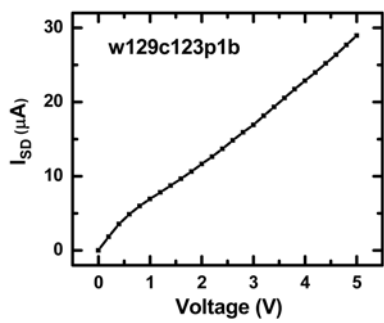
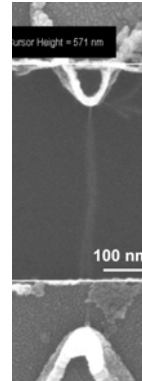
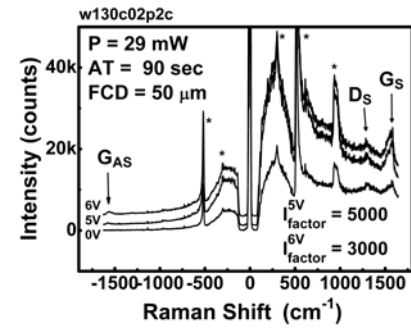
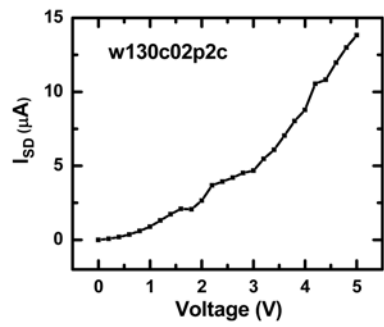
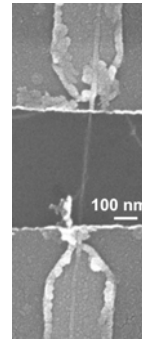
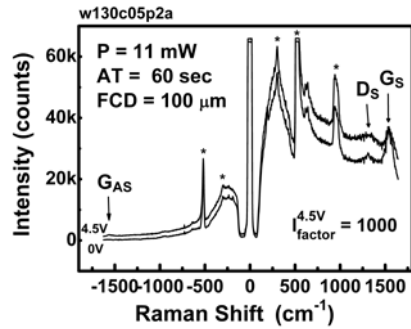
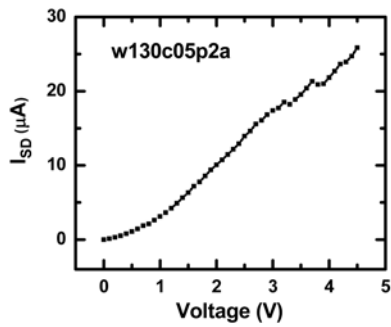
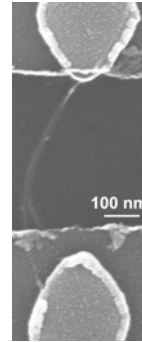
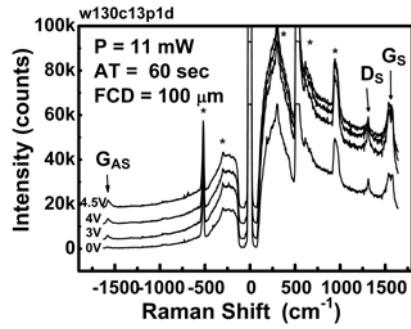
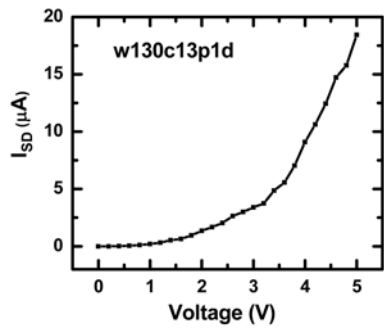
We present some representative examples of $I-V_{SD}$ curves and Raman spectra originating from biased metallic SWNTs. The contacts were prepared in the metal-on-tube configuration (unless otherwise specified), which in most cases presented a pronounced tendency towards current saturation. Nevertheless, if an anti-Stokes G peak was observed, it was only at elevated bias and lacking at zero bias for most samples. The data presented contain SWNTs with various lengths ($\ell = 0.5 \mu\text{m}$ or $1 \mu\text{m}$) and diameters ($d_{\text{avg}} = 1.2 \text{ nm}$ or 1.0 nm). All Raman spectra were taken with 632.82 nm wavelength, under Ar ambient and a 100x objective ($N_A = 0.7$, $WD = 10 \text{ mm}$). The spectra are further shifted vertically to follow the evolution of the anti-Stokes G peak intensity. In cases that an anti-Stokes G peak was missing at both zero and elevated bias, the spectra are given to show the RBM mode evolution at the various voltages (samples w130c881d and w130c893d). Note that a RBM peak did not appear in all samples. Peaks at $\sim 300 \text{ cm}^{-1}$, $\sim 520 \text{ cm}^{-1}$ and $\sim 1040 \text{ cm}^{-1}$ originate from the Si/SiO₂ substrate and are marked with an asterisk. Burned contact (w129c123p1b) shows a spectrum only at zero bias.

Note that sample **w130c13p1d** ($0.5 \mu\text{m}$ long and $d_{\text{avg}} = 1.2 \text{ nm}$) reveals a non-saturated $I-V_{SD}$ curve, however shows a pronounced intensity for the anti-Stokes G peak at zero bias, which increases at elevated bias.

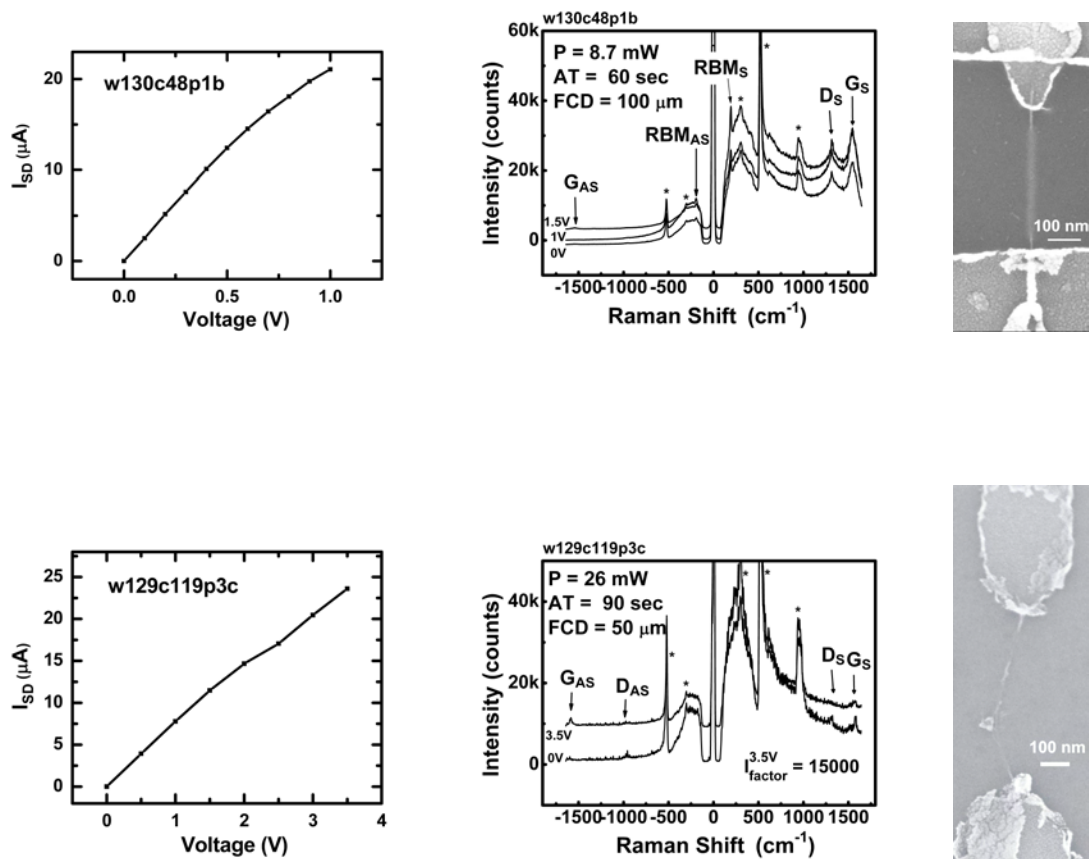
Sample identity, laser power (P), fiber core-diameter (FCD) accumulation time (AT) and voltages (V) are all indicated on the corresponding Raman spectra. For Raman spectra where an intensity factor was added, the specific factor is specified as I_{factor}^V .

G.1. $\ell = 0.5 \mu\text{m}$ $d_{\text{avg}} = 1.2 \text{ nm}$

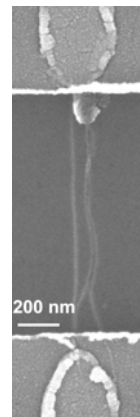
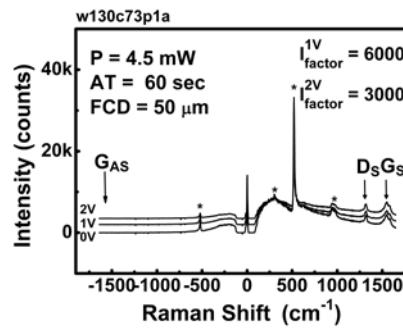
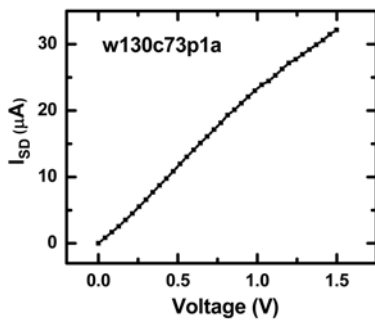
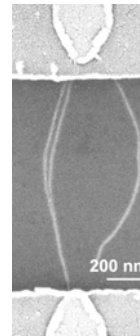
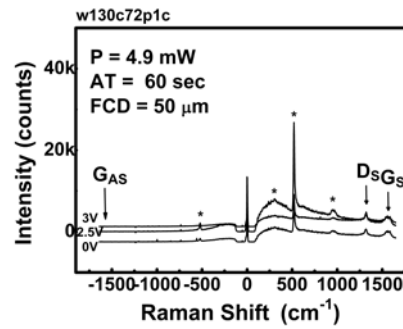
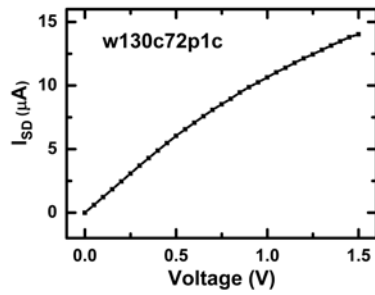
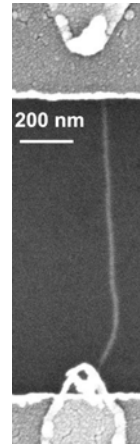
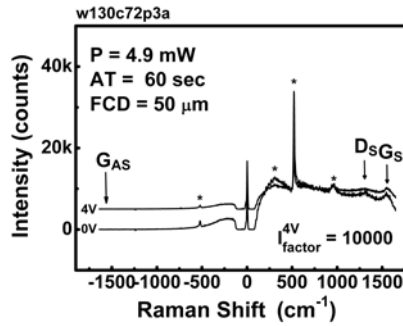
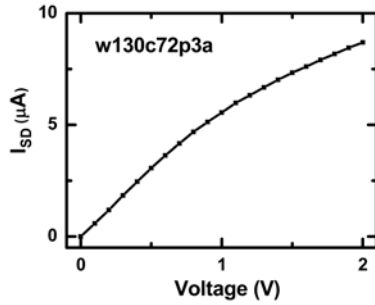




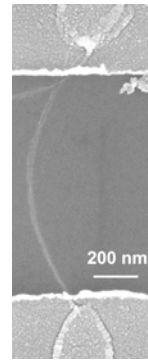
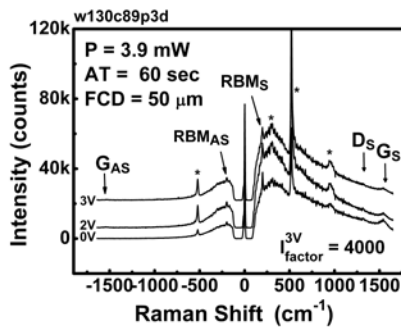
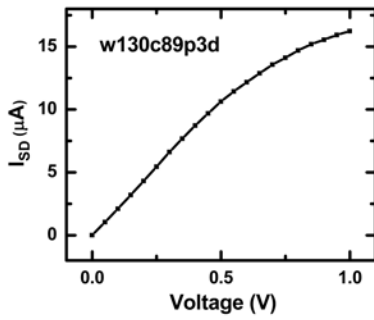
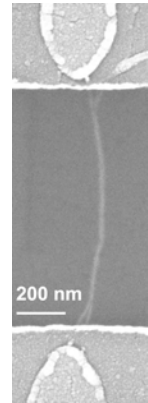
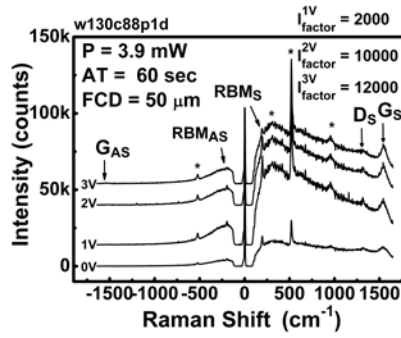
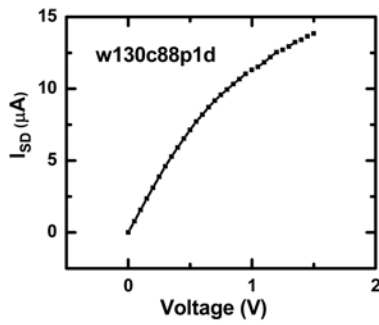
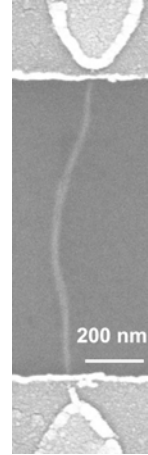
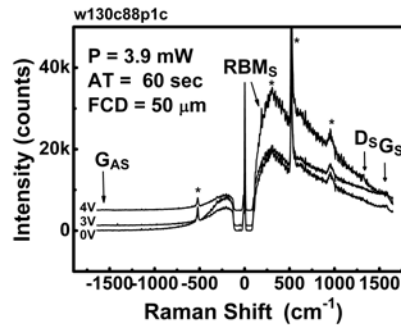
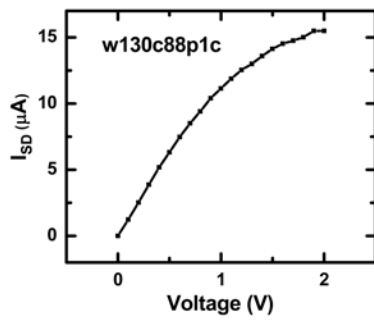
G. I_{SD} curves, Raman spectra and SEM images of biased SWNTs



G.2. $\ell = 1 \mu\text{m}$ $d_{\text{avg}} = 1.2 \text{ nm}$



G.3. $\ell = 1 \mu\text{m}$ $d_{\text{avg}} = 1.0 \text{ nm}$



H. Critical-point dryer (CPD)

In order to prevent capillary forces from causing tube misalignment while drying the sample, a CPD apparatus was used. This technique assures that the supercritical fluid phase is reached and the capillary forces are presumed negligible to cause any misalignment at the metal electrodes. The concept employs the use of a substance that can easily become a super critical fluid. In our apparatus we have used carbon dioxide (CO_2) to exchange the acetone medium surrounding the sample.

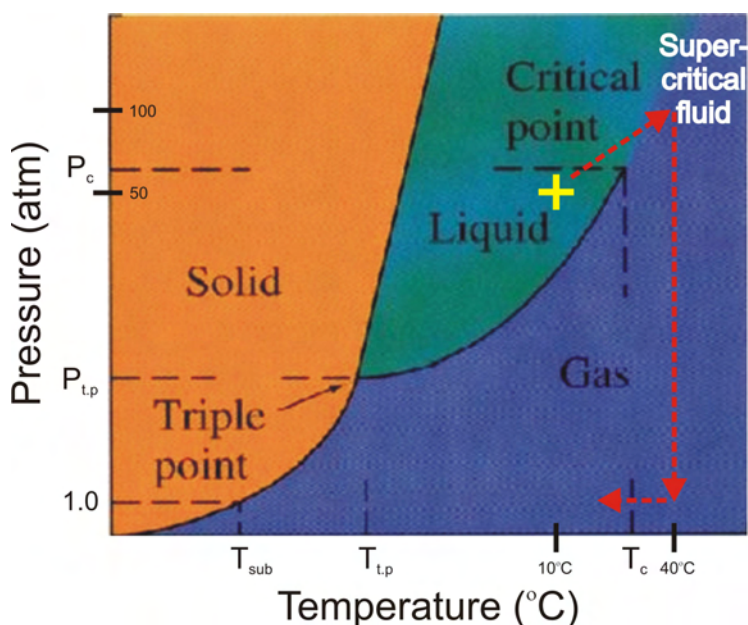


Figure H.1.: Carbon dioxide phase diagram. The sequence under which acetone is exchanged by the CO_2 is demonstrated with red arrows. The chamber pressure is 1 atm prior to the CO_2 injection however it increases rapidly to about 50 atm as the CO_2 is introduced at 10°C . We therefore set the exchange starting point at 50 atm and denote it by a yellow cross. $T_{sub} = -78^{\circ}\text{C}$, $T_{t.p.} = -56.6^{\circ}\text{C}$ and $T_c = 31^{\circ}\text{C}$ are the sublimation, triple-point and critical-point temperatures of CO_2 , respectively. The correlated pressures are also indicated with $P_{sub} = 1$ atm, $P_{t.p.} = 5.1$ atm and $P_c = 72.8$ atm. Note that the temperature and pressure axes are not to scale. Taken from www.chem.uncc.edu.

H. Critical-point dryer (CPD)

As the deposition time elapsed, the generator was switched OFF and the sample with its drop of stabilized-SWNTs suspension was directly dipped into acetone. The chamber containing the acetone and sample was then sealed. Figure H.1 demonstrates the acetone exchange on top of the CO₂ phase diagram. The exchange procedure starts by cooling the system to about 10°C. The CO₂ gas is injected in a regulated manner into the chamber and liquifies while at the same time the chamber pressure increases to about 50 atmospheres. The level of the liquid in the chamber raises, although two phases are still observed (acetone and CO₂). Next, the liquid is removed in a controlled manner as not to lose too much pressure. If the pressure is released too fast, bubbles are being formed as the CO₂ reaches its gas phase. Note that the liquid is not fully removed and its level is always kept above the sample surface. The exchange procedure is repeated several times, in which more and more acetone is replaced by CO₂ and the initial phase difference can no longer be observed. The cooling is then switched OFF and replaced by heating. The temperature and pressure of the chamber slowly increase to where the CO₂ reaches its super critical phase after about 30 minutes. This occurrence results in a pressure and a temperature of ~ 100 atmospheres and $\sim 40^\circ\text{C}$, respectively. The supercritical fluid phase above the critical point is reached and no distinction between the liquid and gas phases exists. Subsequently, the pressure is reduced back to 1 atmosphere still at 40°C (by slowly opening a valve). Finally, the heating is switched OFF and the system is cooled back to room-temperature before opening the chamber (after about 15 minutes).

I. Device fabrication for ambipolar SWNT s-FETs devices

To obtain both thin and thick oxide areas on the same chip, we have used the reactive ion etching (RIE) technique. P-type Si wafers with about 600 nm (or 800 nm) thermally grown oxide were the starting materials. A piece from the wafer was cut and mounted in a way that only part of it was exposed for etching. The part to serve for bonding was initially covered by a resist and later on by a narrow slice of Si¹. After the etching process, the whole piece was covered with a resist for writing purposes via e-beam lithography to obtain the desired structure. The layout described in section 3.2 was used as it provides many devices on the same chip as well as the conditions needed for the low-frequency dielectrophoretic deposition technique. The generated plasma of reactive species for the chemical etching (neutral radicals and ions) comprised the products of SF₆ gas or of a CHF₃ and O₂ gas mixture. Flow rates, pressure, temperature, power and etching time were all controlled. SF₆ gas was initially used, but we later changed to the CHF₃ and O₂ gas mixture so that an isotropic rather than anisotropic etching should occur². A representative outcome from such a procedure obtained with the SF₆ gas is shown in Fig. I.1 where one can observe the different colors originating from the two regions. The thick oxide is the area where the big leads are positioned and the thin oxide is the area where the SWNT-contacts are located. On the right part of Fig. I.1, a scratch in the silicon wafer is observed as a black line. This was done to ensure that the contact is grounded, initially for the deposition and later for the back gate-electrode. Also shown is a magnified image of a triple contact structure (a total of six are structured on one chip).

Etching rates were found by applying different etching durations, followed by thickness measurements of the resulting oxide layers via a reflectometry apparatus. The

¹A Si piece replaced the resist material as it gave better results, *i.e.*, no extra heating and cleaning processes were required.

²The addition of O₂ increases the concentration of fluorine free radicals and thus increases the etch rate of SiO₂ in all directions. The absolute rate is however controlled by the gas pressure.

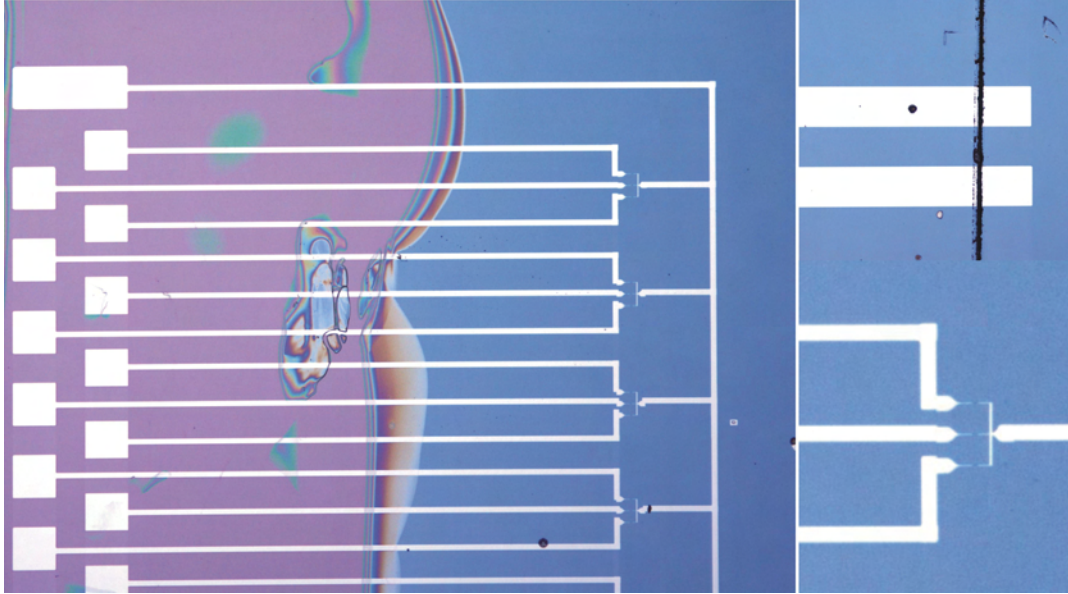


Figure I.1.: An optical image of the chip layout after both etching and metallization steps. Electrode material is Pd with a very thin Ti adhesion layer. The thick and thin oxides are distinguished by the purple and blue colors. A scratch and a magnified contact area are given on the right. The etching condition were as follows; gas flow: 40 sccm of SF₆, pressure: 22 mTorr, power: 70 W, etching time: 35 minutes, temperature: 25°C. Thick and thin oxide are ~800 nm and ~100 nm, respectively, as the etching rate was 20 nm/min. Note that a thick layer of resist was used to cover the area of the leads for bonding. It was later removed by acetone to recover back the 800 nm oxide. Sample w129c02.

rate obtained for SF₆ was 20 nm/min, however, for the CHF₃ and O₂ gas mixture it was found to be slower with only 10 nm etched per minute. The SF₆ was thus replaced by the gas mixture to achieve a better controlled isotropic rather than anisotropic etching process. The use of SF₆ resulted in a steep height variation between the two oxide areas. Thicker electrodes were therefore required to lower the resistance originating from this region of the electrode which is laying on both oxide areas, as shown in Fig. I.1. Thicker metal material can end-up with lift-off difficulties, which may result in metal residues, affecting tube-electrode contact-interfaces. An extra short etching step (~5 minutes with CHF₃ and O₂ gas mixture) can solve this side effect. Figure I.2 is an example of a contact which endured the second short etching step. Note that the etching time with the CHF₃ and O₂ gas mixture was adjusted to give ~350 nm oxide rather than the too thin oxide of ~100 nm, initially used with the SF₆ gas that in many cases resulted in short-circuits. These

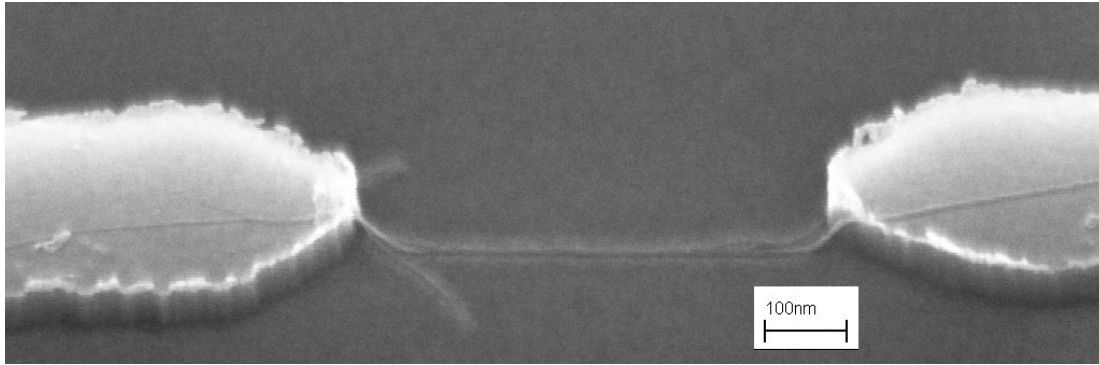


Figure I.2.: SEM image of an etched electrode contact taken at 45° . After 5 minutes, the electrodes are about 50 nm higher than the oxide surface, corresponding to a 10 nm/min etching rate with the CHF_3 and O_2 gas mixture. The etching conditions for this gas mixture were as follows; gas flow: 30 sccm of CHF_3 and 1.6 sccm of O_2 , pressure: 22 mTorr, power: 60 W, temperature: 25°C . The chip was previously etched (35 minutes) to achieve the thick (~ 800 nm) and thin oxide areas (~ 350 nm). The thin area was further thinned to ~ 300 nm after the extra 5 minutes etching time. Sample w129c100p1c.

shorts occurred if already existing pin-holes were located at the designated area for the SWNTs-bridged-contacts. In addition, the original thermal oxide thickness was changed to 800 nm to minimize the occurrence of shorts while bonding the sample.

I. Device fabrication for ambipolar SWNT s-FETs devices

List of Figures

2.1. Graphene lattice	4
2.2. BZ of graphene	6
2.3. BZ of armchair and zig-zag tubes	8
2.4. Band structure and 1 st BZ of graphene	9
2.5. DOS derivation of a metallic tube via its electronic band structure . .	12
2.6. Band structures of zig-zag, armchair and semiconducting tubes	13
2.7. Phonon scattering processes in a metallic SWNT	17
2.8. High-bias electron-phonon coupling	19
2.9. Schematic illustration of the Stokes and anti-Stokes first-order Raman scattering processes	21
2.10. Schematic illustration of double-resonant Raman scattering processes	24
2.11. <i>Ab-initio</i> calculations of graphene phonon-dispersion	26
2.12. D-mode double-resonance process in an armchair tube	28
2.13. Double-resonance scattering processes leading to the two high-energy modes	30
2.14. Electronic band structure at the graphene K-point	32
2.15. Neutral and charged bodies response to both homogeneous and inho- mogeneous electric fields	34
2.16. The behaviors of neutral and charged bodies in both electrode polar- ities of an alternating inhomogeneous electric field	35
2.17. Schematic illustration for the setup used in tube separation experiment	41
2.18. Schematic illustration of a SWNT in a cylindrical SDBS micelle . . .	42
2.19. Minimum electric field strength required to move a micellated SWNT via dielectrophoresis	43
3.1. Pulsed laser vaporization setup and high-resolution TEM image of a bundle of SWNTs	46

List of Figures

3.2.	A drawing of the chip layout for the SWNTs deposition with its wiring plan	47
3.3.	A side view of SWNTs-stabilized suspension on top of a chip	48
3.4.	Schematic illustration of a bonded SWNT prepared for electrical measurement	51
3.5.	Schematic drawing of the confocal microscope setup	52
3.6.	Normalized collection efficiency as a function of pinhole size	53
3.7.	Beam-path as given for a CRM 200 setup	54
4.1.	Metallic SWNTs resistances for the tube-on-metal configuration	59
4.2.	SEM and AFM imaging of an individual aligned SWNT	60
4.3.	Electrical transport measurements and the corresponding Raman spectra of an individual semiconducting SWNT and an individual metallic SWNT	62
4.4.	Hysteresis effect in an individual semiconducting SWNT	63
4.5.	Excitation energies <i>versus</i> the inverse RBM frequency	67
4.6.	G mode line-shape of metallic and semiconducting SWNTs	68
4.7.	G mode analysis of individual metallic SWNTs	69
4.8.	G mode analysis of individual semiconducting SWNTs	70
4.9.	The width of the G^- peak of metallic and semiconducting SWNTs	72
4.10.	Experimental and calculated data for the G^+ and G^- modes in metallic SWNTs	75
4.11.	Integrated metal plate and socket for electrical measurements	77
4.12.	The electrical and Raman parts of the setup used for simultaneous measurements	78
4.13.	Raman spectra of a biased metallic SWNT at different voltages	80
4.14.	Measured AS/S intensity ratios and calculated effective-temperatures <i>versus</i> applied voltage	82
4.15.	$I-V_{SD}$ curve from the biased SWNT in a tube-on-metal configuration	83
4.16.	Metal-on-tube-configuration	86
4.17.	Deriving R_{low} and I_0 from an $I-V_{SD}$ curve	87
4.18.	Current saturation <i>versus</i> R_{low} from various devices	88
4.19.	Etched contact by ammonium fluoride solution	90
4.20.	Collapsed contact	91
4.21.	UV-VIS-NIR spectra of 1 nm <i>versus</i> 1.2 nm NiCo SWNTs	92

4.22. Ambipolar scheme for infrared light emission	93
4.23. Ambipolar electrical behavior from a SWNT s-FET device	95
4.24. Ambipolar behavior from a SWNT s-FET device with 800 nm gate oxide	96
A.1. U and U' rotational axis operations	104
B.1. NaCholate and SDBS chemical structures	105
D.1. Calculated Raman intensity <i>versus</i> frequency	116
E.1. Phonon dispersion of graphite	118
H.1. Carbon dioxide phase diagram	127
I.1. Optical image of the chip layout	130
I.2. SEM image of an etched electrode contact	131

List of Figures

List of Tables

- 2.1. The variation in the relative polarizability factor $\varepsilon_{r1} \left(\frac{\varepsilon_{r2} - \varepsilon_{r1}}{\varepsilon_{r2} + 2\varepsilon_{r1}} \right)$ of different systems 38
- 3.1. $\frac{\pi d_p}{v_p \lambda}$ values for various wavelengths and pinhole sizes 55
- 4.1. Raman data analysis of individual metallic SWNTs 65
- 4.2. Raman data analysis of individual semiconducting SWNTs 66

List of Tables

Bibliography

- [1] S. Iijima. Helical microtubules of graphitic carbon. *Nature (London)*, 354:56–58, 1991.
- [2] W.A. De Heer, A. Chatelain, and D. Ugarte. A Carbon Nanotube Field-Emission Electron Source. *Science*, 270:1179–1180, 1995.
- [3] A. Modi, N. Koratkar, E. Lass, B. Wei, and P.M. Ajayan. Miniaturized gas ionization sensors using carbon nanotubes. *Nature*, 424:171–174, 2003.
- [4] D.S. Chung, S.H. Park, H.W. Lee, J.H. Choi, S.N. Cha, J.W. Kim, J.E. Jang, K.W. Min, S.H. Cho, M.J. Yoon, J.S. Lee, C.K. Lee, J.H. Yoo, and J.M. Kim. Carbon nanotube electron emitters with a gated structure using backside exposure processes. *App. Phys. Lett.*, 80(21):4045–4047, 2002.
- [5] M.S. Dresselhaus, G. Dresselhaus, and P.C. Eklund. *Science of Fullerenes and Carbon Nanotubes*. Academic: San Diego, 1996.
- [6] B.I. Yakobson and R.E. Smalley. Fullerene nanotubes: C-1000000 and beyond. *Am. Sci.*, 85(4):324–337, 1997.
- [7] C. Dekker. Carbon nanotubes as molecular quantum wires. *Phys. Today*, 52(5):22–28, 1999.
- [8] Z. Wu, Z. Chen, X. Du, J.M. Logan, J. Sippel, M. Nikolou, K. Kamaras, J.R. Reynolds, D.B. Tanner, A.F. Hebard, and A.G. Rinzler. Transparent, Conductive Carbon Nanotube Films. *Science*, 305:1273–1276, 2004.
- [9] Z. Yao, C.L. Kane, and C. Dekker. High-field electrical transport in single-wall carbon nanotubes. *Phys. Rev. Lett.*, 84(13):2941–2944, 2000.
- [10] J.Y. Park, S. Rosenblatt, Y. Yaish, V. Sazonova, H. Üstünel, S. Braig, T.A. Arias, P.W. Brouwer, and P.L. McEuen. Electron-phonon scattering in metallic single-walled carbon nanotubes. *Nano Lett.*, 4(3):517–520, 2003.

Bibliography

- [11] A. Javey, J. Guo, M. Paulsson, Q. Wang, D. Mann, M. Lundstrom, and H. Dai. High-field Quasiballistic Transport in Short Carbon Nanotubes. *Phys. Rev. Lett.*, 92:106804–1, 2004.
- [12] S. Reich, C. Thomson, and J. Maultzsch. *Carbon nanotubes - basic concepts and physical properties*. WILEY-VCH Verlag GmbH & Co. KGaA, 2003.
- [13] Ge.G. Samsonidze, R. Saito, A. Jorio, M.A. Pimenta, A.G. Souza Filho, A. Grüneis, G. Dresselhaus, and M.S. Dresselhaus. The concept of cutting lines in carbon nanotube science. *J. Nanosci. Nanotech.*, 3:431–458, 2003.
- [14] R. Saito, G. Dresselhaus, and M.S. Dresselhaus. *Physical properties of carbon nanotubes*. Imperial College Press, 1998.
- [15] T.W. Odom, J.L. Huang, P. Kim, and C.M. Lieber. Structure and electronic properties of carbon nanotubes. *J. Phys. Chem. B*, 104:2794–2809, 2000.
- [16] V. Perebeinos, J. Tersoff, and Ph. Avouris. Effect of Exciton-Phonon Coupling in the Calculated Optical Absorption of Carbon Nanotubes. *Phys. Rev. Lett.*, 94:027402–1, 2005.
- [17] L. Marty, E. Adam, L. Albert, R. Doyon, D. Ménard, and R. Martel. Exciton Formation and Annihilation during 1D Impact Excitation of Carbon Nanotubes. *Phys. Rev. Lett.*, 96:136803–1, 2006.
- [18] G. Dukovic, F. Wang, D. Song, M.Y. Sfeir, T.F. Heinz, and L.E. Brus. Structural Dependence of Excitonic Optical Transitions and Band-Gap Energies in Carbon Nanotubes. *Nano Lett.*, 5:2314–2318, 2005.
- [19] R. Saito, G. Dresselhaus, and M.S. Dresselhaus. Trigonal warping effect of carbon nanotubes. *Phys. Rev. B*, 61(4):2981–2990, 2000.
- [20] M. Ouyang, J.L. Huang, C.L. Cheung, and C.M. Lieber. Energy gaps in "metallic" single-walled carbon nanotubes. *Science*, 292:702–705, 2001.
- [21] M. Ouyang, J.L. Huang, and C.M. Lieber. Fundamental electronic properties and applications of single-walled carbon nanotubes. *Acc. Chem. Res.*, 35:1018–1025, 2002.
- [22] A. Kleiner and S. Eggert. Curvature, hybridization, and STM images of carbon nanotubes. *Phys. Rev. B*, 64:113402–1, 2001.

- [23] J.C. Charlier and J.P. Issi. Electronic structure and quantum transport in carbon nanotubes. *Appl. Phys. A*, 67:79–87, 1998.
- [24] W. Kim, A. Javey, O. Vermesh, Q. Wang, Y. Li, and H. Dai. Hysteresis caused by water molecules in carbon nanotube field effect transistors. *Nano. Lett.*, 3(2):193–198, 2003.
- [25] M.S. Fuhrer, B.M. Kim, T. Dürkop, and T. Brintlinger. High-mobility nanotube transistor memory. *Nano. Lett.*, 2:755–759, 2002.
- [26] S.J. Tans, M.H. Devoret, H. Dai, A. Thess, R.E. Smalley, and C. dekker. Individual single-wall carbon nanotubes as quantum wires. *Nature (London)*, 386:474–477, 1997.
- [27] R. Martel, T. Schmidt, H.R. Shea, T. Hertel, and Ph. Avouris. Single- and multi-wall carbon nanotube field effect transistors. *Appl. Phys. Lett.*, 73(17):2447–2449, 1998.
- [28] S. Heinze, J. Tersoff, R. Martel, V. Derycke, J. Appenzeller, and Ph. Avouris. Carbon nanotubes as schottky barrier transistors. *Phys. Rev. Lett.*, 89(10):106801–1, 2002.
- [29] A. Javey, J. Guo, Q. Wang, M. Lundstrom, and H. Dai. Ballistic carbon nanotube field-effect transistors. *Nature (London)*, 424:654–657, 2003.
- [30] J. Kong, E. Yenilmez, T.W. Tombler, W. Kim, and H. Dai. Quantum interference and ballistic transmission in nanotube electron waveguides. *Phys. Rev. Lett.*, 87:106801–1, 2001.
- [31] W. Liang, M. Bockrath, D. Bozovic, J.H. Hafner, M. Tinkham, and H. Park. Fabry-Perot interference in a nanotube electron waveguide. *Nature (London)*, 411:665–669, 2001.
- [32] C.T. White and T.N. Todorov. Carbon nanotubes as long ballistic conductors. *Nature (London)*, 393:240–242, 1998.
- [33] M. Lazzeri, S. Piscanec, F. Mauri, A.C. Ferrari, and J. Robertson. Electron Transport and Hot Phonons in Carbon Nanotubes. *Phys. Rev. Lett.*, 95:236802–1, 2005.

Bibliography

- [34] L.X. Benedict, S.G. Louie, and M.L. Cohen. Static polarizabilities of single-wall carbon nanotubes. *Phys. Rev. B*, 52(11):8541–8549, 1995.
- [35] R.P. Vidano, D.B. Fischbach, L.J. Willis, and T.M. Loehr. Observation of Raman band shifting with excitation wavelength for carbon and graphites. *Solid State Commun.*, 39:341–344, 1981.
- [36] I. Pocsik, Hundhausen.M., M. Koos, and L. Ley. Origin of the D peak in the Raman spectrum of microcrystalline graphite. *J. Non-Cryst. Sol.*, 230B:1083–1086, 1998.
- [37] C. Thomsen and S. Reich. Double-resonant Raman scattering in graphite. *Phys. Rev. Lett.*, 85(24):5214–5217, 2000.
- [38] D. Sanchez-Portal, E. Artacho, J.M. Soler, A. Rubio, and P. Ordejón. *Ab initio* structural, elastic, and vibrational properties of carbon nanotubes. *Phys. Rev. B*, 59(19):12678–12688, 1999.
- [39] A. Venkateswaran, A.M. Rao, E. Richter, M. Menon, A. Rinzler, R.E. Smalley, and P.C. Eklund. Probing the single-wall carbon nanotube bundle: Raman scattering under high pressure. *Phys. Rev. B*, 59(16):10928–10934, 1999.
- [40] M.J. O’Connell, S. Sivaram, and S.K. Doorn. Near-infrared resonance Raman excitation profile studies of single-walled carbon nanotube intertube interactions: A direct comparison of bundled and individually dispersed HiPco nanotubes. *Phys. Rev. B*, 69:235415–1, 2004.
- [41] C. Fantini, A. Jorio, M. Souza, M.S. Strano, M.S. Dresselhaus, and M.A. Pimenta. Optical Transition Energies for Carbon Nanotubes from Resonant Raman Spectroscopy: Environment and Temperature Effects. *Phys. Rev. Lett.*, 93:147406–1, 2004.
- [42] F. Tuinstra and J.L. Koenig. Raman spectrum of graphite. *J. Chem. Phys.*, 53(3):1126–1130, 1970.
- [43] J. Kastner, T. Pichler, S. Kuzmany, H. Curran, and W. Blau. Resonance Raman and infrared-spectroscopy of carbon nanotubes. *Chem. Phys. Lett.*, 221:53–58, 1994.

- [44] J. Kürti, A. Zólyomi, V. Grüneis, and H. Kuzmany. Double resonant Raman phenomena enhanced by van Hove singularities in single-wall carbon nanotubes. *Phys. Rev. B*, 65:165433–1, 2002.
- [45] J. Maultzsch, S. Reich, C. Thomsen, S. Webster, and R. Czerw. Raman characterization of boron-doped multiwalled carbon nanotubes. *Appl. Phys. Lett.*, 81(14):2647–2649, 2002.
- [46] J. Maultzsch, S. Reich, and C. Thomsen. Chirality-selective Raman scattering of the D mode in carbon nanotubes. *Phys. Rev. B*, 64:121407–1, 2001.
- [47] M. Damnjanović, T. Vuković, and I. Milošević. Fermi level quantum numbers and secondary gap of conducting carbon nanotubes. *Solid State Commun.*, 116:265–267, 2000.
- [48] J. Maultzsch, S. Reich, U. Schlecht, and C. Thomsen. High-energy phonon branches of an individual metallic carbon nanotube. *Phys. Rev. Lett.*, 91:87402–1, 2003.
- [49] A.M. Rao, E. Richter, S. Bandow, B. Chase, and P.C. Eklund. Diameter-selective Raman scattering from vibrational modes in carbon nanotubes. *Science*, 275(5297):187–191, 1997.
- [50] O. Dubay, G. Kresse, and H. Kuzmany. Phonon softening in metallic tubes by a peierls-like mechanism. *Phys. Rev. Lett.*, 88:235506–1, 2002.
- [51] J. Maultzsch, S. Reich, and C. Thomsen. Raman scattering in carbon nanotubes revisited. *Phys. Rev. B*, 65:233402–1, 2002.
- [52] M. Oron-Carl, F. Hennrich, M.M. Kappes, H. von Löhneysen, and R. Krupke. On the Electron-Phonon Coupling of Individual Single-Walled Carbon Nanotubes. *Nano. Lett.*, 5(9):1761–1767, 2005.
- [53] A. Kasuya, Y. Sasaki, K. Tohji, and Y. Nishina. Evidence for size-dependent discrete dispersions in single-wall nanotubes. *Phys. Rev. Lett.*, 78(23):4434–4437, 1997.
- [54] E. Richter and K.R. Subbaswamy. Theory of size-dependent resonance Raman scattering from carbon nanotubes. *Phys. Rev. Lett.*, 79(14):2738–2741, 1997.

Bibliography

- [55] S.D.M. Brown, P. Corio, A. Marucci, M.S. Dresselhaus, M.A. Pimenta, and K. Kneipp. Anti-Stokes Raman spectra of single-walled carbon nanotubes. *Phys. Rev. B*, 61(8):5137–5140, 2000.
- [56] K. Kempa. Gapless plasmons in carbon nanotubes and their interactions with phonons. *Phys. Rev. B*, 66:195406–1, 2002.
- [57] C. Jiang, K Kempa, J. Zhao, U. Schlecht, U. Kolb, T. Basché, M. Burghard, and A. Mews. Strong enhancement of the Breit-Wigner-Fano Raman line in carbon nanotube bundles caused by plasmon band formation. *Phys. Rev. B*, 66:161404–1, 2002.
- [58] M. Lazzeri, S. Piscanec, F. Mauri, A.C. Ferrari, and J. Robertson. Phonon Linewidths and Electron Phonon Coupling in Nanotubes. *Phys. Rev. B*, 73:155426–1, 2006.
- [59] R. Krupke, F. Hennrich, H. von Löhneysen, and M.M. Kappes. Separation of metallic from semiconducting single-walled carbon nanotubes. *Science*, 301:344–347, 2003.
- [60] H.A. Pohl. *Dielectrophoresis - The behavior of neutral matter in nonuniform electric fields*. CAMBRIDGE UNIVERSITY PRESS, 1978.
- [61] H.A. Pohl and I. Hawk. *Science*, 152:p. 647, 1966.
- [62] J.S. Crane and H.A. Pohl. *J. Electrochem. Soc.*, 115:p. 584, 1968.
- [63] R. Krupke, F. Hennrich, M.M. Kappes, and H. von Löhneysen. Surface conductance induced dielectrophoresis of semiconducting single-walled carbon nanotubes. *Nano Lett.*, 4(8):1395–1399, 2004.
- [64] L.X. Benedict, S.G. Louie, and M.L. Chohen. Static polarizabilities of single-wall carbon nanotubes. *Phys. Rev. B*, 52(11):8541–8549, 1995.
- [65] S. Lebedkin, K. Arnold, F. Hennrich, R. Krupke, B. Renker, and M.M. Kappes. FTIR-luminescence mapping of dispersed single-walled carbon nanotubes. *New Journal of Physics*, 5:140.1–140.11, 2003.
- [66] S. Lebedkin, F. Hennrich, T. Skipa, and M.M. Kappes. Near-infrared photoluminescence of single-walled carbon nanotubes prepared by the laser vaporization method. *Phys. Chem. B*, 107(9):1949–1956, 2003.

- [67] M.P. Hughes. Dielectrophoretic behavior of latex nanospheres: Low-frequency dispersion. *Colloid Interface Sci.*, 250(2):291–294, 2002.
- [68] H. Morgan and N.G. Green. Dielectrophoretic manipulation of rod-shaped viral particles. *J. Electrostatics*, 42(3):279–293, 1997.
- [69] S. Lebedkin, P. Schweiss, B. Renker, S. Malik, F. Hennrich, M. Neumaier, C. Stoermer, and M.M. Kappes. Single-wall carbon nanotubes with diameters approaching 6 nm obtained by laser vaporization. *Carbon*, 40(3):417–423, 2002.
- [70] R. Krupke, F. Hennrich, H.B. Weber, M.M. Kappes, and H. von Löhneysen. Simultaneous deposition of metallic bundles of single-walled carbon nanotubes using ac-dielectrophoresis. *Nano Lett.*, 3(8):1019–1023, 2003.
- [71] M. Oron, R. Krupke, F. Hennrich, H.B. Weber, D. Beckmann, H.von. Löhneysen, and M.M. Kappes. Simultaneous Deposition of Individual Single-Walled Carbon Nanotubes onto Microelectrodes via AC-Dielectrophoresis. *Electronic properties of synthetic nanostructures*, edited by H. Kuzmany, J. Fink, M. Mehring, and S. Roth, AIP Conference proceedings, American Institute of Physics: New York:561–564, 723, 2004.
- [72] *Copyright WITec Wissenschaftliche Instrumente und Technologie GmbH 1998-2001. Confocal Raman Microscope, CRM 200 Manual.*
- [73] R. Krupke, F. Hennrich, H.B. Weber, D. Beckmann, O. Hampe, S. Malik, M.M. Kappes, and H. von Löhneysen. Contacting single bundles of carbon nanotubes with alternating electric fields. *Appl. Phys. A*, 76:397–400, 2003.
- [74] S.B. Cronin, R. Barnett, M. Tinkham, S.G. Chou, O. Rabin, M.S. Dresselhaus, A.K. Swan, M.S. Unlu, and B.B. Goldberg. Electrochemical gating of individual single-wall carbon nanotubes observed by electron transport measurements and resonant raman spectroscopy. *Appl. Phys. Lett.*, 84(12):2052–2054, 2004.
- [75] K. Balasubramanian, Y. Fan, M. Burghard, and K. Kern. Photoelectronic transport imaging of individual semiconducting carbon nanotubes. *Appl. Phys. Lett.*, 84(13):2400–2402, 2004.
- [76] M. Oron, F. Hennrich, M.M. Kappes, and R. Krupke. Correlation between Transport Measurements and Resonant Raman Spectroscopy on site-deposited

- Individual Carbon Nanotubes. *Electronic properties of novel nanostructures*, edited by H. Kuzmany, J. Fink, M. Mehring, and S. Roth, AIP Conference proceedings, American Institute of Physics: New York:574–577, 786, 2005.
- [77] V. Derycke, R. Martel, J. Appenzeller, and Ph. Avouris. Controlling doping and carrier injection in carbon nanotube transistors. *Appl. Phys. Lett.*, 80(15):2773–2775, 2002.
- [78] X. Cui, M. Freitag, R. Martel, L. Brus, and Ph. Avouris. Controlling Energy-Level Alignments at Carbon Nanotube/Au Contacts. *Nano Lett.*, 3(6):783–787, 2003.
- [79] A. Vijayaraghavan, S. Kar, S. Talapatra, C. Soldano, Y. Kobayashi, O. Nalamasu, and P.M. Ajayan. Charge-injection-induced Dynamic Screening and Origin of Hysteresis in Field-modulated Transport in Single-wall Carbon Nanotubes. *Submitted to Appl. Phys. Lett.*, 2006.
- [80] H. Telg, J. Maultzsch, S. Reich, F. Hennrich, and C. Thomsen. Chirality Distribution and Transition Energies of Carbon Nanotubes. *Phys. Rev. Lett.*, 93(17):177401–1, 2004.
- [81] F. Hennrich, R. Krupke, S. Lebedkin, K. Arnold, R. Fischer, D. Resasco, and M.M. Kappes. Raman spectroscopy of Individual Single-Walled Carbon Nanotubes from Various Sources. *J. Phys. Chem. B*, 109:10567–10573, 2005.
- [82] S. Reich, J. Maultzsch, C. Thomson, and P. Ordejón. Tight-binding description of graphene. *Phys. Rev. B*, 66:35412–1, 2002.
- [83] S.M. Bachilo, M.S. Strano, C. Kittrell, R.H. Hauge, R.E. Smalley, and R.B. Weisman. Structure-Assigned Optical Spectra of Single-Walled Carbon Nanotubes. *Science*, 298:2361–2366, 2002.
- [84] S. Piscanec, M. Lazzeri, F. Mauri, A.C. Ferrari, and J. Robertson. Kohn Anomalies and Electron-Phonon Interactions in Graphite. *Phys. Rev. Lett.*, 93(18):185503–1, 2004.
- [85] S.D.M. Brown, A. Jorio, P. Corio, M.S. Dresselhaus, G. Dresselhaus, R. Saito, and K. Kneipp. Origin of the Breit-Wigner-Fano lineshape of the tangential G-band feature of metallic carbon nanotubes. *Phys. Rev. B*, 63:155414–1, 2001.

- [86] J. Maultzsch, S. Reich, C. Thomsen, H. Requardt, and P. Ordejón. Phonon dispersion of graphite. *Phys. Rev. Lett.*, 92(7):75501–1, 2004.
- [87] A. Jorio, A.G.S. Filho, G. Dresselhaus, M.S. Dresselhaus, A.K. Swan, M.S. Ünlü, B.B. Goldberg, M.A. Pimenta, J.H. Hafner, C.M. Lieber, and R. Saito. G-band resonant Raman study of 62 isolated single-wall carbon nanotubes. *Phys. Rev. B*, 65:155412–1, 2002.
- [88] S.K Doorn, M.J. O’Connell, L. Zheng, Y.T. Zhu, S. Huang, and J. Liu. Raman Spectral Imaging of a Carbon Nanotube Intramolecular Junction. *Phys. Rev. Lett.*, 94:16802–1, 2005.
- [89] M.A. Pimenta, A. Marucci, S.A. Empedocles, M.G. Bawendi, and E.B. Hanlon. Raman modes of metallic carbon nanotubes. *Phys. Rev. B*, 58(24):16016–16019, 1998.
- [90] V. Scardaci and A.C. Ferrari. unpublished. 2005.
- [91] P.G. Collins, M.S. Arnold, and Ph. Avouris. Engineering Carbon Nanotubes and Nanotube Circuits Using Electrical Breakdown. *Science*, 292:706–709, 2001.
- [92] J. H. Noggle. *Physical Chemistry, Third Edition*. Harper Collins Colledge Publishers, 1996.
- [93] Z. Yao, H. Postma, L. Balents, and C. Dekker. Carbon nanotube intramolecular junctions. *Nature*, 402:273–276, 1999.
- [94] S.J. Tans, A.R.M. Verschueren, and C. Dekker. Room-temperature transistor based on a single carbon nanotube. *Nature*, 393:49–51, 1998.
- [95] J. Nygård, D.H. Cobden, M. Bockrath, P.L. McEuen, and P.E. Lindelof. Electrical transport measurements on single-walled carbon nanotubes. *Appl. Phys. A*, 69:297–304, 1999.
- [96] M. Liebau, E. Unger, G.S. Duesberg, A.P. Graham, R. Seidel, F. Kreupl, and W. Hoenlein. Contact improvement of carbon nanotubes via electroless nickel deposition. *Appl. Phys. A*, 77:731–734, 2003.

Bibliography

- [97] D.A. Heller, R.M. Mayrhofer, S. Baik, M.L. Grinkova, Y.V. Usrey, and M.S. Strano. Concomitant Length and Diameter Separation of Single-Walled Carbon Nanotubes. *J. Am. Chem. Soc.*, 126:14567–14573, 2004.
- [98] W. Kim, A. Javey, R. Tu, J. Cao, Q. Wang, and H. Dai. Electrical Contacts to Carbon Nanotubes Down to 1nm in Diameter. *Appl. Phys. Lett.*, cond-mat/0505431:in press, 2006.
- [99] J. Cao, Q. Wang, D. Wang, and H. Dai. Suspended Carbon Nanotube Quantum Wires with Two Gates. *Small*, 1(1):138–141, 2005.
- [100] E. Pop, D. Mann, J. Cao, Q. Wang, K. Goodson, and H. Dai. Negative Conductance and Hot Phonons in Suspended Nanotube Molecular Wires. *Phys. Rev. Lett.*, 95:155505–1, 2005.
- [101] R. Martel, V. Derycke, C. Lavoie, J. Appenzeller, K.K. Chan, J. Tersoff, and Ph. Avouris. Ambipolar Electrical Transport in Semiconducting Single-Wall Carbon Nanotubes. *Phys. Rev. Lett.*, 87(25):256805–1, 2001.
- [102] J.A. Misewich, R. Martel, Ph. Avouris, J.C. Tsang, S. Heinze, and J. Tersoff. Electrically Induced Optical Emission from a Carbon Nanotube FET. *Science*, 300:783–786, 2003.
- [103] M. Freitag, J. Chen, J. Tersoff, J.C. Tsang, Q. Fu, J. Liu, and Ph. Avouris. Mobile Ambipolar Domain in Carbon-Nanotube Infrared Emitters. *Phys. Rev. Lett.*, 93(7):076803–1, 2004.
- [104] M. Freitag, V. Perebeinos, J. Chen, A. Stein, J.C. Tsang, J. Misewich, R. Martel, and Ph. Avouris. Hot Carrier Electroluminescence from a Single Carbon Nanotube. *Nano Lett.*, 4(6):1063–1066, 2004.
- [105] S.J. Wind, J. Appenzeller, R. Martel, V. Derycke, and Ph. Avouris. Vertical scaling of carbon nanotube field-effect transistors using top gate electrodes. *Appl. Phys. Lett.*, 80(20):3817–3819, 2002.
- [106] J. Appenzeller, J. Knoch, V. Derycke, R. Martel, S.J. Wind, and Ph. Avouris. Field-Modulated Carrier Transport in Carbon Nanotube Transistors. *Phys. Rev. Lett.*, 89(12):126801–1, 2002.

- [107] Y.M. Lin, J. Appenzeller, and Ph. Avouris. Ambipolar-to-Unipolar Conversion of Carbon Nanotube Transistors by Gate Structure Engineering. *Nano Lett.*, 4(5):947–950, 2004.
- [108] S.M. Bachilo, L. Balzano, J.E. Herrera, F. Pompeo, D.E. Resasco, and R.B. Weisman. Narrow (n,m)-Distribution of Single-Walled Carbon Nanotubes Grown Using a Solid Supported Catalyst. *J. Am. Chem. Soc.*, 125:11186–11187, 2003.
- [109] M. Damnjanović, I. Milosević, T. Vuković, and R. Sredanović. Full symmetry, optical activity, and potentials of single-wall and multiwall nanotubes. *Phys. Rev. B*, 60(4):2728–2739, 1999.
- [110] M. Damnjanović, T. Vuković, and I. Milošević. Modified group projectors: Tight binding method. *J. Phys. A: Math. Gen.*, 33(37):6561–6571, 2000.
- [111] F. Lopez, J. Samseth, K. Mortensen, E. Rosenqvist, and J. Rouch. Micro- and Macrostructural Studies of Sodium Deoxycholate Micellar Complexes in Aqueous Solutions. *Langmuir*, 12:6188–6196, 1996.
- [112] M. V. Klein in. *Light Scattering in Solids*. Edited by M. Cardona, Springer-Verlag Berlin Heidelberg New York, 1975, pp. 169-172.
- [113] H. Kataura, Y. Kumazawa, Y. Maniwa, I. Umezū, S. Suzuki, Y. Ohtsuka, and Y. Achiba. Optical properties of single-wall carbon nanotubes. *Synth. Met.*, 103:2555–2558, 1999.
- [114] L. Alvarez, A. Righi, T. Guillard, E. Rols, S. Anglaret, D. Laplaze, and J.-L. Sauvajol. Resonant Raman study of the structure and electronic properties of single-wall carbon nanotubes. *Chem. Phys. Lett.*, 316:186–190, 2000.
- [115] M. Paillet, Ph. Poncharal, A. Zahab, J.-L. Sauvajol, J.C. Meyer, and Roth.S. Vanishing of the Breit-Wigner-Fano Component in Individual Single-Wall Carbon Nanotubes. *Phys. Rev. Lett.*, 94:237401–1, 2005.
- [116] W. Kohn. Image of the Fermi surface in the vibration spectrum of a metal. *Phys. Rev. Lett.*, 2(9):393–394, 1959.

Bibliography

List of publications

1. M. Oron-Carl, F. Hennrich, M.M. Kappes, H. von Löhneysen and R. Krupke, “On the Electron-Phonon Coupling of Individual Single-Walled Carbon Nanotubes”, *Nano Lett.* 5(9), 1761–1767 (2005).
2. M. Oron, F. Hennrich, M.M. Kappes and R. Krupke. “Correlation between Transport Measurements and Resonant Raman Spectroscopy on site-deposited Individual Carbon Nanotubes”. *Electronic properties of novel nanostructures*, edited by H. Kuzmany, J. Fink, M. Mehring, and S. Roth, AIP Conference proceedings, American Institute of Physics: New York: 786, 574–577 (2005).
3. M. Oron, R. Krupke, F. Hennrich, H.B. Weber, D. Beckmann, H.von. Löhneysen, and M.M. Kappes. “Simultaneous Deposition of Individual Single-Walled Carbon Nanotubes onto Microelectrodes via AC-Dielectrophoresis”. *Electronic properties of synthetic nanostructures*, edited by H. Kuzmany, J. Fink, M. Mehring, and S. Roth, AIP Conference proceedings, American Institute of Physics: New York: 723, 561–564 (2004).
4. M. Oron, T. Kerle, R. Yerushalmi-Rozen and J. Klein, “Persistent droplet motion in liquid-liquid dewetting”, *Phys. Rev. Lett.* 92(23), 236104-1 (2004).
5. J. P. Nair, I. Zon, M. Oron, R. P. Biro, Y. Feldman and I. Lubomirsky, “Stoichiometry control during deposition by ion beam sputtering”, *J. Appl. Phys.* 92(8), 4784–4790 (2002).

Bibliography